Atomistic Modelling of Diffusion Mechanisms of Carbon Defects at the SiO_2/4H-SiC Interface

Hind Ateeg Alsnani

Submitted for the Degree of Doctor of Philosophy
School of Engineering, Newcastle University, UK
October 2019

Acknowledgements

After thanking God, I would like to give my heartfelt appreciation goes to my mother, Mrs Aisha Suluman, for her endless love and my beloved husband, Abdullah who always inspired me and gave me support throughout my PhD studies, and to my loving children, Manar, Mayar, Rakan and Lana.

I would like to thank my supervisor, Dr Jonathan Goss, for sharing his knowledge and expertise with me and for providing invaluable support and useful discussions during my PhD studies.

I would also like to thank my co-supervisor, Dr Alton Horsfall, for supporting me at the beginning of my PhD studies.

I am grateful to my colleagues, Fatma Otain, Khatar, Muna Fallatah, Fatimah Bahrani, Oras Alani, Naseem Alsaif, Eman Alkhudhayr, Amirah Alrasheed, Wina Mohamed, Luke Bradley, James Beattie, Claire and Johan Gausden for sharing their knowledge and for our friendly discussions.

I am indebted to both Umm Al-Qura University and the Ministry of Higher Education for sponsoring my studies with a scholarship.

Finally, I would like to give my special thanks to my sisters, brother and other family members, for their continuous moral support during my PhD.

Abstract

4H-SiC is an attractive material for high-power, high-temperature electronics because it has a wide band-gap, favourable thermal-conductivity and the beneficial SiO_2 native oxide. However, SiC device characteristics are degraded by electrically-active defects with electronic states located deep within the band-gap arising from native defects in the SiC and close to the SiO_2 interfaces.

In this thesis are presented the results of a computational study to understand the dynamics of selected native defects, with reference to the SiO_2/4H-SiC interface. Density-functional simulations have been used to explore defect structures, electrical properties and diffusion energetics. The modelling exploits the computational advantages of periodic boundary conditions to represent both bulk and interface cases. Different interfaces corresponding to the internal structure of the SiC have been examined, and many individual diffusion steps have been examined to explore the impact of the system models and role of depth into the SiC for key processes.

It is determined that carbon-vacancies (V_C), which are known to be key carrier traps, have their diffusion hindered in the vicinity of a SiO_2/(0001)-4H-SiC interface, with the overall activation energy ∼15% higher in the immediate interface than two-to-three bi-layers into the SiC where they behave as in bulk SiC. It is also thought that oxidation of SiC introduces carbon interstitials to device channels, and the diffusion C_i in the vicinity of the interface with SiO_2 has also been simulated. It is found that the interface stabilises C_i even more than V_C, lower its energy by ∼1 eV relative to bulk. Such stabilisation is expected to inhibit the injection of self-interstitials into SiC.

The calculated hindering of diffusion of these native defects is consistent with a relatively high density of traps in this region, in line with experimental findings, but effective approaches to remove vacancy-related traps remains a challenging problem to be solved.

Contents

Nomenclature **xix**

1 Introduction **3**

1.1 Background 3

1.2 Properties of Silicon Carbide (SiC) 4

1.2.1 Crystal structure of SiC 4

1.2.2 Physical and electrical properties of SiC 6

1.2.3 Point defects in SiC 7

1.3 Key issues and challenges with SiC 9

1.4 Thesis Outline 13

1.4.1 Part I–Theory and Method 13

1.4.2 Part II–Applications to SiC bulk behaviour 14

1.4.3 Part III–Applications to the SiO_2/(0001)4H-SiC interface 14

1.4.4 Part IV–Conclusions 15

I Theory and Method **17**

2 Background Theory **19**

2.1 Introduction 19

2.2 The Many-Body Problem 19

2.3 The Born-Oppenheimer approximation 21

2.4 Density Functional Theory 21

2.4.1 The Hohenberg-Kohn theorem 21

2.4.2 The Kohn-Sham Equations 22

2.4.3 The exchange and correlation functional in DFT 22

2.5 Chapter Summary 24

3 Modelling of physical quantities 25

3.1 Introduction 25

3.1.1 Self-consistency cycle 26

3.1.2 Pseudopotential approximation 26

3.1.3 Basis sets functions 27

3.1.4 Supercell approach 29

3.1.5 Sampling of the Brillouin Zone 32

3.2 Derived quantities 33

3.2.1 Structural optimisation 34

3.2.2 Lattice constant and bulk modulus 34

3.2.3 Electronic structure 35

3.2.4 Formation energy and electrical levels 38

3.2.5 Diffusion barrier 40

3.3 Chapter Summary 41

II Applications 43

4 Intrinsic defect in Bulk 4H-SiC 45

4.1 Introduction 45

4.1.1 Carbon vacancies in crystalline 4H-SiC 45

4.1.2 Carbon interstitial defects in the crystalline 4H-SiC 47

4.1.3 Chapter Objectives 48

4.2 Computational method 49

4.3 Results and discussion 50

4.3.1 Modelling carbon vacancy in crystalline 4H-SiC 50

4.3.1.1 Geometrical structure 50

4.3.1.2 Role of charge states 51

4.3.1.3 Band structure and electrical level 54

4.3.1.4 Migration of V_{C} defects in 4H-SiC 55

4.3.2 Modelling of C_i defect in crystalline 4H-SiC 60

4.3.2.1 Geometrical structure of single C_i 60

4.3.2.2 Migration of $(C\text{-}C)_C$ in 4H-SiC 63

4.3.2.3 Geometrical structure of C_i pairs 65

4.4 Chapter summary 67

5 Structural models of the SiO_2/(0001)4H-SiC interfaces 69

5.1 Introduction 69

5.2 Computational Details 71

5.3 Results and Discussion 72

5.3.1 The SiO_2 bulk structure 73

5.3.2 The model of the SiO_2/(0001)4H-SiC 74

5.3.2.1 Clean interface parameters 74

5.3.3 Investigation of defects at the SiO_2/(0001) 4H-SiC 79

5.3.3.1 Model of the V_C at both non-equivalent sites 79

5.3.3.2 Migration barrier non-equivalent at both sites 79

5.3.3.3 Activation energy of the V_C with the slab thickness 81

5.4 Chapter Summary 82

6 Analysis of V_C at the SiO_2/(0001)4H-SiC interface 85

6.1 Introduction 85

6.2 Computational Method 88

6.3 Results and discussion 88

6.3.1 Modelling structures of V_C at the SiO_2/4H-SiC interface 88

6.3.1.1 V_C in the first layer 88

6.3.1.2 V_C in the second layer 91

6.3.1.3 V_C in the third layer 95

6.3.2 Diffusion of V_C through the SiO_2/4H-SiC interface layers 99

6.3.2.1 Single hop for V_C at parallel direction 99

6.3.2.2 Single hop for V_C in the c-axis 101

6.4 Chapter Summary 104

7 Carbon interstitials in the SiO_2/4H-SiC interface 105

7.1 Introduction 105

7.2 Computational Method 107

7.3 Results and discussion 107

7.3.1 Modelling of $(C\text{-}C)_C$ the at the interface 107

7.3.1.1 $(C\text{-}C)_C$ in the first layers 108

7.3.1.2 $(C\text{-}C)_C$ in the second layer 109

7.3.1.3 $(C\text{-}C)_C$ in the third layer 110

7.3.2 Diffusion of the $(C\text{-}C)_C$ interfacial layer at the interface 111

7.3.2.1 Single hop for $(C\text{-}C)_C$ at the *c*-axis 112

7.4 Chapter Summary 113

III Conclusions 115

8 Summary and Future Work 117

8.1 Conclusion 117

8.2 Future Outlook 120

List of Figures

1.1 Top and side views of Si–C structure and orientations, leading to cubic and hexagonal forms of SiC crystal lattices. 4

1.2 The sequences for the three most common polytypes of SiC. 5

1.3 Schematic images of the mechanism of the chemical reactions of the thermal oxidation process of SiC (a) before and (b) after in the SiC. Image taken from [1]. 10

1.4 Major deep levels as absorbed in deep level (n-type and p-type) SiC. Image taken from [2]. 12

1.5 DLTS spectra for as-grown n-type 4H-SiC before (dashed line) and after (solid line) oxidation at 1300°C for 1.3 h. Image taken from [3]. 12

1.6 Schematic model for the reduction of $Z_{1/2}$ and $EH_{6/7}$ centres during the oxidation process. Image taken from [3]. 13

3.1 The schematic flowchart of the self-consistent for density functional-based calculations. 27

3.2 Schematic illustration of electron wave-function and potential (dashed green line), and the pseudo-potential and resulting wave-function (solid blue line). Note that the cut-off radius r_c indicates the defined region at which point the systems must match. C_e and V_e refer to the core and valance electrons respectively. 28

3.3 Band structure of the V_{C} in 4H-SiC in the neutral charge state. The deep defect level is shown as the blue line and its dispersion is presented for the 71, and 575 atom supercells. The blue and red lines represent occupied and empty bands, respectively, with the underlying shaded areas showing the valence and conduction bands. 31

3.4 Calculated lattice constant and the computation time with different BZ sampling. These calculation are achieved to show how the Brillouin zone sampling affect the 3C-SiC modelling accuracy. 33

3.5 Band structures of 3C-SiC for using a two atom unit cell, the red and blue levels show condition band E_C and valance band E_V respectively. 37

3.6 Band structure of bulk 4H-SiC, empty and occupied bands are shown in red and blue respectively. The condition band minimum is located at M point, the valence-band maximum is at Γ-point. 37

3.7 Schematic diagram illustrating the formation energy $E^f_x(q)$, to obtain donor and accepter levels for the system x, as a function of the electron chemical potential μ_e. The dashed green and red lines obtain donor and accepter level respectively. E_{CBM} and E_{VBM} are represented to conduction and valence band respectively. 39

3.8 The schematic diagram shows shallow and deep levels of material. The orange and blue curves represent the conduction and valence bands, respectively, and the separated by the energy gap. The orange and blue shades refer to donors and acceptor levels, respectively. 40

3.9 Simple scheme representing a NEB calculation. There are three reaction pathways between two relaxed structures S_1 (initial state) and S_2 (final state) and the highest point between them is a saddle point (E_s). Whereas (E_i) represent forward energy, while (E_f) appear the forward reverse activation energy barriers. 42

4.1 Plot shows that the rotation of upper carbon layer by 60° between the cubic and hexagonal site, which appears in the local geometry in V_{C} in both sites. 51

4.2 Schematic atomic structure indicating the local arrangement of atoms in of V_C labelling the two reconstructed bonds of length N_1 and N_2. C and Si atoms are shown in grey and yellow respectively. 53

4.3 Electronic band structures of V_C bulk 4H-SiC: (a) V_C^k, (b) V_C^h. Occupied and unoccupied states are depicted as solid blue and red lines respectively, with the envelope of the band-structure for the corresponding defect-free case shown by the underlying shading. The energy scale (eV) is defined such that the valence band maxima are at zero. Only states in the region of the band-gap are plotted 56

4.4 Migration of the V_C in 4H-SiC via nearest-C-neighbour hops. The labels show the types of sites between which the hops take place. 58

4.5 Calculated migration barrier of V_C in the natural charge state including all three possible migration processes to nearest C neighbour. 59

4.6 Schematic of the carbon split-interstitial models in 4H-SiC bulk: (1) refers to the carbon-silicon split-interstitial $(\mathrm{C\text{-}Si})_\mathrm{C}$, while the positions 6 and 7 are the carbon-carbon split-interstitial $(\mathrm{C\text{-}C})_\mathrm{C}$ in *k*- and *h*-sites respectively. Position (2) refers to the hexagonal site of the carbon interstitial, which either possess a silicon-like C_{TSi} or (3) carbon-like C_{TC} surrounding. (4) site is the interstitial site in the hexagonal plane C_{Hex}. 61

4.7 Schematic of the $(\mathrm{C\text{-}C})_\mathrm{C}$ configurations in 4H-SiC: (a) in *h*-site, (b)in *k*-site. 63

4.8 Electronic band structures of single carbon split interstitial defects for $(\mathrm{C\text{-}C})_\mathrm{C}$ in the neutral state in 4H-SiC, (a) *h*-site and (b)*k*-site. 64

4.9 Minimum energy paths for $(\mathrm{C\text{-}C})_\mathrm{C}$ in bulk 4H-SiC for different charge states. 64

4.10 Schematic of di-Interstitial configurations in 4H-SiC. 66

4.11 Electronic band structures of single carbon split interstitial defects for $2\mathrm{C}_i$ in the neutral state in 4H-SiC, (a) *k*-site and (b) *h*-site. 67

5.1 Schematic diagrams showing: (a) the lattice structure of 4H-SiC. in 4H-SiC, there are two inequivalent faces are indicated by the light blue plane (*h* and *k*-face for C-face) and the light orange plane (*h* and *k*-faces for Si-face). (b) and (c) show the models for the $\mathrm{SiO_2}/(0001)$4H-SiC and $\mathrm{SiO_2}/(000\bar{1})$4H-SiC interface, respectively. 71

5.2 Schematic illustrations of SiO_2/(0001)4H-SiC. 73

5.3 Schematic diagram showing a side view of the Si-face at the SiO_2/4H-SiC interface. Grey, yellow and red atoms represent C, Si and O respectively. Relaxed atomic geometries for the SiO_2/(000$\bar{1}$) 4H-SiC interface, with: h-face and k-face. Also, the figure shows the differences in the z-position for pairs of atoms given in each layers in the interface. All distances are given in Å. 76

5.4 Schematic diagrams showing: a side view of the Si-face (0001) at the SiO_2/4H- SiC interface; grey, yellow and red atoms represent C, Si and O respectively. The 4H-SiC slab is linked with the oxide layers on the top of the slab. The (a) 204 and (b) 268-slab thickness. 78

5.5 Calculated diffusion barrier using the cNEB method for the carbon vacancy defect in both the k-face and h-face at the SiO_2/(0001)4H-SiC. V_C position in the first layer at the interface. 80

5.6 Minimum energy paths for the V_C are in the interface, while the blue, orange and yellow lines show the diffusion pathway profiles for slabs containing 203, 267 and 331 atoms, respectively. The dotted purple line represents the high barrier of bulk 4H-SiC. 83

6.1 schematic of the SiO_2/(0001)-4H-SiC interface structure used for this study: white, red, grey, and yellow, and white spheres are H, O, C and Si respectively. The numbers within the arrows indicate the layer number. 87

6.2 Schematic atomic tetrahedron structure of SiC indicating the distances of NN atoms around d1–d6 are used in tables 6.1. 89

6.3 Projection of optimised structures of the at the SiO_2/4H-SiC interface. Labels 1-7 indicate the V_C sites investigated. 90

6.4 Atomic structure indicating the local arrangement of the V_C labelling reconstructed Si–Si bond-lengths (Å) for V_C in bulk 4H-SiC and in the first carbon layers in the vicinity of a SiO_2/(0001)-4H-SiC interface, C, O and Si atoms are shown in grey, red and yellow respectively. 92

6.5 Electronic band structures of V_{C} bulk 4H-SiC and at the $\mathrm{SiO_2}$/4H-SiC interface slab: (a) V_{C}^{h*} , (b)V_{C}^{h}, and (C) V_{C}^{1}. Occupied and unoccupied states are depicted as solid blue and red lines respectively, with the envelope of the band-structure for the corresponding defect-free case shown by the underlying shading.The underlying shaded regions show the electronic band structure for the corresponding bulk 4H-SiC (128-atoms) and interface (268-atoms) The energy scale is defined such that the valence band maxima are at zero. Only states in the region of the band-gap are plotted. 93

6.6 Schematics showing wave function isosurfaces for the highest occupied bands of V_{C}^{h} and V_{C}^{1} (figure 6.5). Red and blue isosurfaces represent positive and negative wave function components, respectively. Yellow, grey and red atoms, are Si, C and O, respectively. The horizontal direction is approximately along $[1\bar{1}00]$, and the vertically upward direction is [0001]. . 94

6.7 Reconstructed Si–Si bond-lengths (Å) for V_{C} in bulk 4H-SiC and in the first carbon layers in the vicinity of a $\mathrm{SiO_2}$/(0001)-4H-SiC interface 95

6.8 Electronic band structures of V_{C} bulk 4H-SiC and at three sites in the $\mathrm{SiO_2}$/4H-SiC interface slab: (a) V_{C}^{k}, (b) V_{C}^{2}. Occupied and unoccupied states are depicted as solid blue and red lines respectively, with the envelope of the band-structure for the corresponding defect-free case shown by the underlying shading. The energy scale is defined such that the valence band maxima are at zero. Only states in the region of the band-gap are plotted. 96

6.9 Reconstructed Si–Si bond-lengths (Å) for V_{C} in bulk 4H-SiC and in the third carbon layers in the vicinity of a $\mathrm{SiO_2}$/(0001)-4H-SiC interface 97

6.10 Electronic band structures of V_{C} bulk 4H-SiC and at three sites in the $\mathrm{SiO_2}$/4H-SiC interface slab: (a)V_{C}^{h}, (b)V_{C}^{3}. Occupied and unoccupied states are depicted as solid blue and red lines respectively, with the envelope of the band-structure for the corresponding defect-free case shown by the underlying shading. The energy scale is defined such that the valence band maxima are at zero. Only states in the region of the band-gap are plotted. 98

6.11 Minimum energy path energy profiles for three layers adjacent to the SiO_2/SiC interface (solid blue lines): (a) and (c) show *hh*-process (V_{C}^1 and V_{C}^3), and (b) shows the *kk*-process (V_{C}^2). In each case the underlying red dashes show the energy profile for bulk 4H-SiC (dotted red lines). The energy scale is set to zero for V_{C}^h. Symbols show the energies obtained using the NEB method, with the lines joining them a guide to the eye. 101

6.12 Schematic of V_{C} in 4H-SiC in the neutral charge state, the saddle point structure of of V_{C}^h. The yellow and grey sites are Si and C, respectively, with the translucent spheres indicating the carbon sites between which the C atom is moving. Si sites indicated with spheres are those adjacent to the vacancy at either end of the process. 102

6.13 Calculated migration barrier of V_{C} moving between C-layers at the SiO_2/4H-SiC interface via *c*-axis direction. The first process present as the (V_{C1}) $\rightarrow$ (V_{C4}) in 4H-SiC slab, as illustrated in figure 6.3, while the seconed process; (V_{C4}) $\rightarrow$ (V_{C7}).The circles refers to the images used in the NEB calculations and The horizontal solid line indicates the diffusion of V_{C} in bulk 4H-SiC in same process. 103

7.1 Schematic of the simulated atomic structures, indicating the angles and bond lengths and angles of the (C-C)$_{\mathrm{C}}$ at: (a) first layer at the interface and (b) the 4H-SiC bulk. Grey, red and yellow atoms represent C, O and Si atoms, respectively. 109

7.2 Schematic of the simulated atomic structures indicating the angles and bond lengths and angles of the (C-C)$_{\mathrm{C}}$ at: (a) the second layer at the interface and (b) the 4H-SiC bulk. Grey, red and yellow atoms represent C, O and Si atoms, respectively. 110

7.3 Schematic of the simulated atomic structures indicating the angles and bond lengths and angles of the (C-C)$_C$ at: (a) the third layer at the interface and (b) the 4H-SiC bulk. Grey, red and yellow atoms represent C, O and Si atoms, respectively. 111

7.4 illustration of (C-C)$_C$ diffusion at the SiO_2/4H-SiC interface: (1) the initial step (in *k* site); and (2) the final step (in *h* site) between first and second layers in 4H-SiC slab. while (3)(in *h* site) and (4) (in *k* site) step. This shows the diffusion process of (C-C)$_C$ between the initial (3) and final (4) structures. 113

7.5 Minimum energy paths for in bulk 4H-SiC (dashed red) and interfaces (solid blue). To facilitate comparison, the zero on the energy scale is defined as the *k*-site energy at the end of the process.1-4 are as indicated in the labelling of figure 7.4. 114

List of Tables

1.1 Structural characteristics of common SiC polytypes [4]. 6

1.2 Comparison of physical properties of SiC and Si at room temperature [2, 4]. 7

2.1 Energy band gap E_g and lattice parameters a_0 for 3C-SiC calculations by using LDA. This result is compared with theoretical and experimental values [5, 6] and shown here for the comparison. 23

3.1 Calculated lattice constant and time as a function of the number of Gaussians by using to describe 3C-SiC basis sets for a primitive SiC cell. 30

3.2 Calculated lattice constant by using different basis sets for a primitive SiC cell. Numbers refer to the basis sets listed in table 3.1. 30

3.3 Structure properties of 3C- and 4H-SiC was calculated by using DFT in comparison with other studies. All energies in eV. 35

3.4 Comparison of band gap of 3C-SiC and 4H-SiC as well as other theoretical and experimental results. All energies in eV. 36

4.1 The energy difference (eV) between the V_C^h and V_C^k site from this study and from literature with different supercell sizes. 52

4.2 Reconstructed Si–Si bond-lengths (Å) for V_C in bulk 4H-SiC in different charge states at both the *h*- and *k*-site, relative to the Si-Si distance in pure 4H-SiC (3.05–3.06 Å within our computational approach) as indicated in figure 4.2. Values in parentheses indicate the reduction in distance as a percentage of the pure 4H-SiC reference distance. 54

4.3 Activation energies (eV) for the migration of V_C by nearest C-neighbour hops for different charge states. 57

4.4 Bond lengths Å of the neutral carbon $(C\text{-}C)_C$ in 4H-SiC. The indices of the atoms refer to figure 4.7,and values in parentheses indicate a reference [7]. . 62

4.5 Bond lengths of the neutral carbon $(C\text{-}C)_C$ for di-interstitial configurations in the 4H-SiC lattice. The indices of the atoms refer to figure 4.10. 66

5.1 Calculated (Current calculations), experimental and theoretical values of the lattice parameters (a_0 and c) (Å), the bond-length (Å) and the bond-angle of the SiO_2. The theoretical data and experimental is taken from previous studies. 74

5.2 The atomic geometry of the 4H-SiC interface for the structure, compared to the ideal 4H-SiC bulk structure, where d_{ij} refers to the distance between interface layers numbers, while z_{13} refers to the distance between the positions of two atoms in different layers, as shown in figure 5.3. The negative sign refers to a contraction and the positive sign indicates an expansion of the interlayer spacing. All distances are given in Å. 77

5.3 Range and standard deviation (SD) for the Si-face displacements of the Si atoms in the SiC bonded to the first layer of the SiO_2 as a function of the vacancy location. All values in the table are in Å. 79

5.4 The effect of slab thickness (number of Si-C layers) on the total energy difference of V_C between two neighbouring sites of carbon layers in the vicinity of a SiO_2/(0001)4H-SiC interface interface, as indicated in the figure 5.4, ($V_{C_{ii}}$ indicate the vacancies in the ii layer (odd layers are h-site and even k- site). 82

6.1 Relaxation around the V_C in 4H-SiC given in (%), compared to the ideal tetrahedral distance between NN silicon atoms V_C. Distances $d1$–$d6$ are labelled according to figure 6.2. These values indicate how much each of the the other sites were higher (positive) or lower (negative), relative to the Si–C distance in pure 4H-SiC (3.06 Å) in our computational approach). 89

6.2 The energy differences $\triangle E$ in (eV) associated with the different sites of V_C.The position of V_C as examined for the sites are illustrated in figure 6.3 90

6.3 Range and standard deviation (SD) of the Si- atoms in the [0001] displacements in the SiC bonded to oxygen in the SiO_2 as a function of the position of the V_C, all values in Å 97

6.4 Possible migration pathways for single V_C. The activation energy differences $\triangle E$ in (eV) associated with the different sites of V_C in the bulk. These values indicate how much each of the other sites is higher than the reference (in both both h-site and k-site in bulk 4H-SiC). The position of V_C as examined for the sites is illustrated in figure 6.3 100

Publications and Conferences

List of Publications

1. **Hind Alsnani**, J. P. Goss, P. R. Briddon, M. J. Rayson, A. B. Horsfall, "Carbon-vacancy migration near the SiO_2/4H-SiC interface", 12th European Conference on Silicon Carbide and Related Materials (ECSCRM2018), Birmingham, UK, September 2018.
2. **Hind Alsnani**, J. P. Goss, P. R. Briddon, M. J. Rayson, A. B. Horsfall, "Investigation of carbon interstitials in the vicinity of the SiO_2/4H-SiC(0001) interface", International Semiconductor Conference (CAS), Romania, 2018.
3. **Hind Alsnani**, J. P. Goss, P. R. Briddon, M. J. Rayson, A. B. Horsfall, "First principles study of the stability and diffusion mechanism of a carbon vacancy in the vicinity of a SiO_2/4H-SiC interfacel", Gettering and Defect Engineering in Semiconductor Technology (GADEST, Germany, 2019

List of Conferences

1. Oral Presentation "Physical Trends of Carbon Vacancy in 4H-SiC", Annual Research Conference (ARC2015), Newcastle University, UK, 2017.
2. Poster Presentation "The mechanism of carbon-vacancy diffusion at the SiO_2/4H-SiC interface", in 12th European Conference on Silicon Carbide and Related Materials (ECSCRM), Birmingham, UK, 2018.
3. Oral presentation "Investigation of carbon interstitials in the vicinity of the SiO_2/4H-SiC(0001) interface", International Semiconductor Conference (CAS), Romania,

2018.

4. Poster Presentation “Carbon-vacancy migration near the SiO_2/4H-SiC interface”, a meeting of High–Performance–Computing applied to materials (N8 PHC network event), York, UK, 2018.

5. Poster Presentation “A comparative study of diffusion of carbon vacancies at the *h*- and *k*-(0001)-faces at the SiO_2/4H-SiC interface”, a meeting of High–Performance–Computing applied to materials (N8 PHC network event), York, UK, 2019.

6. Poster Presentation “Diffusion of the carbon vacancy within *h*-and *k* -layers at the SiO_2/(0001)-4H-SiC interface”,Conference on Energy Materials and Interfaces (NECEM 2019), Newcastle, UK, 2019.

7. Poster Presentation “First principles study of the stability and diffusion mechanism of a carbon vacancy in the vicinity of a SiO_2/4H-SiC interface”, Hind Alsnani, J. P. Goss, P. R. Briddon, M. J. Rayson, A. B. Horsfall , Gettering and Defect Engineering in Semiconductor Technology (GADEST), Germany, 2019.

Prizes

1. **Annual Research Conference 2018**, 27–29 January 2018, School of Engineering, Newcastle University, Newcastle upon Tyne, U.K.,“The mechanism of carbon-vacancy diffusion at the SiO_2/4H-SiC interface”. **First place for best Presentation Award**.

Glossary

The following tables list the abbreviations and symbols used in this thesis.

Symbols

Notation	Definition
E_g	Band gap energy.
C_i	Carbon interstitial defect.
V_{C}	Carbon vacancy defect.
V_{C}^{k}	Carbon vacancy in cubic-site.
V_{C}^{h}	Carbon vacancy in hexagonal-site.
V_{C}^{hf}	Carbon vacancy in hexagonal-face.
V_{C}^{kf}	Carbon vacancy in cubic-face.
μ_i	Chemical potential of atom species.
$n(r)$	Charge density.
q	Charge state.
E_{CBM}	Conduction band bottom.
$2\mathrm{C}_i$	Di-interstitial defects.
E_{VBM}	Valence band top.
μ_e	Electron chemical potential.
E_x^f	Formation energy for the system x.
E^F	Fermi energy.
T	Temperature.

Abbreviations

Abbreviation	Definition
AIMpro	*Ab Initio* Modelling PROgram.
BZ	Brillouin zone.
CB	Conduction band.
NEB	Nudged elastic band.
DFT	Density functional theory.
DLTS	Deep level transtor spec
GGA	Generalised gradient approximation.
EPR	Electron paramagnetic resonance.
H-K	Hohenberg-Kohn
HS	Kohn Sham.
HGH	Hartwigsen-Göedecker-Hutter.
HRTEM	High-resolution transmission electron microscopy.
LDA	Local density approximation.
LDF	Local density functional.
MOSFET	Metaloxidesemiconductor field-effect transistor.
MP	Monkhorst-Pack.
NEB	Nudged elastic band.
NN	Next neighbour
PL	Photoluminescence.
SC	Self consistent.
VB	Vacuum banb.

Chapter 1

Introduction

1.1 Background

Semiconductor-based technology is becoming extremely important to modern life, as we are increasingly dependent on electronic appliances [1]. Major applications of such technology include robotics, domestic appliances, and more recently, sustainable technology, and electric cars [1]. Silicon (Si) is a commonly used material due to its low extraction cost and abundant availability in the Earth's crust [8, 1]. However, in recent years, with the rapid development of materials and advances in material processing technology, there has been an increasing need for a material which can operate at temperatures of around 200°C and above. The operating temperature range of Si is relatively limited, with a maximum close to 175°C [4, 2]. One of the better alternatives to silicon for the semiconductor industry is silicon carbide (SiC), which exhibits superior physical and chemical properties. However, SiC is limited in availability compared to pure silicon.

Berzelius first discovered silicon and carbon in 1824 [9], and in 1892 an American chemist discovered SiC from silica [9]. However, no techniques for controlling crystal growth were available at that time, and there were great challenges in the production of high quality SiC crystals. These challenges significantly reduced the ability to work with SiC materials [10]. This situation continued until 1955, when a breakthrough method for producing relatively pure SiC in the laboratory was discovered by Jan Anthony Lely [11].

This led to the development of the Lely method [11, 12], process that is still used today. Much later, in the 1970s, a novel method based on seeded sublimation growth was developed by Tairov and Tsvetkov [13]. This method allowed the researchers to produce SiC wafers for the first time, and since then, there has been a fast-growing interest in this material, given the great importance of SiC in high-power devices. In the next section, more details are presented on the structure of SiC.

1.2 Properties of Silicon Carbide (SiC)

1.2.1 Crystal structure of SiC

Silicon carbide structure is comprised of carbon and silicon atoms that mutually surround each other. The C-Si bond length is found to be around 1.88 Å, which places it between the bond lengths of bulk silicon (2.35 Å) and diamond (1.55 Å). There are two possible orientations for the neighbouring SiC bilayers that exist in SiC crystals [14]. In the first orientation, the top layer of Si, C tetrahedra conforms with the bottom layer, resulting in a cubic zincblende structure. In the second arrangement, the Si–C bonds of the top layer are rotated by 60° relative to the bottom layer, leading to a hexagonal wurtzite structure, as shown in figure 1.1.

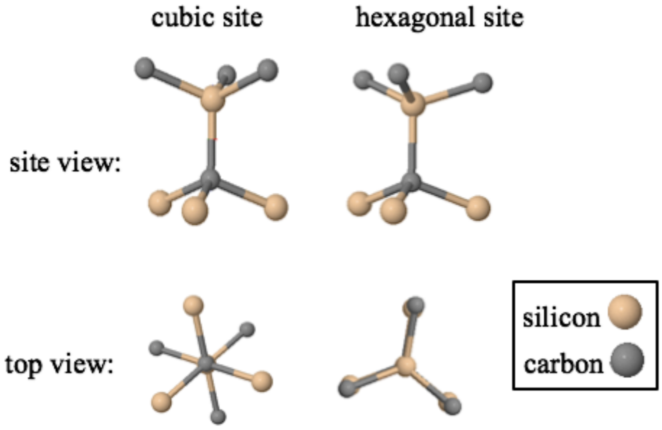

Figure 1.1: Top and side views of Si–C structure and orientations, leading to cubic and hexagonal forms of SiC crystal lattices.

SiC crystals can exist in many different structural formations: the so-called polytypes. More than 200 polytypes of SiC have been discovered to date [15] and are a result of the different stacking sequences of the atoms (figure 1.2). The three configurations of Si and C layers are denoted by A, B and C [16]. The atom locations in the hexagonal polytypes are classified as cubic sites (k) or hexagonal sites (h), according to Ramsdell notation [16], after the scientist who discovered the differences between the polytypes and distinguished them by using a number and a letter. The number refers to the number of double layers in the unit cell, while the letter indicates the structural type, *e.g.* C, H and R to represent cubic, hexagonal, and rhombohedral, respectively.

The most common types are illustrated in figure 1.2. For the case of cubic polytypes that exhibit the stacking sequence ABC, all the atoms residing in the hexagonal polytypes contain AB in their stacking sequences, as shown in table 1.1. The data show that 2H-SiC has a 100% hexagonal structure, while 3C-SiC has a 100%; cubic structure, with other polytypes containing a varying mixture of the two structures. Increasing the number of Si–C bilayers controls the effect of the hexagonality of the different polytypes. These results are summarised in table 1.1. The values confirm the tendency that the percentage of double hexagonal layers decreases to 50% per unit cell in 4H-SiC due to equal numbers of hexagonal and cubic sites, while in 6H-SiC one third of the lattice sites are hexagonal.

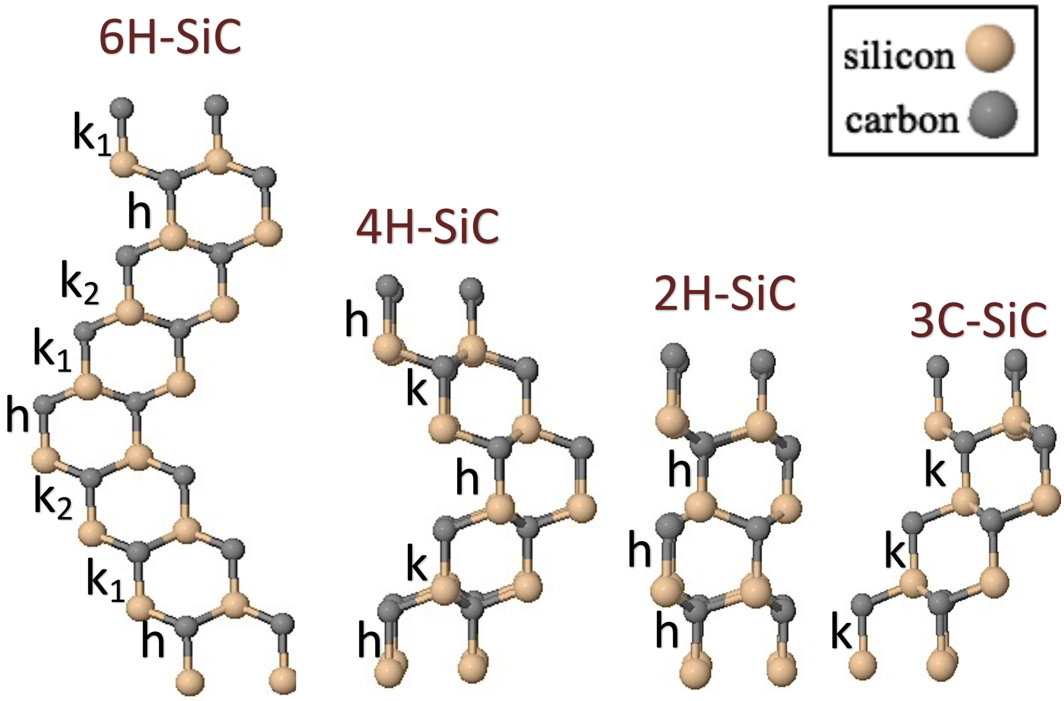

Figure 1.2: The sequences for the three most common polytypes of SiC.

SiC polytypes	stacking sequence	Lattice constant	hexagonally %
2H	AB	$a_0 = 3.1\,\text{Å}$ $c = 5.0\,\text{Å}$	100
4H	ABCB	$a_0 = 3.0\,\text{Å}$ $c = 10.0\,\text{Å}$	50
6H	ABCACB	$a_0 = 3.1\,\text{Å}$ $c = 15.1\,\text{Å}$	33
3C	ABC	$a_0 = 4.3\,\text{Å}$	0

Table 1.1: Structural characteristics of common SiC polytypes [4].

1.2.2 Physical and electrical properties of SiC

Silicon carbide material parameters provide credibility for the claim that it is superior choice for high-power device applications. The breakdown field of SiC is greater than that of silicon [17, 4], which enables the fabrication of very high-voltage, high-power devices [17]. One clear advantage is that SiC has a wide band gap (2.3–3.2 eV), which is two to three times higher than that of silicon (1.2 eV). This increased band gap results in SiC continuing to behave as an intrinsic semiconductor at temperatures close to 1000°C, in comparison to 150°C for Si [10]. This makes SiC very suitable for high-temperature applications, and a number of functional devices have been demonstrated at temperatures beyond 1000°C [4]. The table 1.2 summarises the electronic and material properties of SiC polytypes as compared with silicon.

Another advantage of SiC is its ability to present a stable native oxide in order to form silicon dioxide (SiO_2) [12]. This fact makes the device fabrication process much less complicated. Table 1.2 also shows the difference in the band gap between the polytypes, which is a consequence of the different physical and electrical properties influencing the number of electronic and vibrational levels of the material. 4H-SiC is considered to be the most suitable for electronic applications due to its higher band gap and higher carrier mobility in comparison to 6H. 4H-SiC also has a lower mobility anisotropy, increasing its suitability for both vertical and lateral structures. However, this extremely important technology has its own share of problems that limit its efficiency and functionality. The SiC crystal

Property	Si	3C-SiC	4H-SiC	6H-SiC
Band-gap (eV)	1.2	2.3	3.2	3.0
Lattice constant (Å)	2.3	3.4	$a_0 = 3.0$	$a_0 = 3.1$
			$c = 10.0$	$c = 15.1$
Breakdown field (MV/cm)	0.3	2.0	3.0	3.0
Electron Mobility (cm^2/Vs)	1350	1000	1000 ($\perp c$)	450 ($\perp c$)
			1200 ($\parallel c$)	100 ($\parallel c$)
Thermal conductivity (W/cm,K)	1.5	4.9	4.9	4.9

Table 1.2: Comparison of physical properties of SiC and Si at room temperature [2, 4].

structure has a large array of impurities and defects [7, 2, 18, 19, 20, 5, 21, 22, 23, 24, 25]. The biggest challenge in fully utilising the capacity of SiC devices is the difficulty in obtaining a high power density. A number of issues are responsible for this. In the following sections, these defects and impurities will be discussed in detail. Furthermore, the high density of the interface states (D_{it}) results in a poor surface electron mobility [2], with the effective mobility being reduced by the interface states and Coulomb scattering during the oxidation processes in the growth of SiC [26, 17, 18, 27]. A large number of traps become filled during inversion, causing Coulomb scattering of mobile charges and a decrease in effective mobility. Understanding the nature of these defects in bulk SiC will enable the identification of technologically feasible methods to eliminate them and improve the channel mobility of SiC metal-oxide-semiconductor-field-effect transistors (MOSFETs).

1.2.3 Point defects in SiC

SiC possess a high concentration of impurities and defects than other Si materials. These abnormalities are unintentionally incorporated during processing of the materials or at the growth stage [17]. Primarily, there are three types of point defects reported in literature as due to the fact of two different atom types. These defects are explained as follows:

Firstly, a point defect can be formed due to a vacancy created by removing either a carbon (V_{C}) or a silicon atom (V_{Si}). The space left due to the missing atom can also be occupied by any other atom type (Si_{C} or C_{Si}). and this gives rise to the second type of point defect. In the third type, an atom can occupy a non-lattice site between the existing atoms [28]. The atoms may be displaced from anywhere in the lattice and commonly occur during the growth process [29].

A comprehensive study on the properties of the intrinsic point defect of 4H-SiC is pending. This would further our understanding of the electronic properties of SiC-based semiconductors [29]. The vacancies and interstitials are the most fundamental defects that are produced during the ion irradiation and annealing processes [29]. The formation energy of a V_{C} defect is reported to be lower in comparison to the V_{Si} defect in SiC lattice [29, 30]. As a consequence, a vacancy is understood to move through the SiC lattice by direct migration of atom of same type from a neighbouring site and lead to an activation energy of 3.6 eV [29]. In contrast, V_{Si} defects exhibit metastable behaviour and can convert to a complex state. This state is made from the carbon vacancy and the carbon anti-site complex V_{C}-C_{Si} during the diffusion process [31] and leads to a high activation energy of 4.6 eV [29]. Therefore, It has been established that the diffusion processes that are based on the silicon vacancies will be inherently more complicated than those involving carbon vacancies. In this thesis, the origins of various defect signatures will be studied by exploiting selectively created point defects that are related to the carbon atom.

Another primary defect related to an intrinsic defect in the bulk 4H-SiC is the carbon interstitial C_i. A wide range of structure configurations of carbon interstitials in 4H-SiC, as have been previously been explored [32, 29], but the most stable carbon interstitial forms a short bond with direct carbon neighbours ($(\mathrm{C{-}C})_i$ configuration defect) [33, 29, 34, 32]. An overview of carbon vacancy and interstitial defects in crystalline 4H-SiC is presented, as described in more detail in chapter 4.

Doping is a well-established process to enhance material properties, however the process often leads to an increase of impurities or defects [35, 29]. Specifically doping helps to improve the conductivity of pure SiC by two primary routes: firstly, the addition of extra electrons to SiC is carried with an element that has five valence electrons (negative charge carriers), such as nitrogen (N) adding an extra electron to the SiC structure. This addition of a bonding electron is called n-type doping. secondly, the SiC lattice can be doped with aluminium (Al), which has three valence electrons (positive charge carriers), producing an extra hole and is called the p-type doping [35]. The impurities arising from the doping process lead to an introduction of additional electronic states into the SiC band gap. In the case of *n*-type SiC, the introduced energy level position is close to the conduction band (CB), while the *p*-type SiC introduces a level near to the valence band (VB). This will be presented in more depth in chapter 4.

Defects in SiC can be experimentally observed using various techniques, a few of which are:

1. Photoluminescence spectroscopy (PL), which is based on the identification optical transition between spatially localised defect [7].
2. Deep-level transient spectroscopy (DLTS), based upon the principle of measuring the transient capacitance of the electron transfer from the deep level into the CB [17, 29].
3. Electron paramagnetic resonance (EPR) method, used to identify species which have unpaired electrons [20].

In order to widen our understanding of the above listed bulk defects, literature have explored quite a few experimental techniques but limited to provide only averaged information for large number of defects. However, they fail to provide an understanding that describes the microscopic origin of the defects [29]. Theoretical and validated computational models based on density functional theory (DFT) techniques have been explored and matched against experimental [29] observations to provide quantitative data relating to the structure, electrical properties and migration energetics of the defects [29]. Similar computational approach based on DFT is undertaken in this thesis. The details of the implementation and the underlying theory are presented in chapters 2 and 3.

1.3 Key issues and challenges with SiC

Electronic devices have been manufactured with a technology heavily based on 4H-SiC materials with SiO_2 as its native oxide. A significant challenge arise due to quality or purity of 4H-SiC material: high defect density at the 4H-SiC interface is observed than for Si interfaces (a difference of two orders of magnitude) [36]. These defects lead to charge trapping and/or Coulomb scattering and therefore inefficient devices [26]. Reducing the defect density in SiC interfaces remains a challenging prospect due to a lack of underlying theory explaining the origins of these considerable differences in defect density [37].

Ubiquitous process of SiC oxidation exacerbates the problem of commonly present carbon-related defects [38]. In effect, this means that carbon accumulates during the conventional post-growth process steps (post-implantation annealing and oxidation) and further SiC oxidation produces extra defects, leading to added complexity [39, 40, 3].

Furthermore, the formation of SiO_2 leads to removal of carbon and the formation and outgassing of volatile species such as CO and CO_2 [41], as shown in figure 1.3. As a result, a small volume of C remains close to the SiC interface, according to equation 1.1 [1].

$$\mathrm{SiC} + \mathrm{O_2} \rightarrow \mathrm{SiO_2} + \mathrm{C} \tag{1.1}$$

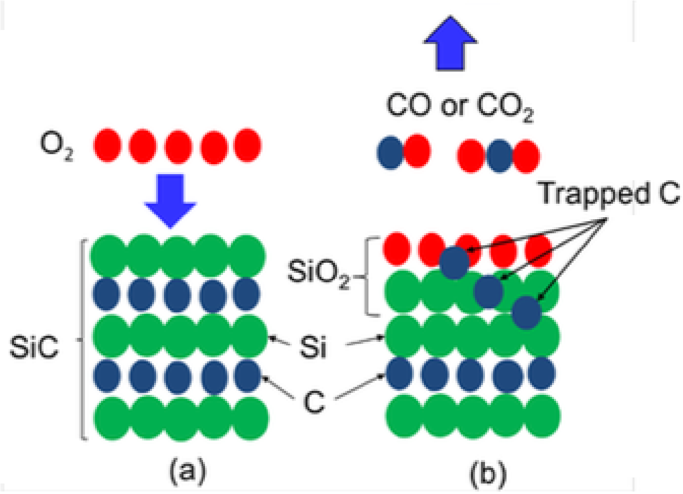

Figure 1.3: Schematic images of the mechanism of the chemical reactions of the thermal oxidation process of SiC (a) before and (b) after in the SiC. Image taken from [1].

Experimental findings suggest that a large density of interface traps D_{it} is mostly present in the lower part of the interface SiC band gap. The high density of interface states result in a poor surface electron mobility, with the effective mobility being reduced by interface-states and coulomb scattering [3]. A large number of trap are filled during inversion, causing the coulomb scattering of mobile charges and decreasing the mobility [12].

Recent computational studies by Deák *et al.* focused on several oxidation paths.

Their calculations indicated that the carbon related defects are a possible origin of the high density traps, as carbon interstitials are expected to appear as carbon dimers or as carbon small clusters, but not large carbon structures [42]. This study further proposed that the split interstitial defect also gives rise to a deep-level state in the band gap (discussed in chapter 5). Other sources of interface traps that have been suggested as contributing to D_{it} is the carbon vacancy [42].

Experimental data indicate that $Z_{1/2}$ centre is linked to the concentration of carbon vacancies in the material, which are incorporated as a consequence of the growth conditions. Data reported in the literature show a reduction in the concentration of the $Z_{1/2}$ centre after both C^+ implantation and thermal oxidation, which is known to create carbon interstitials within the SiC [3]. The centre is a major deep level in n-type 4H-SiC and is a dominant carrier-lifetime killer [2, 10, 43]. These defects have been previously observed by several experimental studies using techniques based on DLTS. Other common defects in as-grown material include the centre are shown schematically in figure 1.4. The study of the origin, stability and structure of the defect can be used to make recommendations to crystal growers. The first objective of this thesis is to confirm whether the and defects are directly related to the existence of carbon vacancies in different charge states, as has recently been hypothesised [44, 19].

As illustrated in figure 1.5, defects may well originate from the same defect, V_{C}, and data obtained from EPR correlates well with those determined by DLTS.

Conventional post-growth process steps (post-implantation annealing and oxidation) have been shown to reduce the concentration of these as-grown defects [4, 45, 3]. DLTS data have previously shown that thermal oxidation and ion implantation play a key role in the evolution of deep-level centres in as-grown SiC epilayers, as shown in figure1.5. Hiyoshi and Kimoto [27] investigated the behaviour of defects during the thermal oxidation of SiC epilayers, as illustrated by the DLTS data in figure1.5. They hypothesised that surplus carbon atoms (which are produced at the SiC interface during the formation of SiO_2) diffuse into the bulk, filling the carbon vacancies and leading to the observed reduction of and centres[27].

Based on these previous studies, a major aim of the current research is to clarify the structure and origin of DLTS centres, which are believed to originate from C-related

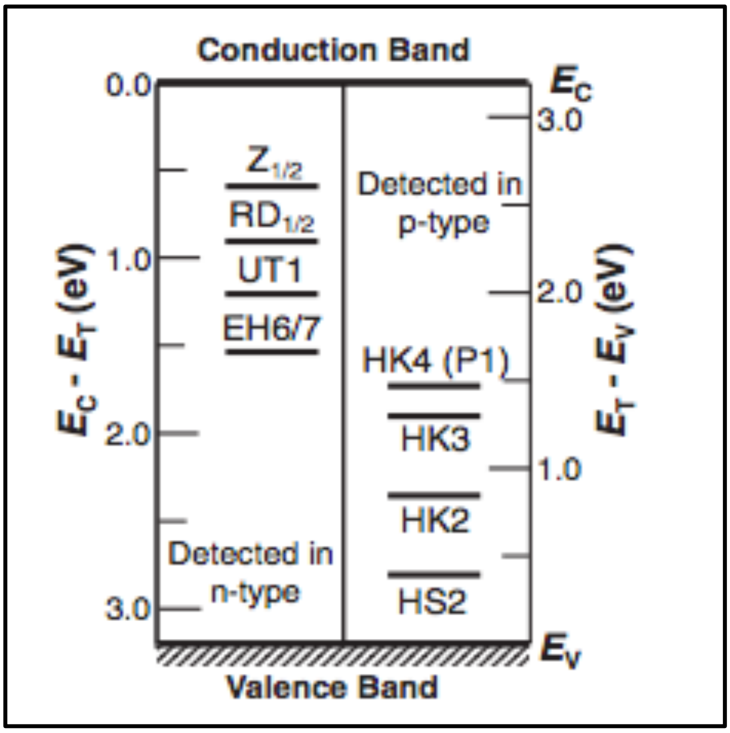
Conduction Band
Valence Band
E_C
E_V
$E_C - E_T$ (eV)
$E_T - E_V$ (eV)
0.0
1.0
2.0
3.0
3.0
2.0
1.0
$Z_{1/2}$
$RD_{1/2}$
UT1
EH6/7
Detected in n-type
Detected in p-type
HK4 (P1)
HK3
HK2
HS2

Figure 1.4: Major deep levels as absorbed in deep level (n-type and p-type) SiC. Image taken from [2].

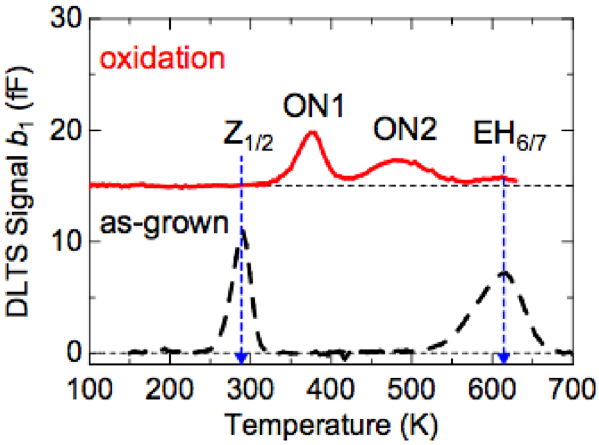

Figure 1.5: DLTS spectra for as-grown n-type 4H-SiC before (dashed line) and after (solid line) oxidation at 1300°C for 1.3 h. Image taken from [3].

defects as a result of thermal oxidation. Experimental data indicate that these defects are linked to the concentration of carbon vacancies in the material [2]. Knowledge of the physical structure of these defects will be critical in optimising the behaviour of high-performance electronic devices that use ion implantation and oxidation in their fabrication, such as MOSFETs.

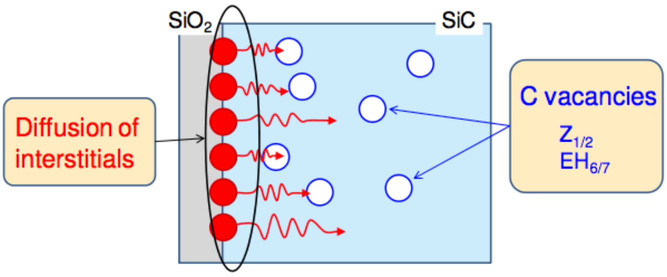

Figure 1.6: Schematic model for the reduction of $Z_{1/2}$ and $EH_{6/7}$ centres during the oxidation process. Image taken from [3].

1.4 Thesis Outline

This thesis is divided into three major parts:

1. An outline of the theoretical formulation of DFT and its implementation using AIMpro modelling;
2. Application of the AIMpro software to understanding carbon vacancy and interstitial defects in the SiC bulk.
3. The defects at the SiO_2/(0001)4H-SiC interface.

Each part is divided into chapters, and a summary of the contents of each chapter is as follows.

1.4.1 Part I–Theory and Method

Chapter 2: Fundamental theories This chapter provides an overview of the computational quantum method of density functional theory (DFT), as implemented in the *Ab Initio* modelling program AIMpro. This is used to obtain the total energy of a system as a function of charge density. DFT can further be used to derive the properties of systems such as solids, molecules and atoms in the ground state.

Chapter 3: Modelling of physical quantities This chapter presents an introduction to the AIMpro software, including the methods and approximations adopted for the calculation of experimental observables. The physical quantities and primary converged parameters used to simulate the pure SiC structures for both 3C- and 4H-SiC are also presented, along with the main quantities that have been tested to study the accuracy of the computational procedure adopted in the application of this thesis. These include modelling parameters such as the choice of lattice constant, wave function basis and Brillouin zone sampling.

1.4.2 Part II–Applications to SiC bulk behaviour

This part summarises the results obtained from AIMpro modelling of the SiC bulk structure.

Chapter 4: Intrinsic defect in bulk 4H-SiC This chapter focuses on the analysis of carbon vacancies to understand how the defects move through the SiC lattice by the direct movement of the same type of atom from a neighbouring site. Since there are two non-equivalent forms of V_{C}, there are multiple diffusion pathways that the vacancy might move through. This depends on whether the vacancy is initially located at a cubic (k) or hexagonal (h) site, and where it ends up.

Furthermore, the carbon interstitials (C_i) defects in pure 4H-SiC are presented in this chapter. This includes studying their geometric and electronic structure and investigating the different forms of carbon interstitials that can occur at either h- or k-sites. Also included in this chapter is the calculation of the activation energies of carbon interstitials for the barriers that are associated with the transfer of a carbon atom from the surface to different site in 4H-SiC.

1.4.3 Part III–Applications to the SiO_2/(0001)4H-SiC interface

Chapter 5: Structural models of the SiO_2/4H-SiC interface This chapter presents an investigation of the model for the 4H-SiC interface to obtain the effects of various modelling parameters: the choices of converged parameters for the slab calculations. Further, the first-principles calculations were performed on the 4H-SiC interface including examination of the geometric differences between *h*-face, *k*-face, Si-face and C-face at the interfaces. In addition, the differences in 4H-SiC carbon vacancy occurring at either *h*- or *k*-faces have been investigated.

Chapter 6: Analysis of V_C at the 4H-SiC(0001) interface Based on the fundamental calculations highlighted in 4, this chapter focuses on the analysis of the diffusion of V_C defects in a more complex environment in the vicinity of the 4H-SiC interface. The chapter outlines the migration of carbon vacancy defects at the interface that were discussed in chapter 5. This includes the calculation of the activation energies for the barriers associated with the transfer of a carbon vacancy from the surface to the different sites in the 4H-SiC slab. The migration of carbon vacancies is examined in two directions: the basal plane and *c*-axis directions of the 4H-SiC slab. Finally, the migration of carbon for both vacancies and interstitial defects is presented and compared with the results described in chapter 4.

Chapter 7: Carbon interstitials in the $\mathrm{SiO_2}$/4H-SiC interface Based on the fundamental calculations highlighted in chapter 6, this chapter focuses on the analysis of diffusion of $(\mathrm{C\text{-}C})_i$ defects in the vicinity of the 4H-SiC interface and presents a comparison with the bulk SiC results (chapter 4). The calculation of the activation energies for the barriers associated with the transfer of a carbon atom from the surface to different sites in 4H-SiC slab is included in this chapter. The migration of the carbon spilt-interstitial is examined in the *c*-axis direction of the 4H-SiC slab. Finally, the migration of carbon interstitial defects is presented, alongside the results of the impact of the migration of carbon spilt- interstitials in the vicinity of an the $\mathrm{SiO_2}$/4H-SiC interface.

1.4.4 Part IV–Conclusions

Chapter 8: Conclusions and future work In the final chapter, the general conclusions are presented alongside suggestions for future research.

Part I

Theory and Method

Chapter 2

Background Theory

2.1 Introduction

For a stationary system with a number of interacting electrons, the quantum-mechanical behaviour can be adequately described by calculating its many-electron wave function. In principle, this can be achieved by solving the Schrödinger equation; however, the equation is hard to solve analytically because the motion of a single electron is determined by all the other electrons present in the system. Progress requires same approximations and a numerical approach. The content in this chapter aims at gives the reader an introduction into density functional formalism theory and the main concepts therein. It will provide, albeit in brief terms, a presentation of the important approximations incorporated in the *Ab Initio* modelling program [46] AIMpro.

2.2 The Many-Body Problem

The fundamental task behind the DFT method is to find the solution to an approximation to many-body Schrödinger equation for the system which is under study. The time independent Schrödinger equation (SE), can be represented in the following way:

$$\hat{H}\Psi(r) = E\Psi(r) \tag{2.1}$$

where, E represents the total energy of the system, $\hat{H}$ is the Hamiltonian operator and Ψ refers to a function of the electron, coordinates and nuclear positions.

$$\Psi = \Psi(r_1, r_2, ...; R_1, R_2, ...) \tag{2.2}$$

where, $(r_1, r_2, , ...r_n)$ indicate to the electrons' coordinates, while $R_1, R_2, ...R_N$ refer to the coordinates of the nuclei of masses $M_1, M_2, ...M_N$. The Hamiltonian operator describes both the kinetic (T) and potential energies (V) of the electrons or nuclei and can be described in form of an equation 2.3.

$$\hat{H} = \hat{T}_n + \hat{T}_e + \hat{V}_{n-n} + \hat{V}_{n-e} + \hat{V}_{e-e} \tag{2.3}$$

The kinetic terms $\hat{T}_n$ and $\hat{T}_e$, represent the kinetic energy of nuclei and electrons, respectively. As shown in equation 2.3, there are three types of interactions: the Coulomb potentials of nuclear-nuclear $\hat{V}_{n-n}$, the electron-electron interactions $\hat{V}_{e-e}$, and the attractive Coulomb potential of electron-nuclear $\hat{V}_{e-n}$. The Hamiltonian operator in the Schrödinger equation can be written as:

$$\begin{aligned} H = & - \sum_{i=1}^{n} \frac{\hbar^2}{2m_e}\nabla_i^2 - \sum_{A=1}^{N} \frac{\hbar^2}{2M_A}\nabla_A^2 - \sum_{i=1}^{n}\sum_{A=1}^{N} \frac{Z_A e^2}{4\pi\varepsilon_0 r_{iA}} \\ & + \sum_{i=1}^{n}\sum_{j>i}^{n} \frac{e^2}{4\pi\varepsilon_0 r_{ij}} + \sum_{A=1}^{N}\sum_{B>A}^{N} \frac{Z_A Z_B e^2}{4\pi\varepsilon_0 R_{AB}} \end{aligned} \tag{2.4}$$

where

$$r_{ij} = |r_i - r_j|, \quad r_{iA} = |r_i - R_A|, \quad R_{AB} = |R_A - R_B|. \tag{2.5}$$

Here, A and B are the nucleus and $|r_i - r_j|$ is the distance between electrons i and j, $|r_i - R_A|$ is the distance between electron j and nucleus A, while A refers to the nuclei charge of atom A. The parameters e, $\hbar$, $4\pi\varepsilon_0$, m_e are equal to (1 au)in the atomic system of units. The Hamiltonian can be expressed as in equation 2.6.

$$\hat{H} = \overbrace{\sum_{i=1}^{n} \frac{1}{2}\nabla_i^2}^{(1)} - \underbrace{\sum_{A=1}^{N} \frac{1}{2M_A}\nabla_A^2}_{(2)} - \overbrace{\sum_{i=1}^{n}\sum_{A=1}^{N} \frac{Z_A}{r_{iA}}}^{(3)} + \underbrace{\sum_{i=1}^{N}\sum_{j>i}^{N} \frac{1}{r_{ij}}}_{(4)} + \overbrace{\sum_{A=1}^{n}\sum_{B>A}^{N} \frac{Z_A Z_B}{R_{AB}}}^{(5)} \tag{2.6}$$

The first and second terms of equation (2.6) refer to the kinetic energy of the electrons and the nuclei, while the third part contain the nuclear coulombic attraction between the j^{th} nucleus and the i^{th} electron. The fourth term refers to the electron coulombic repulsion between the i^{th} and j^{th} electrons, and the final term represents the nuclear coulombic repulsion between the A^{th} and the B^{th} nucleus. Finding practical methods to solve the Hamiltonian expressed in equation 2.6 is extremely difficult. Therefore, it is necessary to make additional approximation and assumptions to simplify this equation. To this end, an assumption can be made to make the motions of electrons and nuclei independent. The approximations were first achieved by Born and Oppenheimer [47] and are widely used; these as described in next section.

2.3 The Born-Oppenheimer approximation

This approximation is applied by separating the nuclear and electronic terms in the Schrödinger equation. In this approach, the nuclei of the system are seen as fixed, depending on the electrons' small mass and faster motions compared to the mass and motions of nuclei. Therefore, according to this approximation, the kinetic energy team of the nuclei in the Hamiltonian equation 2.3, can be removed, leaving the electronic Hamiltonian can be written as in equation 2.7:

$$\hat{H} = \hat{T}_e + \hat{V}_{n-e} + \hat{V}_{e-e} \tag{2.7}$$

The nucleus coordinates now enter as parameters. That is, equation 2.1 is solved for a certain set of R_A.

2.4 Density Functional Theory

The DFT method was first introduced by Hohenberg and Kohn [48]. This is a mathematical theory that uses the electron density $n(r)$ to derive the system propertie's and eventually succeeded in overcoming the challenge of reducing the number of parameters that faces most many-body theories. The principal idea of this method is to find the total energy of a system as a function of charge density $E[n(r)]$. It is considered a successful method for quantum mechanical modelling explaining the interactions of many-body systems such as atoms, molecules, and solids.

2.4.1 The Hohenberg-Kohn theorem

Density Functional Theory is based upon two fundamental theorems introduced by Hohenberg and Kohn (H-K) [48]. The first Hohenberg-Kohn theorem assumes that ground state properties can be inferred from the charge density $n(r)$. This further means that a given charge density of the system can correspond to only one electron potential. The ground state energy is thus a functional of $n(r)$, i.e. we may write $E[n(r)]$ equations can be expressed as in equation 2.8:

$$E[n(r)] = F[n(r)] + \int n(r)V_{ext}(r)d^3r \tag{2.8}$$

Here $F[n(r)]$, which is a universal function that represents the kinetic energy and electron-electron interactions in the system. Therefore, the H-K calculate ground state depending on $n(r)$. The second H-K theorem [49] states that the correct density $n(r)$ can be inserted into $E[n]$, is the one that produces the minimum energy.

2.4.2 The Kohn-Sham Equations

In order to applied density functional theory approach for computational applications, Kohn-Sham (K-S) [49] suggested approach in which the system is replaces the real electron state with function electron, which is generated the same charge density. The main idea behind this approach is to calculate the non-interacting system of electrons that have the same density $n(r)$ as the real system. The total energy of a system can be expressed as a function of the charge density as in equation:

$$E[n] = T[n] + V_{ext}[n] + V_{e-e}[n] \tag{2.9}$$

Where $T[n]$ is the kinetic energy, while $V_{e-e}[n]$ of a fictitious non-interacting system of electrons which has the same density $n(r)$ as the real system. $V_{ext}(r)$ is an external potential representing the interacting system. There is obstacles to straightforward application of this formula one of them is that exchange and correlation energy is not known exactly. One of the effective approximations that can be used within DFT is the local density approximation (LDA).

2.4.3 The exchange and correlation functional in DFT

The local density approximation is the most widely used approximation for determining the exchange-correlation energy function in order to produce accurate ground state energy and charge density. Its local density $n(r)$ means that the electron exchange-correlation energy density of a homogeneous electron gas $\epsilon_{xc}(n)$ is used locally as a function of the electron density at the given point:

$$E_{xc}[n] = \int n(r)\epsilon_{xc}(n)dr \tag{2.10}$$

This method is very useful in determining the exchange-correlation energy function, as it is the mostly used for modelling solids. Despite providing rational definitions for the non-homogenous systems, the DFT technique in LDA results in an underestimation of the lattice constant and the band gap values. Table 2.1 lists the computed lattice constants and band gaps for the 3C-SiC, as a cubic structure of SiC polytypes. Based on the current results, the calculated values for the lattice constants show a high level of agreement with the theoretical values reported in the literature [5], which is reflecting the well-documented underestimate arising from the underpinning methodology [50, 35] (see Table 2.1).

On the other hand the calculated band gap is underestimated by around 1.0 eV, which is well known in the literature, for the LDA calculations, which is consistent with the data reported in [19]. Ground state energy can be accurately predicted without the optical band gap being correct. This means that the ground state properties, such as thee lattice constant, bond lengths, migration barriers, formation energies and electrical levels (which, as explained in chapter 3, are found in ground state total energies), can be accurately predicted by DFT, even if the band gap is poor.

Parameter	Present work	Theory [5]	Experiment [6]
a_0 (Å)	4.33	4.35	4.36
E_g(eV)	1.30	1.20	2.36

Table 2.1: Energy band gap E_g and lattice parameters a_0 for 3C-SiC calculations by using LDA. This result is compared with theoretical and experimental values [5, 6] and shown here for the comparison.

2.5 Chapter Summary

This chapter briefly provided an overview of the computational quantum method density functional theory (DFT), with the mathematical principles approximations. The technical methods and the relevant theories and aspects of the calculation parameters have been discussed. The next chapter will present additional methods and the implementation of the DFT theory in the AIMpro software along with the calculations for the defect structures and the experimentally observable properties.

Chapter 3

Modelling of physical quantities

3.1 Introduction

In chapter 2, the fundamental theory of electron density energetics was presented with a focus on density functional theory. In this chapter, an efficient computational implementation of DFT using the quantum mechanical code AIMpro [46] is presented. This code is used to calculate the electronic and structural properties of a multi-electron interacting system. The AIMpro software takes atomic-level information as inputs from the user. These inputs are fundamental to the problem or system under consideration, and the solution is sensitive to these parameters. These inputs are summarised as follows:

1. Atomic geometric configuration: position, atom types.
2. Basis functions to be used for the wave function and charge density
3. Supercell size: determines the structure size to be studied
4. Sampling zone: sampling grid size for integration approximations

The inputs are either (a) determined based on the system or (b) optimised a priori with a simple system before moving on to a complex system understanding or (c) as well some inputs are based on understanding from the literature. On the basis of these inputs, AIMpro solves the Kohn-Sham equations [49] through a self-consistency cycle algorithm which is an iterative procedure to find the minimum energy of the system. In this chapter, the simplification of DFT theory implementation is presented with emphasis on the basis of the choice of the input parameters listed above. In the latter half of the chapter, the calculations of fundamental material properties are presented with the help of the code.

3.1.1 Self-consistency cycle

The self-consistency cycle (SC) is an iterative procedure for solving Kohn-Sham (KS) equations (section 2.4.2) by determining a residual potential. In a generic sense, in this method the charge is redistributed around the system iteratively until the minimum total energy is achieved, which is then taken as the solution to the KS equations. The solution procedure starts with the initial charge density $n(r)$, which is guessed as either a neutral atom density or from the output of a previously optimised structure and used to generate a potential. The initial estimate of the charge density is further used to solve the KS equations to obtain a new output charge density, $n(r)$. The difference between the initial and the new output charge density is calculated, and if the difference (residual) is within a certain threshold, the new density is taken as the solution. Otherwise, the procedure is re-iterated until a converged charge density solution is found. The procedure is illustrated in the schematic in figure 3.1.

3.1.2 Pseudopotential approximation

Interactions between core electrons and the nucleus are complicated and computationally challenging to solve. For example, the electronic configuration of a carbon atom is $1s^2 2s^2 2p^2$. The $1s^2$ refers to the core electron (C_e) of a carbon atom, which does not chemically bond because of its extremely localised position around the nucleus. Only the valence electrons (V_e) $2s$ and $2p$ contribute to bonding. One may remove the core electrons from the explicit quantum-mechanical simulation by using a pseudo-potential approximation that defines an effective net potential term to reduce the computational expense. This approximation is illustrated in figure 3.2, which shows both the real potential and a pseudo-potential.

The pseudo-potential of Hartwigsen, Goedecker and Hutter (HGH) is used throughout this thesis for all calculations are easily available from the literature [51]. In this study, atoms are modelled using norm-conserving separable pseudopotentials, with $2s^2 2p^2$ and $3s^2 3p^2$ valence sets for C and Si, respectively, as per the standard AIMpro guidelines.

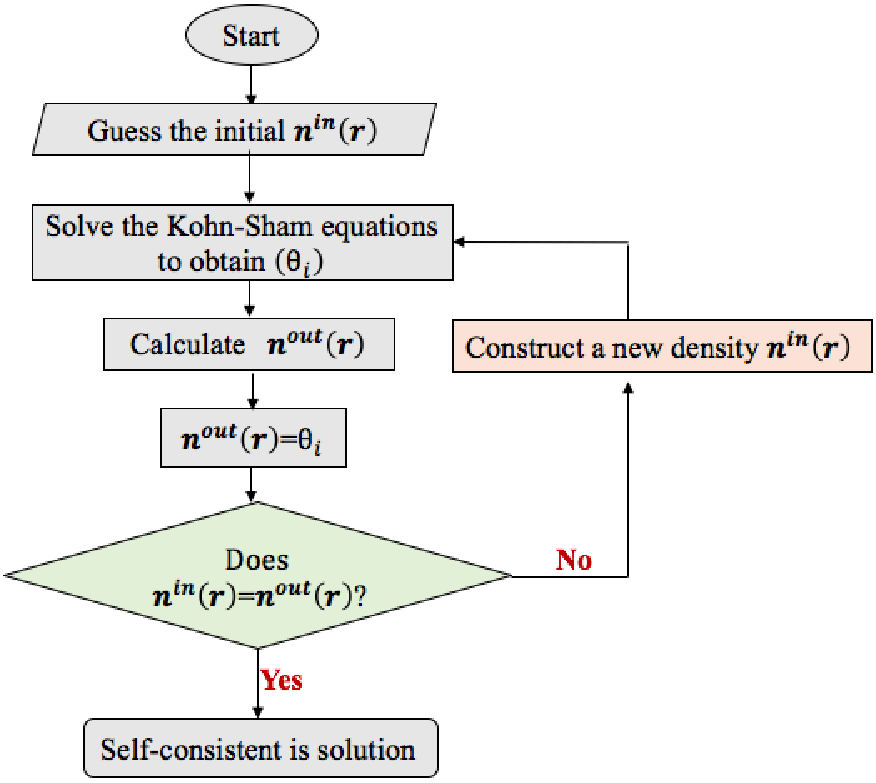
Start
Guess the initial $n^{in}(r)$
Solve the Kohn-Sham equations to obtain (θ_i)
Calculate $n^{out}(r)$
Construct a new density $n^{in}(r)$
$n^{out}(r)=\theta_i$
Does $n^{in}(r)=n^{out}(r)$?
No
Yes
Self-consistent is solution

Figure 3.1: The schematic flowchart of the self-consistent for density functional-based calculations.

3.1.3 Basis sets functions

The basis set method expresses a complicated mathematical function using a sum of suitable simpler functions. In the AIMpro package, this approach is leveraged by representing the charge densities and the electron states by linear combinations of Gaussian functions to form the orbitals only a small number of functions per atom is required, significantly reducing the time required for calculations. The Cartesian Gaussian orbitals assign a group of basis functions to each atom within a molecule and are able to approximate and expand the wave function mathematically in order to provide accurate results.

The Gaussian basis functions, θ_i, which are centred at an atomic site, R_i, are as shown in equation 3.1,

$$\theta_i(r) = (x - R_{i,x})^{a_1}(y - R_{i,y})^{a_2}(z - R_{i,z})^{a_3}e^{-\alpha(r-R_i)^2} \tag{3.1}$$

where a_1, a_2 and a_3 are integers and $\sum_i a_i = 0, 1, 2, \ldots$ There are various types of orbitals that can be constructed by selecting different values of a_i, which correspond to particular

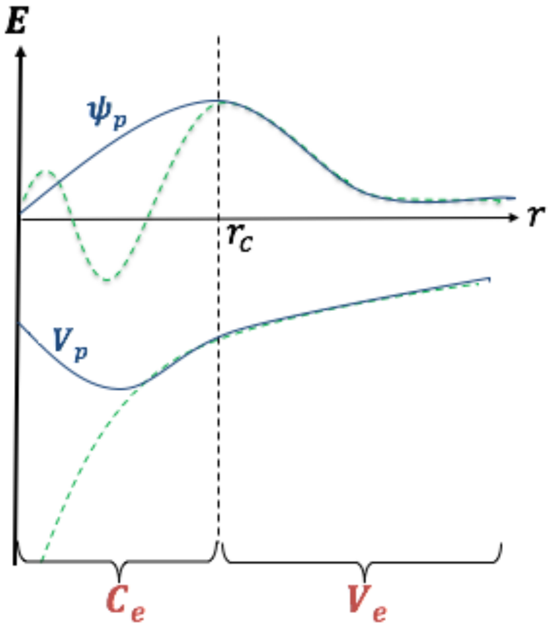

Figure 3.2: Schematic illustration of electron wave-function and potential (dashed green line), and the pseudo-potential and resulting wave-function (solid blue line). Note that the cut-off radius r_c indicates the defined region at which point the systems must match. C_e and V_e refer to the core and valance electrons respectively.

atomic orbitals (s, p and d), while α is a constant for each function. In this thesis, the Cartesian Gaussian orbital basis sets are extensively used to increase the breadth of the study.

Several test calculation basis sets that are provided by the AIMpro package are used to the optimised material for Si and C. The total energies were computed from the electron charge density using the different basis set to select the most promising basis set for both elements C and Si. The basis sets used to represent Si and C in 3C-SiC are optimised to obtain the minimum total energy are (SiC-*ddpp*), which contains of 28 functions per atom. The data in table 3.1 shows the influence of structural properties, which include the total energy, bulk modulus (B_0), and lattice constant (a_0) of SiC for different basis sets. The numbers of the labelled basis sets indicate the exponent and number of functions per atom for silicon and carbon. For example, the labelled basis function (*ddpp*), which is used to represent Si and C in the SiC polytypes, comprises four letters indicating four different exponents.

As clearly shown in table 3.1, the variation in the structural parameters with basis is relatively small such as basis like *pdpp* or *ddpp* and *dppp* are found to be sufficient. Although the same basis sets are able to describe the pure SiC polytype, with *ddpp* a higher accuracy is obtained with much higher computational speed as compared to the other basis sets in table 3.1.

Consequently, this basis set consists of 28 functions per atom, giving the best lattice parameters for the 3C-SiC system when compared with the values of 4.33Å and 4.36 Å obtained by another theoretical-experimental study [5, 6].

Furthermore, to establish the accuracy of the Gaussian basis set used in this thesis, the lattice constant of the hexagonal lattice (4H-SiC) was calculated using the same basis set for both Si and C. Comparison of the two lattice constants a_0 and c with other simulations and experiments shows excellent agreement. Based on the current results, the calculated values for the lattice constants a_0=3.06 Å and c=10.04 Å compared with the values of a_0=3.07 Å and c=10.04 Å obtained by another theoretical study [5]. Moreover this result also shows a best agreement with experimental lattice constants values reported in the literature [5] (a_0=3.07 Å and c=10.05 Å, more details in 3.2.2).

In summary, these results and calculations provide a good foundation for the use of the basis set SiC-*ddpp* for both Si and C atoms for all subsequent calculations with both polytypes throughout the rest of this thesis.

3.1.4 Supercell approach

The computational costs of modelling defects, interfaces and surfaces can be mitigated by choosing a model system, i.e. a supercell, which is representative of an infinite and periodic set of cells. To investigate defect modelling in bulk SiC and surfaces using the slab method (as will be discussed later in chapter 5, it is necessary to ensure that the supercell is large enough to contain all the local relaxation around a defect [52]. When defects are introduced to the unit cell, they are arranged periodically, which means that they are repeated throughout the three dimensions.

Therefore, one should consider how to avoid the localised charge distribution with its neutralising total energy around each defect. The slab-model approach is used to model

Basis	Si	C	No. functions per atom	a_0 (Å)
1	*pdpp*	*pdpp*	22	4.238
2	*dddppp*	*pppp*	29	4.318
3	*ddpp*	*ddpp*	28	4.332
4	*pppp*	*pdpp*	19	4.362
5	*dddd*	*ddpp*	34	4.314
6	*ddpp*	*dppp*	25	4.323

Table 3.1: Calculated lattice constant and time as a function of the number of Gaussians by using to describe 3C-SiC basis sets for a primitive SiC cell.

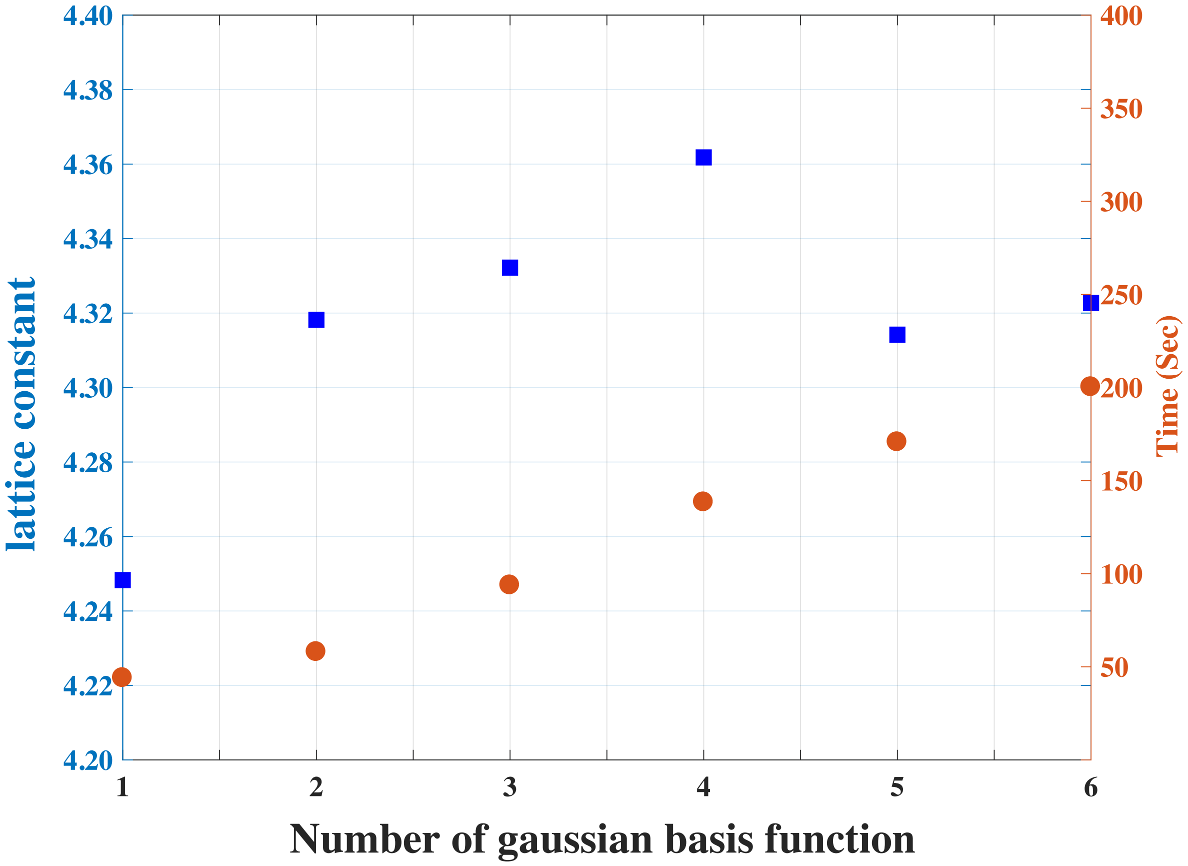

Table 3.2: Calculated lattice constant by using different basis sets for a primitive SiC cell. Numbers refer to the basis sets listed in table 3.1.

the interface. The slab in the supercell is infinite in the xy plane, while finite in the z-direction normal to the interface. This uses a basic repeated unit cell (*slab*) with 2D symmetry and periodic boundary conditions [53].

There are two important considerations when modelling the structure of the 4H-SiC/SiO$_2$ interface: (a) the crystal slab should be thick enough to study any defects present beyond the deep layer; and (b) the vacuum region between the two slabs should be wide enough to isolate the two slabs. Chapter 5 discusses these features in detail. The various different structures of 4H-SiC determine the behaviour of carbon vacancies (V_C) in bulk 4H-SiC. Subsequent calculations were performed using two different sizes of supercell for 4H-SiC (as shown in Figure 3.3) and carbon vacancies were analysed in bulk 4H-SiC (see chapter 6). In contrast, the investigation of diffusion V_C in bulk 4H-SiC did not need more than 71 atoms to describe this calculation without defect–defect interactions [52], as presented in chapter 4.

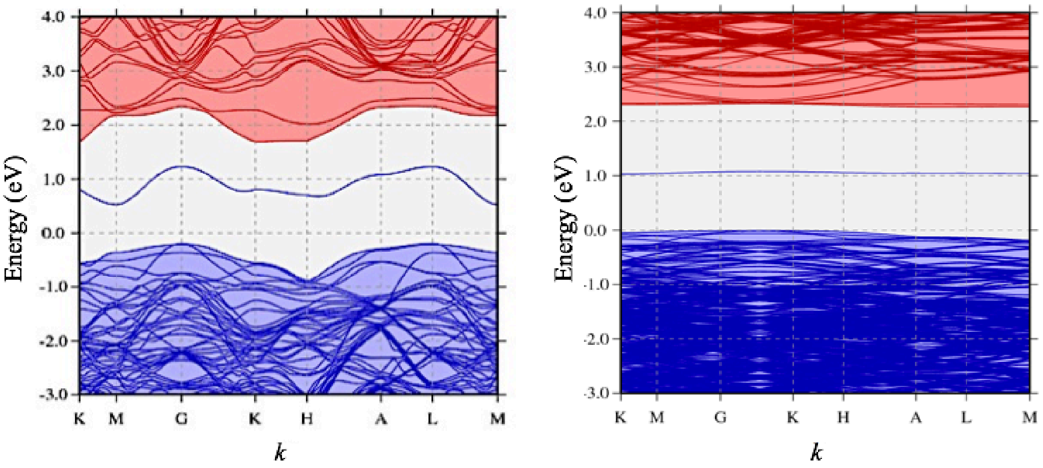

Figure 3.3: Band structure of the V_C in 4H-SiC in the neutral charge state. The deep defect level is shown as the blue line and its dispersion is presented for the 71, and 575 atom supercells. The blue and red lines represent occupied and empty bands, respectively, with the underlying shaded areas showing the valence and conduction bands.

3.1.5 Sampling of the Brillouin Zone

Total energy calculations in periodic systems require an integration over a primitive unit cell of the reciprocal lattice, often referred to as the Brillouin zone (BZ) [54]. These calculations are essential to calculate the electronic and structural properties of the system using a supercell with specific boundary conditions. The Brillouin zone sample contains a set of finite points, which are called k-points.

Monkhorst and Pack proposed a uniformly spaced k-point mesh over the BZ, giving the advantage that the mesh density can be used as a parameter to adjust the trade-off between accuracy and computational cost in integrating over the Brillouin zone. The sampling scheme is therefore represented by MP-n^3 for an $[n \times n \times n]$ grid.

It does, however, ensure that the chosen lattice vectors are the same length-scale magnitude, creating a cubic structure. Therefore, in this thesis, the Monkhorst-Pack (MP) method is used for the BZ sampling. The energies calculated for a range of sampling schemes, including MP-2^3, MP-4^3, MP-6^3 and MP-8^3 are shown in figure 3.4. The influence of BZ sampling on the calculated physical properties of bulk SiC polytypes was determined, and the data shown in the figure relate to a two-atom 3C-SiC structure. The results show that the energy per atom is independent of the number of k-points selected for sampling. Further, the values of the lattice constant exhibit similar behaviour to that of the total energy. The data show that the calculated energy difference $6 \times 6 \times 6$ is $4 \times 4 \times 4$ is equal to 3×10^-5 eV, which is significantly more than $1\,meV$. Therefore, throughout the rest of this thesis, MP sampling of $[4 \times 4 \times 4]$ is fixed to for any subsequent 3C-SiC structure studies.

The sampling study is further extended to hexagonal polytypes from the cubic structures, as demonstrated previously. The 4H polytype and the k-point values of $[6 \times 6 \times 2]$ were tested, and the required grid size was established by a convergence test. The limit of the grid size was tested to an extent that an extra k-point within the BZ led to an unnecessary computational cost, with the calculated value showing a very minor deviation. The energy values and the difference in the lattice constant value remained almost unchanged from the $[2 \times 2 \times 2]$ grid, which will now be used in the remainder of this study to model hexagonal polytypes.

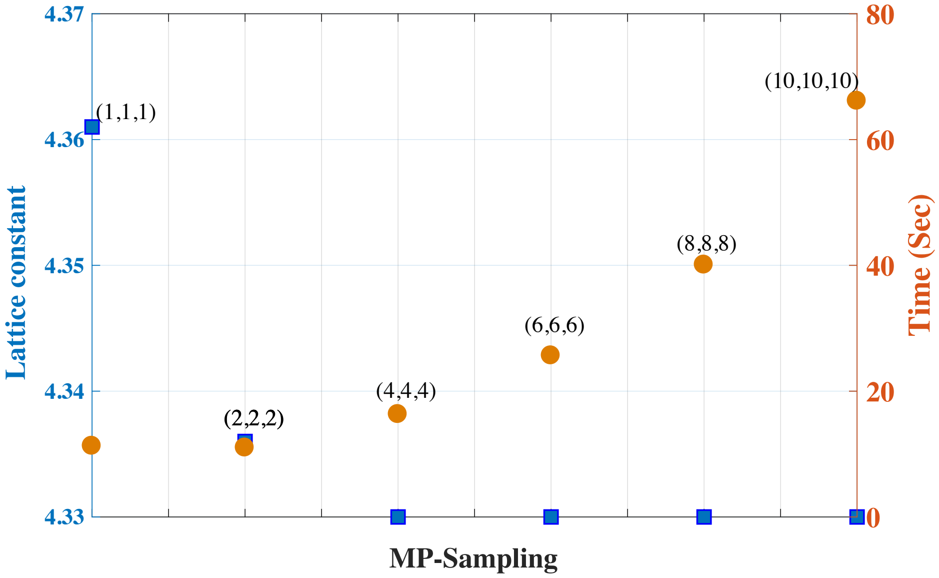

Figure 3.4: Calculated lattice constant and the computation time with different BZ sampling. These calculation are achieved to show how the Brillouin zone sampling affect the 3C-SiC modelling accuracy.

3.2 Derived quantities

In the previous sections, the parameters relating to total energy calculations on the basis of DFT were identified and studied. However, the first-principles simulations are much more meaningful when their outputs are compared against experimental observables. In this section, several of the experimentally measurable observables, such as the formation energy of carbon vacancy defects, are explained in detail. Furthermore, the emphasis here is on how these experimental observable quantities can be calculated or reconstructed from the first-principles DFT simulations, which aim to model the structure at a more fundamental microscopic "electron" length-scale.

In this section, the following important quantities (obtained from DFT) are discussed:

1. Lattice constant and bulk modulus

2. Formation energy and electrical levels

3. The diffusion barrier.

3.2.1 Structural optimisation

AIMpro simulations require a knowledge of constituent atoms, and the underlying physics of the energetics is fully governed by the quantum-mechanical DFT. The code determines the structural and electronic properties of a range of materials such as semiconductors, metals and insulators. The foremost computational task is to find the stable equilibrium structure of the system. This requires the determination of the state of the system with minimum energy. This process is called (relaxation) or (optimisation) and uses the forces on each atom. In AIMpro, the conjugate gradient method is performed to identify a self-consistent charge density (section 3.1.1). The structures are optimised until the change in energy between iterations is less than 10^{-5} Ha, while the forces are below 10^{-3} atomic units. It is to be noted that this method could calculate an optimised structure within a local energy minimum rather than the global energy minimum of the system. In order to reach a level of certainty, several tests can be performed to optimise until finding the lowest energy state. This is presumed to be the best estimate of the ground-state structure.

3.2.2 Lattice constant and bulk modulus

To evaluate the lattice parameters for the SiC structure, the values determined from the initial calculations are considered as a function of unit cell volume. AIMpro calculated energies were fitted to determine the bulk modulus B_0 and equilibrium volume by means of the Birch-Murnaghan equation of state for the total energy [55, 56], as shown in equation (3.2). The purpose of the procedure is to obtain the relationship between total energy and unit cell volume in bulk 3C-SiC.

$$E(V) = E_0 + \frac{B_0 V}{B_0'}\left(\frac{(V_0/V)^{B_0'}}{B_0'-1}+1\right)\frac{B_0}{B_0'-1} \tag{3.2}$$

where E_0 refers to equilibrium energy and equilibrium volume V_0, B_0 is the bulk modulus and $\acute{B_0}$ presents the first derivative of the bulk modulus B with respect the pressure, are defined as:

$$B_0' = -V\left(\frac{\partial P}{\partial V}\right)_{P=0} \tag{3.3}$$

Density functional theory calculations have been used to identify the equilibrium atomic structure of SiC, which is plotted as a function of energy versus unit cell volume, rather than the lattice constant $a_0 = V^{1/3}$. Thus, these can be fitted to determine values for the extracted lattice constant and bulk modulus, which can then be compared to suitable experimental values [57]. For example, the equilibrium lattice constant and bulk modulus of 3C-SiC calculated using the LDA approximation for two 3C-SiC atoms with a basis set (SiC-*ddpp*) for both Si and C atoms (as described previously in section 3.1.3) extends by 4.33 Å. This value agrees with the experimental value [5]. The bulk modulus is 228.7 GPa, which is just slightly higher than the experimental value of 224.0 GPa [57]. These results thus sufficiently converged to the total energy and optimised lattice parameter, and they agree well with both theoretical and experimental values in the literature.

In addition, the lattice constant was determined for the 4H polytype, the hexagonal structure, using an eight-atom supercell with the basis set *ddpp*, as shown by the data summarised in table 3.3. When compared with other simulations and experiments, the values show excellent agreement. The calculated values for the lattice constants a_0 showed a high level of agreement with the theoretical values reported in the literature. The data show that the lattice constants for both 3C- and 4H-SiC are similar to those reported in another theoretical study.

Parameter	This study	Theory [5]	Theory [58]	Experiment [57]
3C-SiC				
a_0	4.33	4.33	4.45	4.36
4H-SiC				
a_0	3.06	3.06	3.07	3.07
c	10.04	10.01	10.04	10.05

Table 3.3: Structure properties of 3C- and 4H-SiC was calculated by using DFT in comparison with other studies. All energies in eV.

3.2.3 Electronic structure

The electrical properties of a solid material can be expressed by description of all allowed electronic energy levels put together in the form of electronic band structures. The band structure is effectively a plot of the energy of an electron as a function of its wave vector.

The energy bands of a material can be described by three key quantities: (a) the valence band E_V, which contains the electrons; (b) the conduction bands (E_C); and (c) the empty energy between E_C and E_V, known as the band gap. Figure 3.5 describes the band structure of 3C-SiC as simulated via AIMpro and shows the minima of the conduction bands and the maximum of the valence band, The band gap was measured from the highest point on the valence band (Γ-point), as in previous studies [58]. The LDA calculations of this structure give a band gap value of 1.30 eV, which is very similar to the theoretical value of the *Ab Initio* LDA calculations as shown in the literature [5], and the experimental values differ by 1 Å. As mentioned in section 3.1.3, the error in the predicted band gap for wide band gap materials was typically 1.0 eV, which is consistent with the reported data [59]. Therefore, these results reflect the accuracy of the *Ab Initio* LDA calculations, which were obtained in terms of bulk SiC.

SiC polytapes	This work	Theory [5]	Theory [58]	Experiment [57]
3C-SiC	1.30	1.20	1.33	2.36
4H-SiC	2.20	2.20	2.23	3.23

Table 3.4: Comparison of band gap of 3C-SiC and 4H-SiC as well as other theoretical and experimental results. All energies in eV.

Furthermore, the studies were repeated for the 4H-SiC structure with a calculated band gap of 2.5 Å and lattice constants $a_0 = 3.06$ Å and $c = 10.04$ Å. The indirect band gap of 4H-SiC was calculated from the band structures and found to be 2.2 Å. This value is quite similar to that reported previously for density functional theory calculations but shows the expected reduction in comparison to the experimental values [57], as shown in table 3.4. This result is similar to that reported by one study [5], but slightly lower than that reported by another [58]. This difference arises from the choice of different pseudo-potentials in their calculations.

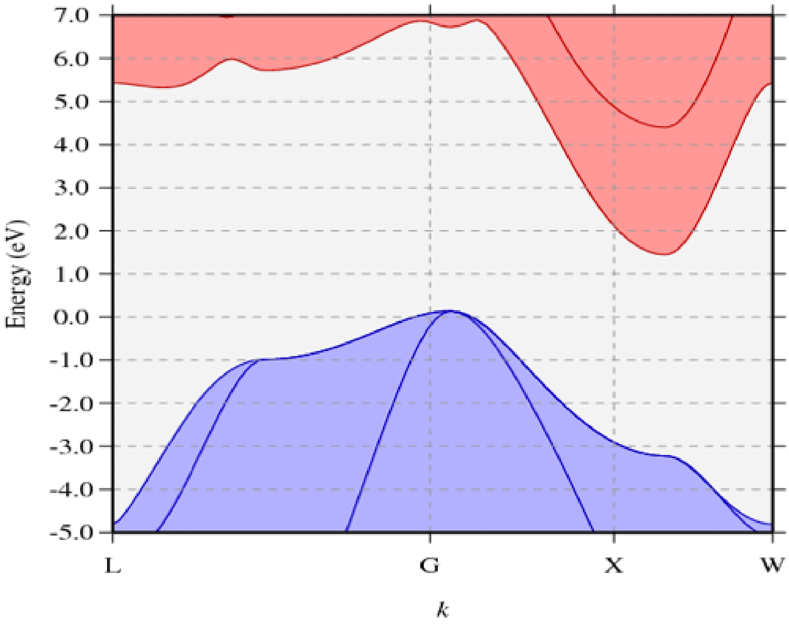

Figure 3.5: Band structures of 3C-SiC for using a two atom unit cell, the red and blue levels show condition band E_C and valance band E_V respectively.

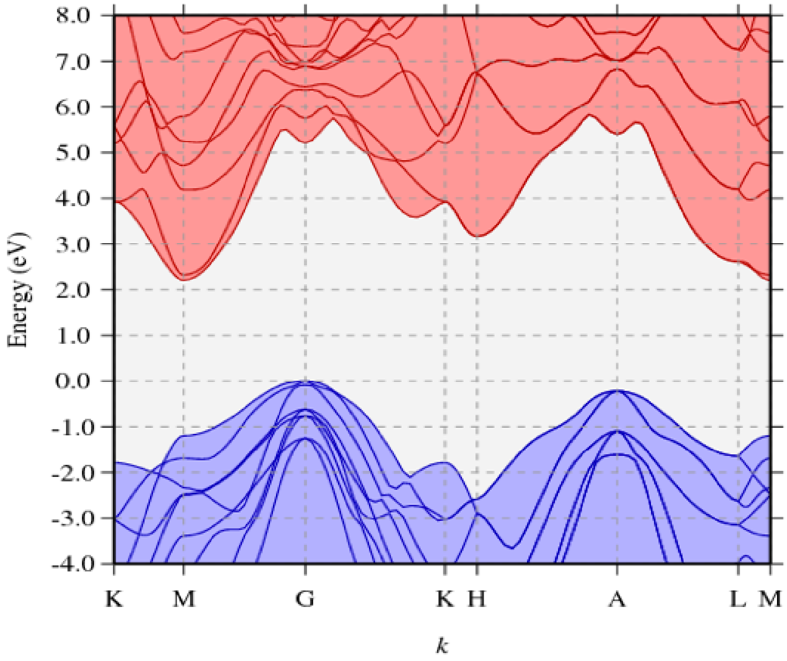

Figure 3.6: Band structure of bulk 4H-SiC, empty and occupied bands are shown in red and blue respectively. The condition band minimum is located at M point, the valence-band maximum is at Γ-point.

3.2.4 Formation energy and electrical levels

The electrical characteristics of the defect that represent the charge state transition can be calculated by the formation energy equation (3.5), which is fundamentally defined as the difference between the energy of the atom configurations and the sum of the energies of the atoms in their reference or elemental state. These are useful for understanding the behaviour of different defects in a system. The formation energy $\mathrm{E}_x^f(0)$ of a particle system x in natural charge states can be expressed as follows:

$$E_x^f(0) = E_x(q) - \sum \mu_i + q\mu_e \tag{3.4}$$

Equation 3.4 can be written as equation 3.5.

$$E_x^f(q) = E_x(q) - \sum n_i\mu_i + qE_F + \eta_x(q) \tag{3.5}$$

where q refers to the charge state of the system, μ_i and n_i denote the chemical potential and number respectively of the atom species i. The energy of the valence band maximum E_{VBM} is often chosen as a reference energy for E_F. It can be expressed by $(E_{VBM} + \mu_e)$. The extra term in equation 3.5, η_x(q), refers to a correction caused by the approximate treatment of a charged defect in a finite-sized unit cell.

Calculations of electrical levels as a function of the electron chemical potential are possible when two charge states are equal, as shown schematically in figure 3.7. The formation energy of the charged the electron defect follows the same trend as electron chemical potential. The system changes its charge state at the point where (q and $q+$ N_e) have the same energy; μ_e stands for number of added or removed electrons. Therefore, the single donor level corresponds to μ_e, where $E_x^f(0) = E_x(+1)$, and it is written as (0/+). The μ_e for the equation $\mathrm{E}_x^f(0) = E_x(-1)$ characterises the single acceptor level, which is inscribed as $(-/0)$. The left and right symbols on either side of the slash therefore represent the defect electron charge state.

As an example of this calculation, the equilibrium concentration and ionisation levels of V_C of 4H-SiC are calculated here. The chemical potentials of components μ_C and μ_{Si} are related by $\mathrm{E}_{SiC} = \mu_C + \mu_{Si}$ where E_{SiC} is the energy per bulk formula unit in SiC. The range of possible values for μ_C and μ_{Si} is related to the requirement for 4H-SiC to be stable relative to decomposition into its elemental constituents, so that the silicon-rich limit is taken from silicon-metal, and for carbon-rich. The formation for V_C in 4H-SiC in a neutral charge state is calculated to be 3.49 eV, which agree with pervious work (3.61 eV) [58].

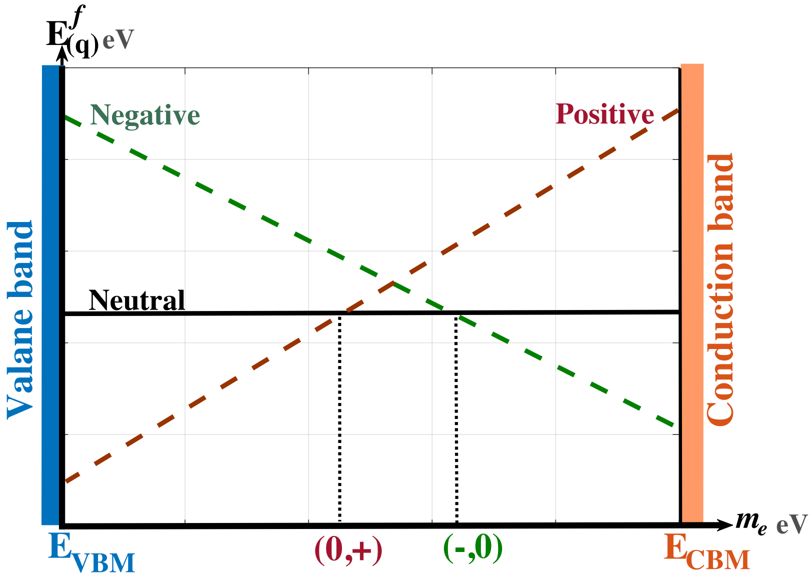

Figure 3.7: Schematic diagram illustrating the formation energy $E^f_x(q)$, to obtain donor and accepter levels for the system x, as a function of the electron chemical potential μ_e. The dashed green and red lines obtain donor and accepter level respectively. E_{CBM} and E_{VBM} are represented to conduction and valence band respectively.

Defects introduce frequently electrical energy levels in the forbidden energy gap such as carbon vacancy defect in SiC [58]. These energy levels are consequences of the symmetry breakage of the crystal structure. The electrons may be captured by those at various rates which depending on the potential produced due to the crystal defect. Donor levels that are located quite close to the conduction bands (CB) are referred to as shallow donors, whereas the acceptor levels located close to the valance band (VB) are called shallow acceptors. Deep acceptors and the donor levels are located far from the VB and CB, respectively, and as shown in figure 3.8. The band gap width and defect states are primarily responsible for the conductive properties of the materials. The majority of electrically active defects in SiC have levels located deep within the band-gap, and these act as the carrier traps and degrade the carrier transport properties as discussed in chapter 6.

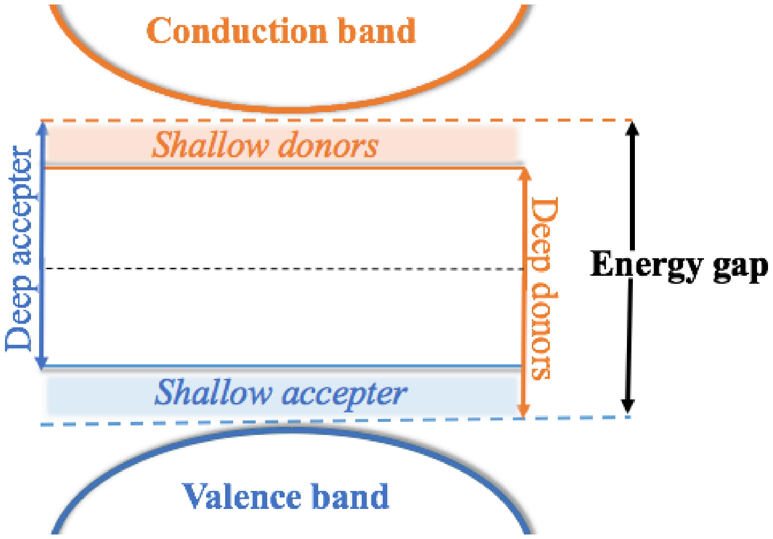

Figure 3.8: The schematic diagram shows shallow and deep levels of material. The orange and blue curves represent the conduction and valence bands, respectively, and the separated by the energy gap. The orange and blue shades refer to donors and acceptor levels, respectively.

3.2.5 Diffusion barrier

The dynamics of defect behaviour is a key to improving or designing the channel mobility of devices. In order to find minimum energy pathways between different orientations of defects or just the migration of a defect, the nudged elastic band (NEB) technique can be used within the AIMpro package [60, 61].

In this method, the migration mechanisms of the defects in SiC (in order to obtain an energy barrier (E_{ba}) can respond to an accuracy of 10^{-4} au)

can be calculated via a curve containing a number of “images” along a path between two equilibrium structures. As a first step, the minimum energy of the initial (S_1) and final structure (S_2) is found. The structure with the highest energy along the reaction path is called the saddle point. The minimum energy path between each structure is found by linear interpolation of a number of “images” along the path, and the optimisation of each of the images, which are in turn connected via spring forces to ensure equal spacing along the reaction path. The procedures for NEB calculations can be described as shown in figure 3.9.In the schematic flowchart in figure 3.9, three diffusion processes can occur in principle:

Three diffusion processes can occur in principle 3.9:

(a) Symmetrical diffusion: the diffusion energy rate in the forward reaction is equivalent with that of the backward reaction, and the energy is equal between states S_1 and S_2, as occurs in path-1

(b) Forward transition: excitation applied at an initial state S_1 overcomes the energy barrier E_i and reaches state S_2 (E_i ¿ E_f). This can often lead to rapid symmetrical reactions from the higher energy structure to the lower one 3.9.

(c) Reverse or backward transition: This transition occurs when E_i is greater than E_f: the atom resides at state S_1 and moves to state S_2. However, this reaction is not favourable in comparison to the forward transition 3.9.

In the present work, the activation energy and reaction pathways of carbon vacancy defect in bulk 4H-SiC, the barrier is optimised by using seven images and the image-forces are less than 0.01 atomic units. This will be presented in more depth in chapter 4.

3.3 Chapter Summary

In this chapter, a detailed implementation of DFT within the AIMpro package (self-consistency cycle calculations) was presented, along with the rationale for the choices of the key input parameters are:

1. The Pseudopotential approach: to help in speeding up the DFT calculations by removing the core electrons from a calculation.

2. Atomic geometric configuration: position, atom types, relaxation.

3. Basis function: to expand the Kohn-Sham electron orbitals for the wave function and charge density.

4. Supercell size: to determine the structure size to be studied.

5. Sampling zone: the sampling grid size for integration approximations.

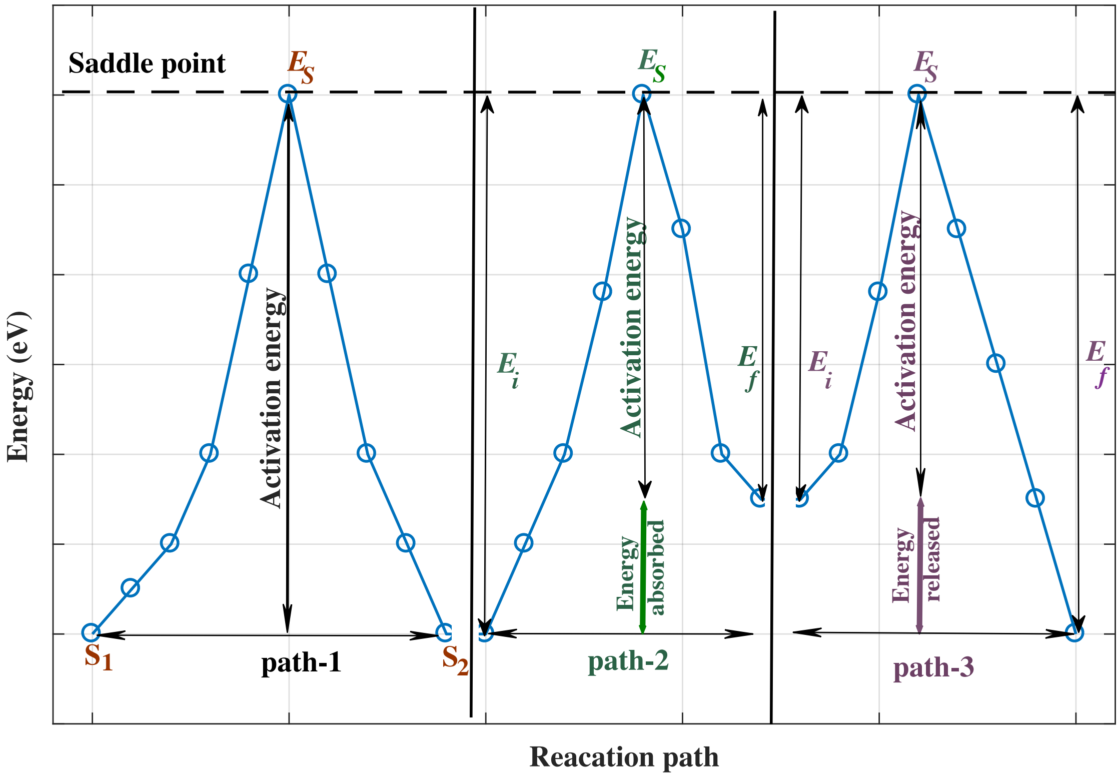
Saddle point
E_S
E_S
E_S
Energy (eV)
Activation energy
Activation energy
Activation energy
E_i
E_f
E_i
E_f
Energy absorbed
Energy released
S_1
path-1
S_2
path-2
path-3
Reacation path

Figure 3.9: Simple scheme representing a NEB calculation. There are three reaction pathways between two relaxed structures S_1 (initial state) and S_2 (final state) and the highest point between them is a saddle point (E_s). Whereas (E_i) represent forward energy, while (E_f) appear the forward reverse activation energy barriers.

The chapter also presented the first-principle calculations of the derived quantities such as the lattice constant, the electronic structure and the diffusion barrier. The input parameters listed will be used in the rest of the thesis to calculate the key experimental variables and compare them against relevant experiments.

Part II

Applications

Chapter 4

Intrinsic defect in Bulk 4H-SiC

4.1 Introduction

A detailed knowledge of point defects is a prerequisite to understanding and subsequently controlling the electronic properties of SiC-based semiconductors [29]. Vacancies and interstitial defects are the most fundamental defects and also the primary defects that are produced during the ion irradiation and annealing processes [29] (see section 1.2.3). In the next two sections, an overview of carbon vacancy and interstitial defects is presented.

4.1.1 Carbon vacancies in crystalline 4H-SiC

For an overview of carbon vacancy defects in 4H-SiC, readers are encouraged to refer to the literature [58, 30, 29, 19, 62]. The 4H-SiC structure has a strong site dependence for carbon vacancies, and this results in a different structure for the *k* and *h* [29, 62, 63] (see section 1.2.1). A variety of carbon vacancies arise from different inequivalent sites (*h*-site and *k*-sites) in the 4H-SiC lattice. The influence of inequivalent sites is not negligible and needs to be understood to control impurities and defects [29, 64].

One theoretical calculation, predicts that there should be a striking difference in the carbon vacancy properties as compared between the *k* and *h* sites for 4H-SiC, due to different Jahn-Teller distortion behaviours [62]. In this thesis, emphasis is laid specifically on the geometrical structure of V_{C} and the mechanisms of vacancy migration. The computational studies by [62] are based on DFT calculations within the local spin-density approximation (LSDA), and emphasis was mostly on investigating the electronic and atomic structures of the defects in 4H-SiC for possible charged states. It has been concluded that the influence of inequivalent sites is qualitatively similar for geometric structures but different for the charged state [62].

However, the influence of inequivalent sites was found to be negligible. Geometric structure data by [58] suggest that the relaxations in the structure due to a carbon vacancy lead to shortening of the bond lengths for the four nearest-neighbour (NN) Si atoms (2.7 Å as compared to 3.05 Å for a pure Si–Si bond). This is referred to as the pairing mode, where Si atoms form new covalent bonds, and has been corroborated by previous literature studies [30, 62]. Another theoretical study by Umeda *et al.* [20], which is supported by EPR studies, concluded that the shorter length is due to fact that the k site shows a Jahn-Teller distortion of V_{C}.

Several theoretical works have studied the energy barriers for the migration mechanism of V_{C} transport through the SiC layer [30, 65, 66, 33]. Knowledge of migration processes is crucial to understanding the kinetic properties of defects. Bockstedte *et al.* [30] presented a comprehensive picture of the formation and migration energies and concluded that these energies are very similar. However, the data showed that the knowledge of defect energetics still lacks completeness. The results for cubic SiC (3C-SiC) and hexagonal polytypes (4H-SiC) were discussed but did not address inter-site differences (hk or kh). Also, Gao *et. al.* studied the migration of point defects in 3C-SiC using the molecular dynamics (MD) and nudged-elastic band methods. It was suggested that the carbon vacancies jump to one of their equivalent sites through a direct migration mechanism and the activation energy for V_{C} migration was reported to be around 4.10 eV in the neutral charge state [33]. Moreover, more recently, migration of carbon vacancies in 4H-SiC and their energy barriers were studied in great detail by [65, 66]. It was shown that the migration energy varies significantly with the charge state. The migration energy for a carbon vacancy is raised by almost 2 eV for the neutral state as compared to the V_{C}^{+2} charged state.

A variety of experimental techniques has been used to describe the defects within the bulk 4H-SiC bulk, surface and interface regimes in SiC-based samples (not necessarily devices). The most prominent trapping centres in as-grown 4H-SiC are the $Z_{1/2}$ and $EH_{6/7}$ centres [19, 3, 67, 68, 69]. These have been reviewed in detail in the section 1.2.3.

On the basis of comparative EPR and DLTS studies, researchers [29] suggest that the peak could also be attributed to the V_{C} defects [3]. Experimental data by [10] indicate that the defects are linked to V_{C} concentrations which are produced at the $\mathrm{SiO_2}$/4H-SiC interface during the formation of $\mathrm{SiO_2}$. This leads to a reduction of the $Z_{1/2}$ and $EH_{6/7}$ centres. Theoretical calculations using DFT found that the electrical level properties of V_{C} defects are very similar to those of $Z_{1/2}$ and $EH_{6/7}$ DLTS centres [19]. A study by [67] has unambiguously shown that the $EH_{6/7}$ level can act as a double donor, located at 1.5-1.6 eV below E_C [68]. However, it is difficult to be separate because of severe overlapping. The DLTS peak is rather broad and consists of two closely overlapping levels, the energy position of $E_C - 1.35$ and $E_C - 1.50$ eV for EH_6 and EH_7 respectively [70, 71]. These overlapping levels are treated together as their occurrence is found to be almost always concurrent. In fact, it is a common knowledge that the EH_7 and $Z_{1/2}$ levels are different charge states of the carbon vacancy, found on the basis of an energy level comparison of V_{C}, $Z_{1/2}$ and EH_7 [67, 20, 17, 72, 73]. Both the EH_6 and the EH_7 exhibit highly enhanced annealing following either carbon implantation [74] or thermal oxidation [27, 17].

4.1.2 Carbon interstitial defects in the crystalline 4H-SiC

Another primary defect related to an intrinsic defect in the bulk 4H-SiC is the carbon interstitial C_i, which has a lowest formation energy comparing of carbon vacancies among carbon-related defects in SiC. A wide range of structure configurations of carbon interstitials in 4H-SiC has been previously been explored [32, 29], but the most stable carbon interstitial forms short bonds with direct carbon neighbours to form the $(\mathrm{C{-}C})_i$ configuration defect [33, 29, 34, 32]. Carbon interstitials defects are responsible for the reduction of $Z_{1/2}$ and $EH_{6/7}$ centres, previously reported and discussed in [74]. Apart from $Z_{1/2}$ and $EH_{6/7}$, additional deep levels are also, generated during the thermal oxidation process of *n*-type 4H-SiC, labelled ON1 and ON2, which lie 0.84 eV and 1.1 eV below the conduction band [3, 10]. It is generally agreed based on the experimental data [3] that the role of these defects in the active regions of SiC devices is a significant challenge (as discussed in chapter 1). The trapping of carbon within the oxide may further result in an increased concentration of carbon within the SiC. Numerous centres of SiC structures have been experimentally observed by using EPR, such as EI3 and EI1 in the 4H-SiC [34] and T5 in 3C-SiC centres [75, 34]. EI1 is observed as the signal dominates in the SiC sample's radiations (annealing around 200 C°), suggesting that the EI1 centre is related to a single defect rather than the complex ones. This is further represented by [29] and is in agreement with the low migration barrier studies.

It has also reported that the high mobility of the C_i defects and their low formation energy means they could act as condensation points for larger interstitial clusters [34]. This can be further extended to an additional pair of the C_i defects into the SiC lattice and form a carbon di-interstitial [29]. This configuration can play a crucial role in forming carbon aggregates and their impact on annealing mechanisms in SiC [2, 34, 29].This defect can be formed by the two C_i relaxing into the nearby hexagonal ring, which is the most stable di-interstitial structures in the 4H-SiC [29].

Furthermore, Knaup *et al.* suggested the possibility of defect structures at the interface (as will be discussed in detail in chapter 6). They proposed the carbon split-interstitial is responsible for the high state density at the interface near the valence band. It was further suggested that the a single C–C bond is electrically active, having pair of p-states closer to the mid-gap of 4H-SiC [76]. It was also further reported that the pair of interstitial carbon atoms is introduced as an occupied state in the 4H-SiC band gap ($E_V + 0.37$ eV)) while no unoccupied state was reported [76]. A detailed discussion of the role of the single and pairs of this defect will be given in this chapter.

4.1.3 Chapter Objectives

From the literature review, it has been recognised that even though a plethora of studies is available for the 4H-SiC structure, the material properties of the SiO_2/4H-SiC structure are largely understudied. In this chapter, first-principles DFT calculations are deployed to reproduce the geometrical properties of the 4H-SiC structure in the most computationally efficient manner, and these are compared against experiments and previous computational studies. This is an important step and builds confidence with the use of the first-principles calculations to simulate the SiO_2/4H-SiC boundary, and furthermore extend the understanding of C_i and defect migration between different sites both in the bulk and at the interface.

This chapter aims to present the calculation of the energetics of 4H-SiC C_i and V_C

defects on the basis of density functional theory, implemented via the software package AIMpro [46]. In this study, the model structures for both carbon interstitial defects and carbon vacancies are produced, while outputting the electronic structures, occupation levels, and binding energies of the defects, before comparing them to the literature [29, 58, 30, 19]. Moreover, the migration behaviours of carbon vacancies and carbon interstitials are investigated with two non-equivalent forms of V_{C} and C_i. The geometric structures and diffusion behaviours of V_{C} and C_i learnt from this chapter will serve as the basis of the studies in subsequent chapters. The identification of the defect behaviours in this chapter will also provide a reference for studying both types of defect in an $\mathrm{SiO_2}$/4H-SiC interface environment in this study.

4.2 Computational method

The first-principles density-functional theory, implemented in AIMpro [46] (as mentioned in chapters 2 and 3) forms the basis of the investigation of V_{C} defects in bulk 4H-SiC. The computations were conducted with three sizes of cells containing 72, 128 and 567 Si and C atom host sites, respectively. The carbon vacancy defects are modelled using a supercell based upon the conventional unit cell of the 4H-SiC structure (eight atoms per unit cell). Analyses of V_{C} in bulk 4H-SiC were previously presented in chapters 2 and 3. For this study, the basis set was selected in order to ensure a convergence of the total energy of the carbon vacancy in a pure 4H-SiC system (see section 2.8 that presents the results of a detailed analyses of V_{C} defects conducted using different Gaussian basis sets). The wave functions were expanded in terms of cartesian Gaussian functions of four widths, yielding 28 functions per atom for C and Si. The calculated in-plane lattice constant for pure 4H-SiC was found to be $a_0 = 3.06\,\text{Å}$ and the out of plane lattice constant was $c = 10.04\,\text{Å}$, which is in an excellent agreement with previous DFT results [5].

A Monkhorst-Pack mesh of (2×2×2) k-points [54] yielding a total energy within 10^{-5} Ha of MP-3^3 was chosen as the sampling frequency (see section 3.1.5). A conjugate gradient scheme was used to obtain the structures optimised for minimum energy, wherein the final energy was accepted only when the final forces were below a threshold of 10^{-3} atomic units. The final structural optimisation step was required to reduce the total energy to be less than 10^{-5} Ha.

The minimum energy paths for diffusion processes of V_C defects in bulk 4H-SiC were determined by using the climbing-image nudged-elastic-band (CI-NEB) method (as described in section 3.2.5 [61, 60]).

4.3 Results and discussion

This section is divided into two parts: the first models carbon vacancy defects 4.3.1.1, and the second examines carbon interstitial defects 4.3.2. For both types of defect, the energy differences at different sites and the role of charge effects, band gaps, and diffusion processes are presented.

4.3.1 Modelling carbon vacancy in crystalline 4H-SiC

4.3.1.1 Geometrical structure

Carbon vacancy defects can occur at two sites in the 4H-SiC structure hexagonal and cubic (as mentioned in chapter 2). These defect sites are shown in figure 4.1. The key difference to note between these two sites is how the second-neighbour environment affects the reconstruction of the defect. In cubic sites, the atoms of the lower silicon layer lie at an angle of 60° between neighbouring carbon and silicon atoms [29, 58, 30, 77]. This immediately raises the question of whether cubic and hexagonal vacancies possess distinct properties. The quantitative and qualitative investigations of the vacancies at lattice sites with local *h* or *k* environments are shown in figure 4.1.

In this section, carbon defect energetics at the hexagonal and cubic sites are calculated and compared against values reported in studies [58, 30]. Using AIMpro code, a key parameter, supercell size, was varied over a considerable range of atoms (71, 128 and 567) for a sensitivity analysis and the energy difference for the hexagonal and cubic sites was subsequently calculated. Table 4.1 shows the energy difference between the hexagonal and cubic sites as calculated by this study and as reported in the literature [58, 30, 19]. It is noted that the calculations from this study are in agreement with the result reported by [58], with very small discrepancy in the values of V_C (0.013 eV) in the natural charge state. In a later study [58], 128 atoms of V_C structure were used to create of one vacancy

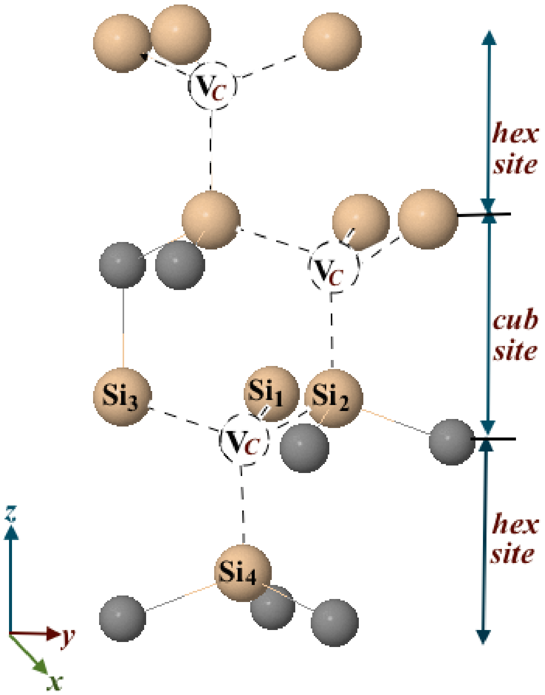

Figure 4.1: Plot shows that the rotation of upper carbon layer by 60° between the cubic and hexagonal site, which appears in the local geometry in V_C in both sites.

on a lattice site, with an MP^2 mesh used to sample the BZ (similar to this study). It should be noted that the energy difference between the hexagonal and cubic sites of the pure 4H-SiC is lower than 1eV irrespective of the supercell size. Therefore, accurate calculations achieved for a bulk SiC supercell containing 128-atoms were used to study properties of V_C. To demonstrate this effect, the occupation of V_C at different sites in the 4H-SiC structure host was firstly examined.

4.3.1.2 Role of charge states

In order to study the behaviour of V_C defects in the bulk 4H-SiC, different structures were investigated with the different charge states. The qualitative properties of V_C defects in the 4H-SiC host structures were examined, as shown in figure 4.2. The schematic structure shows the the second nearest neighbours (2NN) of the vacated site; sites labelled Si_1, Si_2 and Si_3 are in a common basal-plane and site Si_4 is along the c-axis relative to the vacant site. In the neutral charge state, the V_C at the h- and k-sites creates two covalent Si–Si bonds with different bond lengths. As shown in table 4.2, in the case of a neutral charge

Supercell size	EV_C^h – EV_C^k (eV) (Present work)	Previous theory
72 cell	0.157	0.17 [a]
128 cell	0.108	0.12 [b]
567 cell	0.092	0.10 [c]

[a] ref [58]

[b] ref [30]

[c] ref [19]

Table 4.1: The energy difference (eV) between the V_C^h and V_C^k site from this study and from literature with different supercell sizes.

state, there are two neighbouring Si atoms of the vacant site move towards each other and reduce the bonds in the ideal tetrahedral structure [58].

The Si dangling bonds (due to the removal of carbon) form two reconstructed Si–Si covalent bonds, resulting in the pairs of the silicon atoms. Calculations show that the bond lengths of the reconstructions in the V_C^h are 0.31 and 0.29 Å, and 0.29 and 0.38 Å at the k-site shorter than the Si-Si distance in pure 4H-SiC (3.07 Å). This indicates that the values are significantly shorter than the inter-nuclear separation of nearest silicon neighbours in the SiC structure. These calculations on the restructured bond lengths are in close agreement with the previous theoretical calculations by [58, 78]. It should be noted that test calculations were performed for all the tetrahedral distances between the V_C defects and compared against the reference Si–Si bond length, but only the most notable ones are shown in table 4.2.

In order to understand the effects of the charged states on the reconstruction state, simulations were carried out by adding or removing electrons from the system. In principle, if an electron is removed from V_C^0 (as shown in table 4.2), this will result in a positively charged C-site vacancy V_C^{+1} and further lead to an outward relaxation of the system. The Si-Si reconstructed bond-length in V_C^{+1} indicates an increase in both the sites. The table 4.2 as well shows that the V_C^{+1} in the h-site is slightly higher in comparison with the k-site. For the h-site calculations, the bond distance increase is reported for about 3%, and 2%, respectively, in comparison with the corresponding values for the Si-Si distance

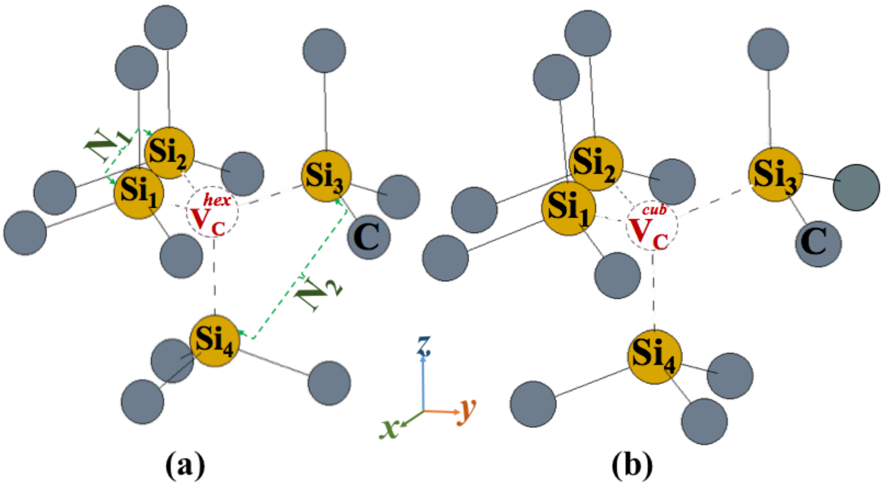

Figure 4.2: Schematic atomic structure indicating the local arrangement of atoms in of V_C labelling the two reconstructed bonds of length N_1 and N_2. C and Si atoms are shown in grey and yellow respectively.

in pure 4H-SiC (3.06 Å).

If an extra electron is removed to form the V_C^{+2} states and the bond lengths of Si atoms the reconstruction are calculated, they are found to be closer to 3.06 Å. This is in good alignment with the calculations and observations from [58, 20]. The system can gain energy by charge redistribution even for quite small changes in the interatomic distances [58]. N_1 and N_2 lengths for V_C^{-1} and V_C^{-2} in comparison with the corresponding values of the bond length in Si–Si bulk 4H-SiC (table 4.2), showing a significant decrease of about 13 and 14 percent respectively. However, these lengths are shown to increase in the case of V_C^{-1}.

The same investigations were conducted for V_C^{k}, and the values for N_1 and N_2 for a k site are slightly different to those reported for an h site in the cases of neutral and positive charges, as shown in table 4.2.

As discussed previously, for a k-site, the values for the positive charges are closer to the inter-nuclear separation of nearest silicon neighbours in the SiC structure (around 3.06 Å). However, calculations show a significant difference in the behaviour for the negative charge states (V_C^{-1} for h sites as compared to k sites). The reconstructed Si–Si bond lengths have shortened by 2.65 Å for N_1 and 2.72 Å for N_2. This shortening of N_1 and widening of N_1 can be explained by the creation of a V_C defect at the h site, as reported in [58, 20].

Charge	N_1	N_2
V_C In h-site		
V_C^{0}	2.76 (10)	2.77 (9)
V_C^{+1}	2.99 (3)	3.03 (1)
V_C^{+2}	2.98 (3)	2.99 (3)
V_C^{-1}	2.57 (16)	2.91 (5)
V_C^{-2}	2.44 (19)	2.93 (4)
V_C In k-site		
V_C^{0}	2.68 (12)	2.77 (9)
V_C^{+1}	2.98 (3)	3.00 (2)
V_C^{+2}	2.97 (3)	3.02 (2)
V_C^{-1}	2.65 (13)	2.72 (11)
V_C^{-2}	2.62 (14)	2.65 (13)

Table 4.2: Reconstructed Si–Si bond-lengths (Å) for V_C in bulk 4H-SiC in different charge states at both the h- and k-site, relative to the Si-Si distance in pure 4H-SiC (3.05–3.06 Å within our computational approach) as indicated in figure 4.2. Values in parentheses indicate the reduction in distance as a percentage of the pure 4H-SiC reference distance.

Similar conclusions can be drawn for the cases of the double positive and negative states. Therefore, this difference in the structure of both h and k sites has a significant impact on the diffusion process, as will be shown later, in section 4.3.1.4.

4.3.1.3 Band structure and electrical level

In this section, the electronic V_C band structures will be discussed together with corresponding experimental data [67, 10, 70]. Figure 4.3 shows the calculated electronic band structures of a V_C defect in a neutral state at an h-site (a) and a k-site (b), plotted along high-symmetry branches in the first BZ. Occupied and unoccupied states are shown in the figure as blue and red lines, respectively. The underlying shaded regions show the electronic band structure for the corresponding bulk SiC supercell (128 atoms). The figure 4.3 indicates that the carbon vacancy at both sites creates deep mid-gap defects in the structure of 4H-SiC. Observing the line with an energy of 1.0 eV for the h and k sites indicates a difference in the defective states and their dispersion (of the order 0.1 eV). These differences can arise due to the change of the stacking sequence of the Si–C bilayers along the c-axis.

As noted in section 3.2.4, the formation energy of the V_{C} defect in 4H-SiC is a function of the chemical potential of the species (calculated as in equation 3.4). The chemical potential of the species calculated with equation 3.2 is further used to calculate the formation energy of a V_{C} defect in 4H-SiC. The formation energies are further calculated to estimate the donor levels located at k and h sites: $E_V + 1.14$ and $E_V + 1.18$ respectively. It should be noted that the hexagonal site levels are slightly lower than the cubic site and in agreement with previous calculations [19].

The double charge state is thermodynamically stable for both k and h sites. This occurs at $E_C - 0.65$, $E_C - 0.41$ eV for V_{C}^{k} and V_{C}^{h}, respectively. These values are close to the values determined using DLTS data [67, 10, 19]. The simulated results from this study indicate that the $Z_{1/2}$ centre has (-2/0) levels located at $E_C - 0.65$ eV, which is in good agreement with observations from [17]. The DLTS peak for $EH_{6/7}$ consists of two closely overlapping peaks with the EH_6 and EH_7 levels, which usually appear together [72].

It is as widely reported in the literature that the $Z_{1/2}$ and EH_7 levels are thought to arise from to the same kind of V_{C} defects with different charge states [67, 10, 74, 17, 70]. According to the present results and correlation with energy position in the band-gap of the $Z_{1/2}$ is determined by DLTS [17] and that of V_{C} by EPR [20, 17], a (-2,0) level could be a possible explanation for the origin of the $Z_{1/2}$ centre.

4.3.1.4 Migration of V_{C} defects in 4H-SiC

In the previous section, the existence of electrical levels that could be conespond to the$Z_{1/2}$ and EH_7 peaks was confirmed. These peaks are considered as the most common deep-level defects in as-grown n-type 4H-SiC, and are directly related to the existence of carbon vacancies in different charged states [20, 2, 19]. This section deals with the migration of carbon vacancies within the 4H-SiC structure at different sites, which could happen when the devices are subjected to post-implantation annealing and subsequent oxidation. These carbon vacancy migrations have been shown to reduce the concentration

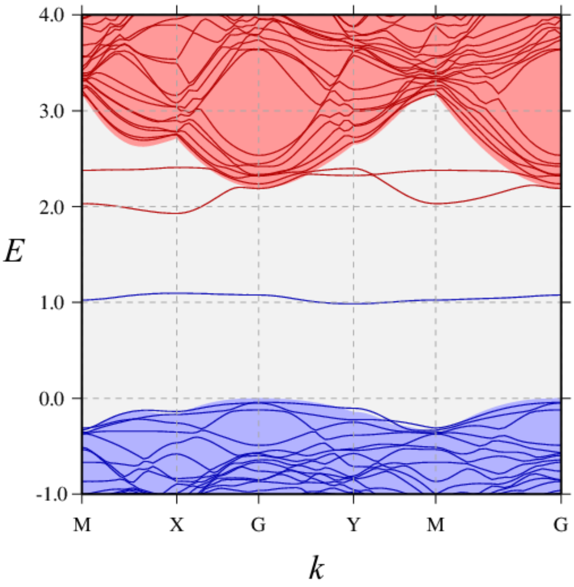

(a)

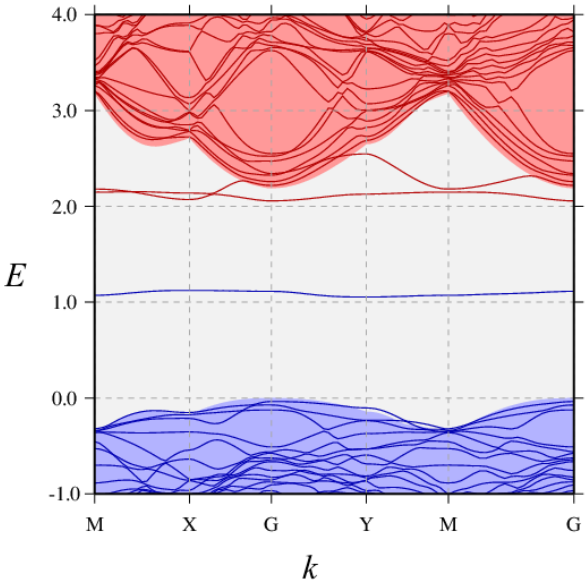

(b)

Figure 4.3: Electronic band structures of V_{C} bulk 4H-SiC: (a) V_{C}^{k}, (b) V_{C}^{h}. Occupied and unoccupied states are depicted as solid blue and red lines respectively, with the envelope of the band-structure for the corresponding defect-free case shown by the underlying shading. The energy scale (eV) is defined such that the valence band maxima are at zero. Only states in the region of the band-gap are plotted

of as-grown defects such as $Z_{1/2}$ and EH_7 [67], and hence it is crucial to understand them in detail. The knowledge from this study can help with decisions relating to the choice of optimal materials and therefore device performance.

In 4H-SiC, migration could be within the same layer (hh or kk) or in the perpendicular direction (hk or kh). Diffusion of carbon vacancies is a key knowledge gap in the understanding of the impact of carbon vacancies on the functionality of 4H-SiC [79]. In this section, we study the diffusion of carbon vacancies by calculating the activation energies required for carbon vacancies to migrate between two sites (h to h, h to k, k to k, k to h) for different charged states. These calculations will determine the reference diffusion barriers for SiO_2 defects in bulk SiC, and will be later be compared with the diffusion of identical defects formed close to the SiO_2 interface (chapter 5).

A vacancy can move through the SiC lattice by direct movement of an atom of the same type from a neighbouring site. As there are two non-equivalent forms of carbon vacancy, as described in section 4.3.1.1, there are multiple diffusion pathways by which the vacancy can move, depending on whether the vacancy is located at a k–site (V_C^k) or an h–site (V_C^h), and the end state, hh, kk and hk. The mechanism of this diffusion was previously described in section 3.2.5. This method is based on determining a minimum from a chain of images between two equilibrium structures. For the current migration study, the minimum energy paths were calculated as described in figure 4.5.

Charge	$h \rightarrow h$	$k \rightarrow h$	$k \rightarrow k$
-2	3.11	3.86	3.35
-1	2.88	3.85	3.80
0	3.34	3.90	3.35
+1	4.18	4.63	4.44
+2	4.97	5.25	5.13

Table 4.3: Activation energies (eV) for the migration of V_C by nearest C-neighbour hops for different charge states.

There are four possible migration pathways for V_C diffusion in bulk 4H-SiC, as shown figure 4.4 [80]:

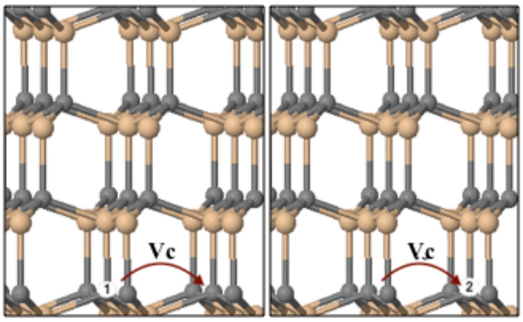

h-site .to. h-site

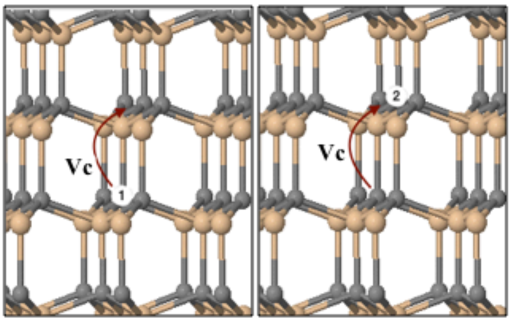

k-site. to .h-site

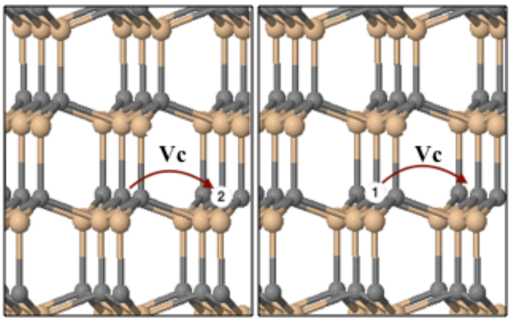

k-site. to. k-site

Figure 4.4: Migration of the V_C in 4H-SiC via nearest-C-neighbour hops. The labels show the types of sites between which the hops take place.

1. Parallel migration of V_C within the same C-layer (*hh* and *kk*) can be described as: the C_1 atom is removed and moves to the next nearest neighbour C_2 (labelled *hh* in figure (4.4-a). Similarly, migration for a *k*- site happens as $C_3 \rightarrow C_4$ (labelled *kk* in figure (4.4-c)).

2. Perpendicular migration of V_C along the *c*-axis (*hk* (in figure 4.4-b), described as: $C_1 \rightarrow C_2$ through the *hk* layer (labelled *kh* in figure (4.4-b)) or $C_3 \rightarrow C_4$ through the *kh* layer.

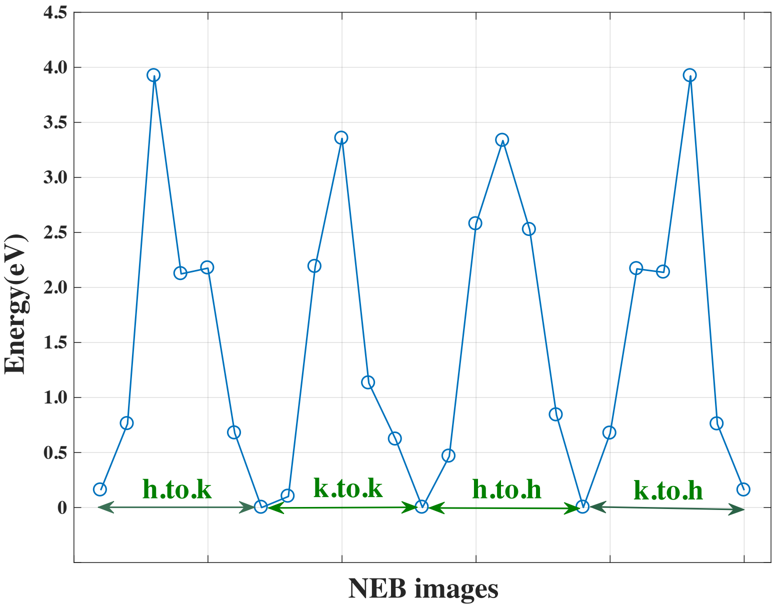

Figure 4.5: Calculated migration barrier of V_{C} in the natural charge state including all three possible migration processes to nearest C neighbour.

These diffusion pathways were simulated using AIMpro by removal and addition of the carbon vacancies as described above. The calculated energy barriers along these path ways calculated are given in table 4.3. For the neutral states the energy barrier values for hh (3.34 eV) and kk (3.35 eV) are comparable but are ten percent lower than for kh migration (3.77 eV). These values suggest that the V_{C} defect moves more freely along in the basal-plane via h- and k-sites than in the orthogonal direction. This may be due to the small local strain field (hk) causing the Si atoms surrounding the V_{C} defect to displace outwards along the perpendicular direction [66, 65], known as asymmetrical relaxation around the defect [66]. This lowers the distance between the second C neighbours and the V_{C} defect in the parallel direction as opposed to the perpendicular direction, and hence lowering the energy barrier for diffusion. The difference between the energy barrier for an hh site (3.34 eV) and a kk site (3.35 eV) can be explained by the difference in the formation energies. Figure 4.5 describes the minimum energy pathway and shows as the intermediate minimum for perpendicular migration hk or kh but not for parallel migration hh or kk cases. This might be due to a reorientation of the Si–Si bond (due to the carbon vacancy) between out plane Si–Si atoms (kh) against a case where the Si–Si bond reconstructs within the plane (hh or kk migration).

The calculations shown in the table 4.3 for *hh* and *kh* suggest that the reorientations of a Si–atom can take place with barriers of around 0.5 eV, while the migration of a V_{C} via *kh* has an energy barrier of 3.90 eV. Simulations from the neutral states were extended to include the effect of charged states and the energy barriers along the different pathways were calculated (table 4.3). It can be observed that the calculated values for *hh* migration are lower than the corresponding *kk* migration for all the charged states from +2 to -2, and the gap is significantly greater than that found with neutral states. These differences can again be explained due to differences in the formation energies of the two sites (section 4.3.1.2). Furthermore, it should be noted that the energy barrier for the positive charge states (+2 and +1) across all migration pathways (*hh*, *hk*, *kh* and *kk*) is always higher than the negative charges states (-2 and -1).

For instance, for *hh*, the +2 charge state value for the energy barrier is 4.97eV, whereas for the -2 charge state, the value is 3.11eV. This may be a consequence of the different geometric rearrangements: there are two Si–Si reconstructed covalent bonds for the positive state, meaning the dangling bonds are located at the nearest-neighbour Si atoms at a distance of 3.06 Å, as in the ideal SiC crystal, and cannot substantially overlap. Therefore, the process involves the breaking of a stronger C–Si bond. Thus, this process gives a higher barrier, as explained in 4.3.1.1. These calculations are consistent with previously reported theoretical results based on density functional theory calculations [81, 57].

4.3.2 Modelling of C_i defect in crystalline 4H-SiC

4.3.2.1 Geometrical structure of single C_i

As shown in the previous section, there is one form of carbon vacancy, V_{C}, which can exist in SiC (regardless of whether the different sites in the 4H-SiC). However, there are various forms of carbon interstitial configurations that have been explored in SiC materials [82]. Figure 4.6 shows carbon interstitial configurations that can exist in SiC. For example, it is agreed that the tetrahedral site of carbon C_{TC} (the site of carbon that is surrounded by four carbon atoms as shown in site (4) in figure 4.6) is considered an unstable site [7]. The primary reason for this is due to the fact that the C_i relaxes towards the nearest neighbours into a more favourable split-interstitial configuration. Another possible configuration of the interstitial is the carbon-silicon split-interstitial (C–Si)$_\mathrm{C}$ (this is shown in site (1) in figure 4.6), but this is found to be less stable than (C–C)$_\mathrm{C}$ [29]. However, the hexagons (hex) perpendicular to the basal plane C_h as shown in the site (4) of figure 4.6 is energetically unstable [7]. This site plays an important role in the migration mechanisms, and will be discussed in section 4.3.2.2.

Carbon interstitial defects can have additional configurations the 4H-SiC structure [32], which can be distinguished by their different nearest neighbourhood configurations, and primarily arise due to different resulting relaxation patterns (figure 4.6). The primary reason for the wide variation of these configurations can be attributed to orientation changes in the stacking sequence at the hexagonal sites, which results in a different bonding to the nearest neighbours as compared to the cubic sites in the 4H-SiC lattice. In general, carbon interstitials have a tendency to form short bonds with their direct carbon neighbours. The ground state of a single carbon interstitial in 4H-SiC is understood to primarily form a split–interstitial configuration [33, 7], which is formed when two atoms share a single site (figure 4.7).

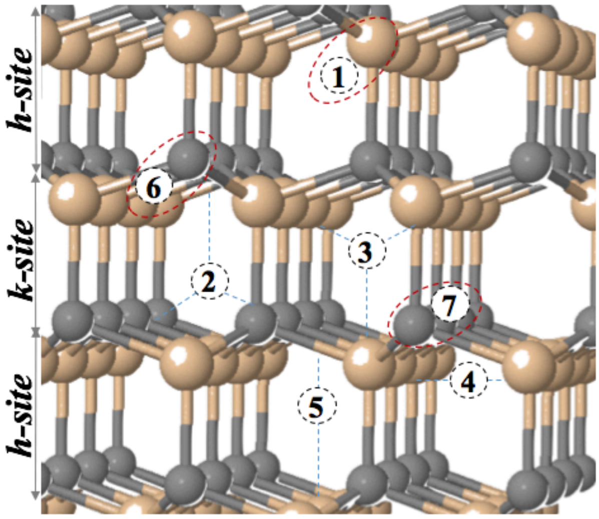

Figure 4.6: Schematic of the carbon split-interstitial models in 4H-SiC bulk: (1) refers to the carbon-silicon split-interstitial (C-Si)$_\mathrm{C}$, while the positions 6 and 7 are the carbon-carbon split-interstitial (C-C)$_\mathrm{C}$ in k- and h-sites respectively. Position (2) refers to the hexagonal site of the carbon interstitial, which either possess a silicon-like C_{TSi} or (3) carbon-like C_{TC} surrounding. (4) site is the interstitial site in the hexagonal plane C_{Hex}.

It can be seen in this figure that the carbon split-interstitials involve both sp^3 and sp^2 hybridisations, depending on whether the interstitial is located at a hexagonal or cubic site. The single carbon interstitial defect is studied in the bulk SiC. It can also be seen that the addition of a carbon atom leads to an increase by 10 % in the volume of the tetrahedron, defined by the four silicon atoms including the C-C pair. This is true for both *h* and *k* sites. Based on the computational studies using AIMpro, the resulting bond lengths between the carbon atoms and the enclosing silicon tetrahedron are summarised in table 4.4. In this table, the distance of band length parameters in both configurations of defect at the *k*- and *h*-sites in 4H-SiC can be seen. The bond lengths between the carbon pairs were found to be 1.35 and 1.33 Å in the *k*- and the *h*-sites, respectively. This leads to a reduction in the C–C bond length by around 0.07 Å. In comparison, the bond length between these C-atoms in graphene is around 1.407 Å. In the case at an *h*-site, it is found that the C_1 - C_2 atoms bonded with four Si neighbours, while the $Si_{3,4}$ was nearly equal, while the Si_1 was pushed outwards, and the bonds created increased slightly in length because of the presence of $(C\text{-}C)_C$.

In contrast, the results of *k*-site structural calculations when a $(C\text{-}C)_C$ defect is present show that there are five silicon atoms bonded to the defect, with a bond length varies between 1.80 and 1.81 Å, which is much less than at the *h*-site, although a similar mechanism occurs in both sites. The computational results are in close agreement with the DFT calculations by [7] and the results are included in the parentheses in table 4.4.

Bond	*k*-site	*h*-site
C_1 - C_2	1.35 (1.35)	1.33 (1.33
C_1 - Si_3	1.81 (1.83)	1.77 (1.77)
C_1 - Si_4	1.81 (1.83)	1.77 (1.77)
C_2 - Si_1	1.82 (1.88)	1.78 (1.77)
C_2 - Si_2	1.82 (1.88)	1.75 (1.76)
C_2 - Si_5	1.99 (1.88)	–

Table 4.4: Bond lengths Å of the neutral carbon $(C\text{-}C)_C$ in 4H-SiC. The indices of the atoms refer to figure 4.7,and values in parentheses indicate a reference [7].

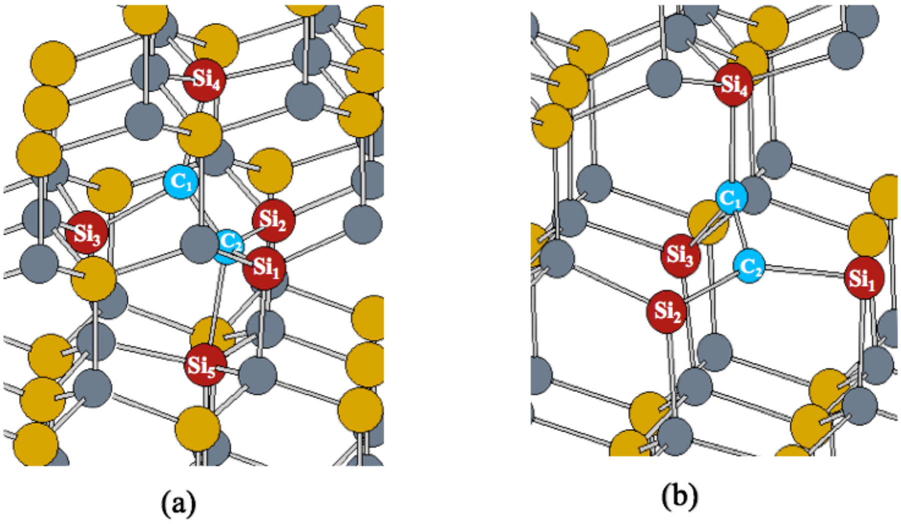

Figure 4.7: Schematic of the $(C\text{-}C)_C$ configurations in 4H-SiC: (a) in *h*-site, (b)in *k*-site.

The electronic band structures of single carbon split interstitial defects $(C\text{-}C)_C$ in the neutral state and at two sites, (a) *h*-sites; (b) *k*-sites are shown in figure 4.8. Single carbon split interstitial defects create defect states within the 4H-SiC band gap. The unoccupied and occupied states are found in the band-gap. The defect is composed of the sp^2 hybridised carbon atoms, which are presented for the occupied levels in the band gap. An unoccupied level leads to a shift in the *p* orbital to a higher energy level, which are located at 1.9 and 2 eV below the CB for *h*- and *k*-sites respectively. This is because both the carbon atoms in $(C\text{-}C)_C$ are sp^2 hybridised, and this introduces a two-fold degenerate defect level into the band gap and the C-site [34]. The $(C\text{-}C)_C$ defects were further observed experimentally and also by theoretical calculations of the hyperfine tensor [75, 34].

4.3.2.2 Migration of $(C\text{-}C)_C$ in 4H-SiC

The migration of $(C\text{-}C)_C$ in the bulk 4H-SiC is used to calculate the activation energy for $(C\text{-}C)_C$ with all the possible charged states. Figure 4.9 shows the two different configurations of the C_i defect depending upon on the charge state. It is obvious that there is a symmetrical pattern in case of the positive charge states, whereas, in the case of the neutral and negative charge states, barriers are found due to the differences in the activation energy of each of configuration in which reorientation and rotation processes

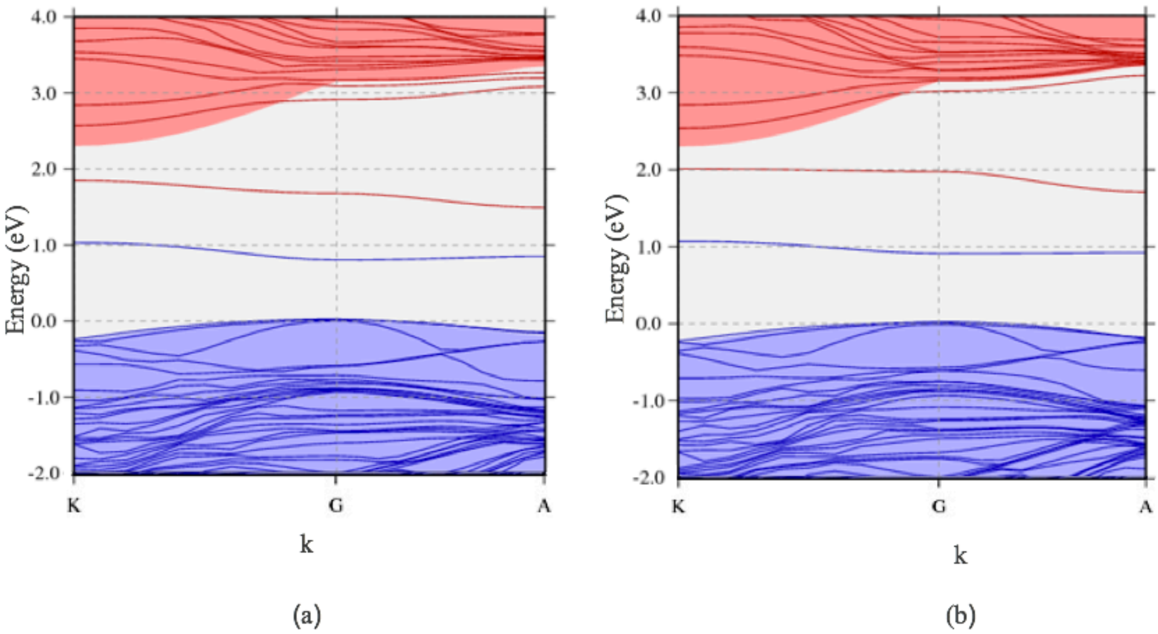

Figure 4.8: Electronic band structures of single carbon split interstitial defects for (C-C)$_C$ in the neutral state in 4H-SiC, (a) *h*-site and (b)*k*-site.

occur. The focus of this work is on the migration of (C-C)$_C$, as all the other forms (*k*, *h* and *kh*) behave with the same diffusion mechanism.

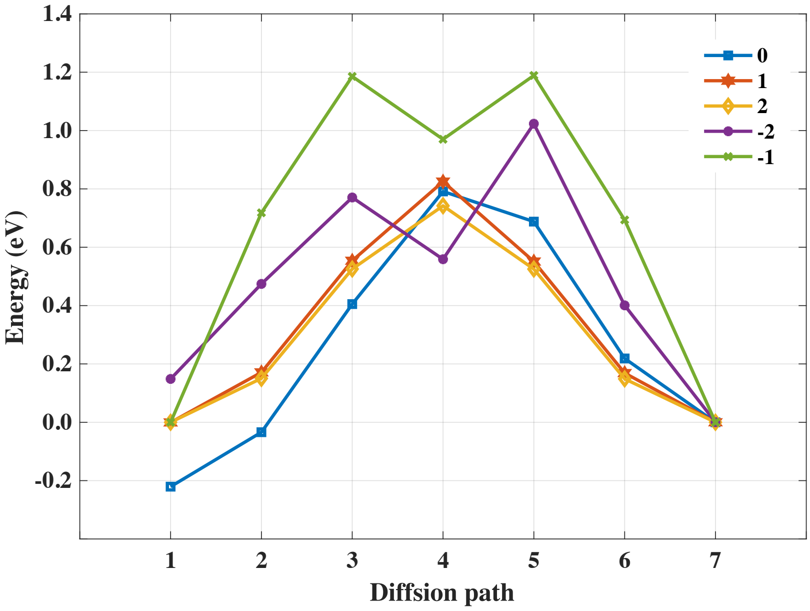

Figure 4.9: Minimum energy paths for (C-C)$_C$ in bulk 4H-SiC for different charge states.

The computational results obtained show that the activation energies of a (C-C)$_C$, in the negative and neutral charge states have an intermediate structure, in contrast to the other positive states(figure 4.9). This is probably due to the differences in the structure of charge states. This defect is found in the charge states +2 and 0. A reorientation into a more favourable orientation yields an energy gain of about 0.2 eV. The reason for the former to being a very unfavourable orientation of the carbon orbitals to their nearest silicon neighbours is that the resulting distance required for the C-atom to move in the diffusion process is greater.

4.3.2.3 Geometrical structure of C$_i$ pairs

Di-interstitial defects in 4H-SiC can be considered as nuclei for the growth of larger groups of interstitial defects (clusters). The mobility of C$_i$ defect (0.78 eV) is reported to be higher in comparison with vacancy defects. This means that a cluster of interstitials is likely to be present in a high range of temperatures and irradiation conditions [29]. Therefore, understanding the structure of this type of defect could give a clearer understanding of the existence of these clusters.

Di-interstitial defects in 4H-SiC are carbon lattice atoms that share their position with two carbon interstitials as opposed to one (see section 4.3.2). These can be denoted as 2C$_i$. In theory, there are many plausible locations for an interstitial in the lattice, but not all are stable. Based on the calculations, the most stable configurations of 2C$_i$ are those which contain a hexagonal ring [33, 7, 34]. These hexagonal di-interstitials can be located in the cubic and the hexagonal planes, and it should be noted that the difference between the *h* and *k* sites for this structure is minor (as shown in figure 4.10).

Structural rearrangements occur due to the addition of two carbon atoms as compared with Si–C in bulk SiC and C–C in graphite. Table 4.5 summarises the results of the computational studies to model di-interstitial configurations using the AIMpro package. In this configuration, the carbon pair bonds to two silicon atoms (Si$_1$ and Si$_2$) and two carbon atoms (C$_1$ and C$_2$). The C$_i$–Si$_2$ distances are calculated to be 1.74 Å, leading to a reduction of the Si–C bond length by around 0.13 Å as compared with the bonds in SiC for either *h* or *k* sites. It is further observed that the stronger C$_i$–C$_1$ bonds are formed with a distance of 1.35–1.36 Å, which can be compared to the experimental values

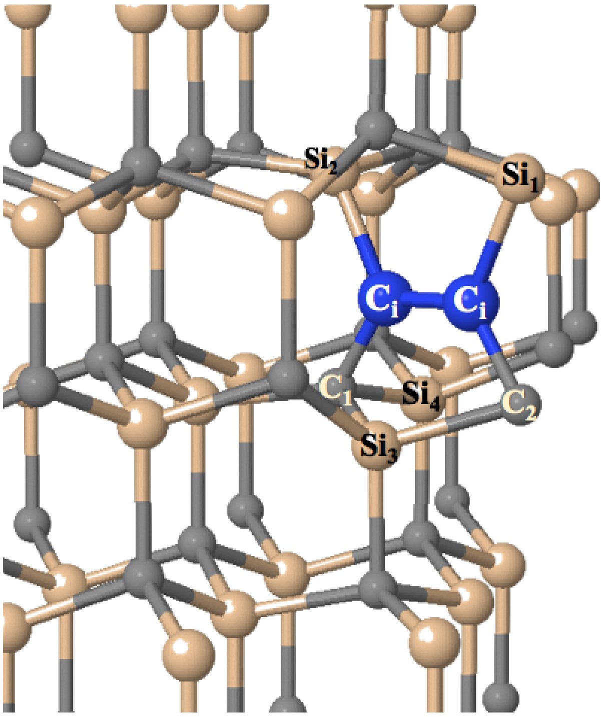

Figure 4.10: Schematic of di-Interstitial configurations in 4H-SiC.

Bond	k-site	h-site
C_i - C_i	1.36	1.35
C_i - Si_2	1.74	1.73
C_i - Si_1	1.74	1.73
C_i - C_2	1.42	1.42
C_i - C_1	1.43	1.42

Table 4.5: Bond lengths of the neutral carbon $(C\text{-}C)_C$ for di-interstitial configurations in the 4H-SiC lattice. The indices of the atoms refer to figure 4.10.

with C–C sp^2 bound length in graphite [83]. (1.54 Å). This finding is in agreement with previous studies [7]. The angle between Si_1,C_i and the Si_2 from the sp^2 hybridisation of the carbon atoms is 120.3°. It is expected that there will be a sizeable energy barrier for diffusion, since the diffusion process requires the breaking of two carbon bonds.

The electronic band structures of di-interstitial defect pairs C_i have been computationally studied, as shown in figure 4.8. It can be seen that the defect levels in the conduction bands are localised, and the lowest band above the band gap shows a lower dispersion than the conduction bands of the pure crystal (figure 4.11).

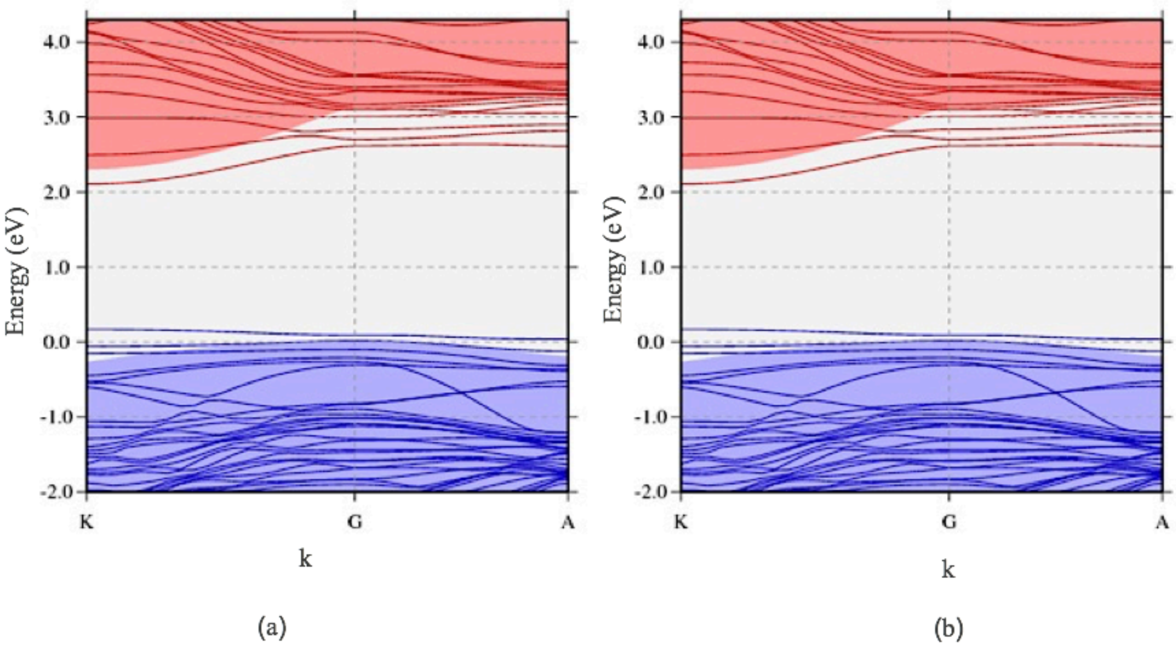

Figure 4.11: Electronic band structures of single carbon split interstitial defects for $2C_i$ in the neutral state in 4H-SiC, (a) *k*-site and (b) *h*-site.

As seen from the plot, it is clear that there are no associated deep levels within the band structure. Based on these results, the $2C_i$ defects in the bulk SiC cannot explain the experimentally observed peak, which is responsible for high trap density (correlation with defect levels in the lower part of the SiC band gap). Based on the current calculations, the $(C\text{-}C)_C$ defect appears to be the simplest and the most likely structure to be formed during the annealing process, and this is in agreement with the low migration barrier studies [29]. Therefore the positive outcomes obtained from $(C\text{-}C)_C$ calculations are provided as the basis for the extension of this study to a more complex system at the interface.

4.4 Chapter summary

In this chapter, the first-principles density-functional based simulations were conducted to study the electronic structures of 4H-SiC of the carbon vacancies. These carbon vacancies within the 4H-SiC structure were created at different sites (*h* and *k*) and different charged states from +2 to -2 were studied in detail to cover changes in the geometric structure and band structures and as well as electronic levels.

The calculations based on first-principles simulations show that there are slight variations with inequivalent lattice sites in h or k bilayers in the unit cell, although the difference in the energy of V_{C} is quite small (in agreement with the literature [19]). This difference was found to increase with charged states due to relaxation after the removal of the carbon atom, and the chemistry resulted in the covalent bonds between Si atoms around a defect begin in the different charged states. Simulations studying the electrical activity of V_{C} for h and k sites at different charged states support the assignment of the double acceptor level to $Z_{1/2}$ and $EH_{6/7}$ to the single donor level.This is in agreement with prevouse studies [19, 70, 3]. In the latter part of the chapter, simulations were carried out for all the possible migration pathways, that is, parallel and perpendicular directions of V_{C} defects in 4H/SiC as well as different charged states.

Calculations for the two different migration directions suggest that the V_{C} defect moves more freely in the basal plane via h and k sites than in the orthogonal direction. The energy barrier for the positive charge states across all migration pathways is higher than for the negative charged states. This is due to the fact that the process involves the breaking of Si–C covalent bonds and the forming of Si–Si bonds. Furthermore, single and di-interstitial carbon defects were successfully reproduced computationally using the AIMpro package. The electronic and band calculations are in excellent agreement with other results [29, 7].

In summary, it is concluded that the simulations and calculations carried out using AIMpro in this chapter are in excellent agreement with the experimental and theoretical results. The conclusions of this chapter validate the use of this methodology to analyse carbon vacancy defects in a more complex environment, i.e. V_{C} defects in the vicinity of an $\mathrm{SiO_2}$/4H-SiC interface. In the next chapter, these scenarios will be studied in detail and further compared with the results of this chapter.

Chapter 5

Structural models of the SiO_2/(0001)4H-SiC interfaces

5.1 Introduction

As discussed in chapter 1, the high interface state densities at the SiC/SiO_2 interfaces (value can be greater than 10^{13} cm^{-2} eV^{-1}) are typically located closer to the 4H-SiC conduction-band edge [84, 40]. These high state densities at SiC/SiO_2 interfaces result from atomic level disorders [85]. A thorough understanding of the geometry and the bonding structures in the vicinity of the SiO_2 and 4H-SiC region can determine the interface characteristics, and clarify how the bonding structure impacts these characteristics.

A large amount of research effort has been dedicated to the development of processing techniques aimed at reducing trap densities [84, 86, 87, 88]. The majority of the works directed at improving interface quality have focussed on the Si-terminated face of 4H-SiC, while while the results in Dhar et al. [84] indicate that in some of the cases (dry oxidation), the C-face has a considerably higher trap density than the Si-face, likely due to the presence of a larger number of carbon clusters on the C-face. Additional studies have compared the C-face and the Si-face on 4H-SiC orientations during dry oxidation, in a bid to form oxide have been reported [85]. However, the mechanism responsible for the D_{it} reduction into the SiC/SiO_2 interface is still not fully understood.

Quantum mechanical modelling is considered a useful route for gaining insight into the microscopic nature of D_{it} at the SiC/SiO_2 interfaces, which is otherwise not possible via experiments. In order to identify the origin of the D_{it}, a SiO_2/4H-SiC interface model with good structural and electronic properties is essential. Modelling the evolution of the SiO_2/SiC interface is computationally challenging. Previously, theoretical studies of the defects at the SiC/SiO_2 interface used simplified model systems to address the interface [89]. The first attempt to model the interface was made by Knaup *et. al*, who attached two SiO_2 layers to the 4H(0001)SiC substrate, and saturated all bonds at the interface [76]. Devynck *et. al* generated a SiO_2/(0001)4H-SiC interface slab model by using *abinitio* simulation methods; the results showed a better model technique, as it included a larger SiO_2 layer with a proper experimental density of SiO_2 average (2.5 g/cm^3). This was close to oxide densities near the interface found in models of the Si/SiO_2 interface (2.4 g/cm^3) [21]. Therefore, constructing a model interface with a realistic interfacial bond pattern will significantly extend the studies of near interface defects.

The purpose of this chapter is to provide insights into the structural properties at the interface, in particular, to provide insights into the structural differences that occur due to different slab configurations at the interfaces. These patterns can be differentiated as a slab attached to either of the C-face or Si-face, with a defect situated at either of the h or k site (refer to figure 5.1). In this chapter, the modelling work is undertaken using the AIMpro software package with the following main objectives:

1. Ascertain the appropriate model parameters to determine a SiO_2 and interface model structure, based on DFT, using the AIMpro software;

2. Examine geometrical differences between h-face, k-face and Si-face, C-face at the interfaces resulting from differences in 4H-SiC carbon vacancy occurring at either h- or k-sites

3. Examine the 4H-SiC slab thickness effect on the activation energy.

In order to obtain an understanding of technologically important defects in the interface, this is discussed in details in subsequent chapters. This includes the model systems for future carbon vacancy studies (chapter 6) and carbon interstitial defect studies (chapter 7).

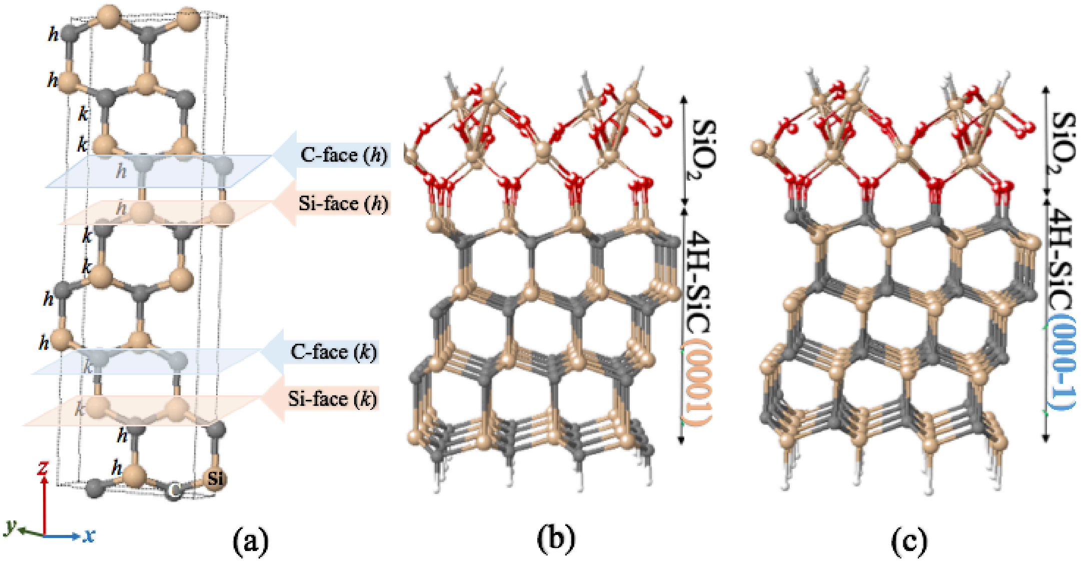

Figure 5.1: Schematic diagrams showing: (a) the lattice structure of 4H-SiC. in 4H-SiC, there are two inequivalent faces are indicated by the light blue plane (h and k-face for C-face) and the light orange plane (h and k-faces for Si-face). (b) and (c) show the models for the SiO_2/(0001)4H-SiC and SiO_2/(000$\bar{1}$)4H-SiC interface, respectively.

5.2 Computational Details

Chapter 2 describes the modelling parameters and algorithms used to optimise a computationally feasible study. In this section, the results of chapter 2 were leveraged to obtain the base simulation parameters, the basis set (see section 3.1.3), the band structure (see section 3.2.3) and the minimum energy path for the diffusion processes of V_C (section 3.2.5). The same computational approach as used in chapter 4 was deployed to model the SiO_2/4H-SiC(0001) and SiO_2/4H-SiC(000$\bar{1}$) systems.

A model structure of a SiO_2/(0001)-4H-SiC was created using the AIMpro software, and optimised to run computationally feasible simulations. For this purpose, the minimum cross-section of the structure determined the number of Si and C atoms per atomic plane. In this study, an optimised cross-section was found to include one atom of (Si or C) and there were eight C and Si atoms per layer; the in-plane footprint was repeated for each in-plane direction to yield 32 atoms of Si and C per layer, with five layers in total. This resulted in the basic interface model, which included a total of 204 atoms, as shown in the figure 5.2. A thin layer (48-atoms) of SiO$_2$, situated on top of the Si-face of a 128-atom 4H-SiC slab, was taken to be the initial structure (the number of atoms in the thin layer and 4H-SiC slab thickness were used as parameters for optimisation). The lower layer of the 4H-SiC slabs were saturated with 24 hydrogen atoms to remove their surface states, as were the dangling bond sites of the SiO$_2$. Furthermore, the bottom Si, C and H layers are held fixed in the simulations to mimic the long range constraints of the bulk SiC. The angles and bond-lengths were concurrent with the bulk SiO$_2$ structural parameters. Therefor, this system was similar to a previous modelling study of the same system type [21].

The computational model for this study included three sets of s and p Gaussian functions, totalling to 12-functions per H atom. The Kohn-Sham functions were expanded using the Gaussian basis sets (see section 3.1.3). The wave function and charge density were expanded in terms of Gaussian orbitals on 40 function per atom (four sets of Gaussian up to and including d-functions), and were optimised to represent both Si and O in SiO$_2$. The wave function was expanded in terms of Gaussian orbital, using 28 functions per atom basis sets, which were used to represent Si and C in the 4H-SiC slab (see section 3.1.3). Controlled calculations were performed using bulk 4H-SiC supercell, which were comparable to the SiC section of the slab model. Relaxation was performed until the interatomic forces were below 0.016 eV. The Brillouin zone was sampled with a MP grid of $[5 \times 5 \times 4]$ k-points, which was converged to better than 1meV/atom. To ascertain a computationally optimised sample size (see section 3.1.3), the total energy of the structure was calculated as a function of sample size, with the Γ point, which yielded energy differences, converging to roughly 2 meV (used in the remainder of the study).

5.3 Results and Discussion

In this section, we present simulation results to address two key points about the numerical reproduction of two structures: 1) SiO$_2$ bulk structure, 2) 4H-SiC (0001) slab structure. In the latter case, an investigation of the choices related to various converged parameters is undertaken, including activation energy convergence using the 4H-SiC slab thickness.

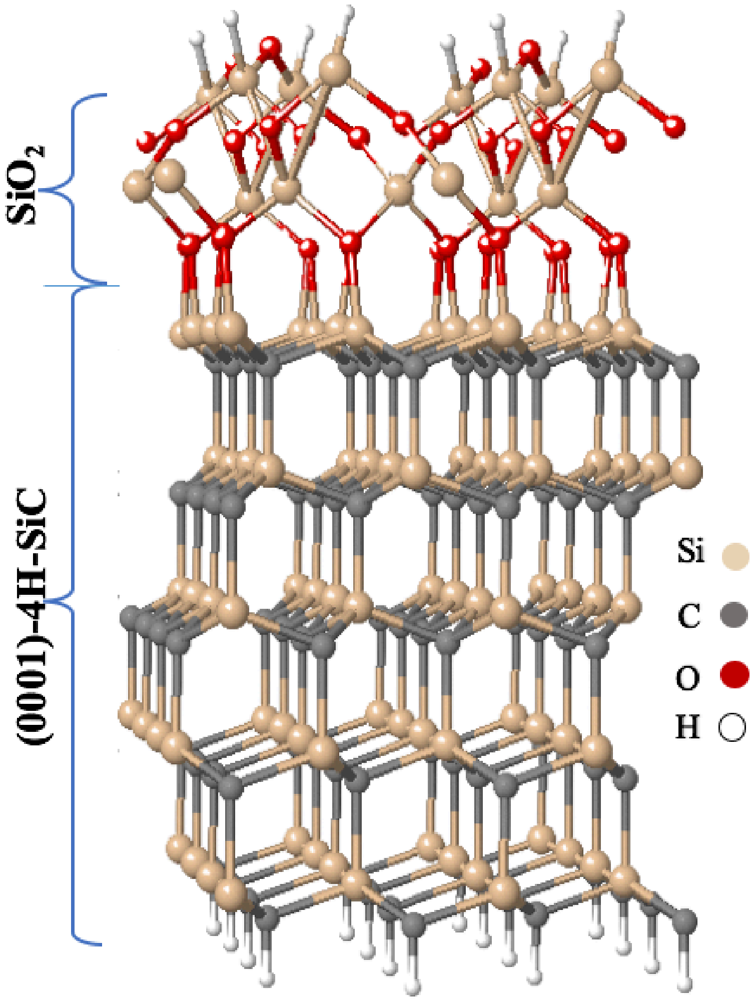

Figure 5.2: Schematic illustrations of SiO_2/(0001)4H-SiC.

5.3.1 The SiO_2 bulk structure

This section outlines the optimisation of the numerical approach and computational model required to model the SiO_2 bulk structure. Specifically, the principal computational results related to the bond lengths and the angles in the SiO $_2$ structure was compared with the literature studies [21, 76]. In this study, the amorphous form of SiO_2 is modelled as an alpha quartz (α-quartz)structure, and was chosen due to its known stability at room temperature and its similarity to the underlying hexagonal pattern within the 4H-SiC substrate [90].

The SiO_2 structure was simulated as a primitive cell containing nine atoms: six oxygen and three silicon atoms, and each O-atom had two Si neighbours. Table 5.1 presents the calculated geometric parameters, including the lattice constant, and bond lengths for DFT optimised for the SiO$_2$ structure. Theoretical and experimental values were also included in the table for the comparison purposes.

Property	Current calculations	Theory [21]	Experiment [91]
a_0	9.06	9.09	9.29
c	10.03	10.12	10.29
O–Si	1.63	1.66	1.61
$\angle Si - O - Si$	132.87°	137.10°	143.87°
$\angle O - Si - O$	109.75°	109.50°	109.47°

Table 5.1: Calculated (Current calculations), experimental and theoretical values of the lattice parameters (a_0 and c) (Å), the bond-length (Å) and the bond-angle of the SiO$_2$. The theoretical data and experimental is taken from previous studies.

All the O–Si–O angles were very close to the ideal tetrahedral value of 109.45 ° [21, 91, 92] (table 5.1). However, the calculations show that the average of Si–O–Si bond angle was 132.87°. The Si-O-Si band angle can be extending from 110° to 180°, which reflects the significant flexibility of this configuration [93]. This result deviated slightly from the experimental values, which resulted in the less expanded lattices. The lattice parameter calculation is comparable to the experimentally observed values and agreement with previous calculations [91].

5.3.2 The model of the SiO$_2$/(0001)4H-SiC

The two faces, i.e. the C-face, $(000\bar{1})$ and the Si-face, (0001) of interface orientation for the 4H-SiC slab were compared for each face s interface structure with two non-equivalent C (in Si-face) or Si (in C-face)sites per unit cell, as shown in figure 5.1. Accordingly, the topmost C or Si layer configuration can include the atoms in the *h*-face or *k*-face in the 4H-SiC crystal structure.

5.3.2.1 Clean interface parameters

As discussed in the section 5.2, a 4H-SiC layer is placed on the top of the SiO$_2$ layers. After optimisation of the atomic positions, the resultant SiO$_2$ layers covalently bond to the 4H-SiC layer (as shown in figure 5.3). During the interface optimisation of the ideal structures, it was found that the geometrical arrangement of the surface atoms were the same as for the 4H-SiC bulk structure. It was therefore concluded that the relaxation changes has an impact up to the interlayer spacings but not beyond; the surface unit cell does not change [94, 53]. Figure 5.3 shows the side views of the interface structures, where the first layers of each face are different. Table 5.2 summarises the simulated interface layer distances with respect to the ideal 4H-SiC bulk structure distances. The negative signals the presence of a contraction, while a positive sign signifies expansion of the interlayer spacing. The topmost Si atoms of the Si-faces moved by 0.02 Å, while the topmost C atoms of the C-faces led to an inward displacements of 0.09 Å, compared to the interlayer 4H-SiC bulk distance. The deeper layers showed insignificant relaxation and were in fair agreement with the results of previous studies [95] for both Si- and C-faces. Furthermore, the relaxation of the interlayers in the z direction was calculated to be relatively insignificant, with a hight of 0.02 Å as its position in bulk material (table 5.2). The third layer was found not to have any displacement of atoms at all, and all similarly, all subsequent layers remained in their bulk-like positions, where comparable displacements were reported here [95, 96], and when compared quantitatively, showed an excellent agreement. It should be noted that the k-face generally exhibited an inward relaxation, while an outward relaxation was observed for the h-face in both the C and Si faces. Additionally, it can be seen that the Si-face exhibited a lower effect of the interface layer, compared to the C-face. It is noted that the variations in the interlayer spacings for near layers associated with the C-face were different to those for the Si-face interface, but showed a similar trend.

The structure of a SiO_2/(0001)4H-SiC interface was simulated using the alternating slabs. There were two important considerations when modelling this structure: a) the 4H-SiC crystal slab had to be thick enough to prevent relaxation of atoms near the SiO_2, and the position of atoms can be fixed to their positions in the bulk material to a specific depth within the surface (common practice, as reported previously in [97]); b) the vacuum region between the two slabs should be wide enough to isolate the two slabs (see section 3.1.4).

In order to determine an optimised slab thickness, a convergence test was conducted. As discussed in the section 5.2, the basic interface model included a total of 204 atoms with

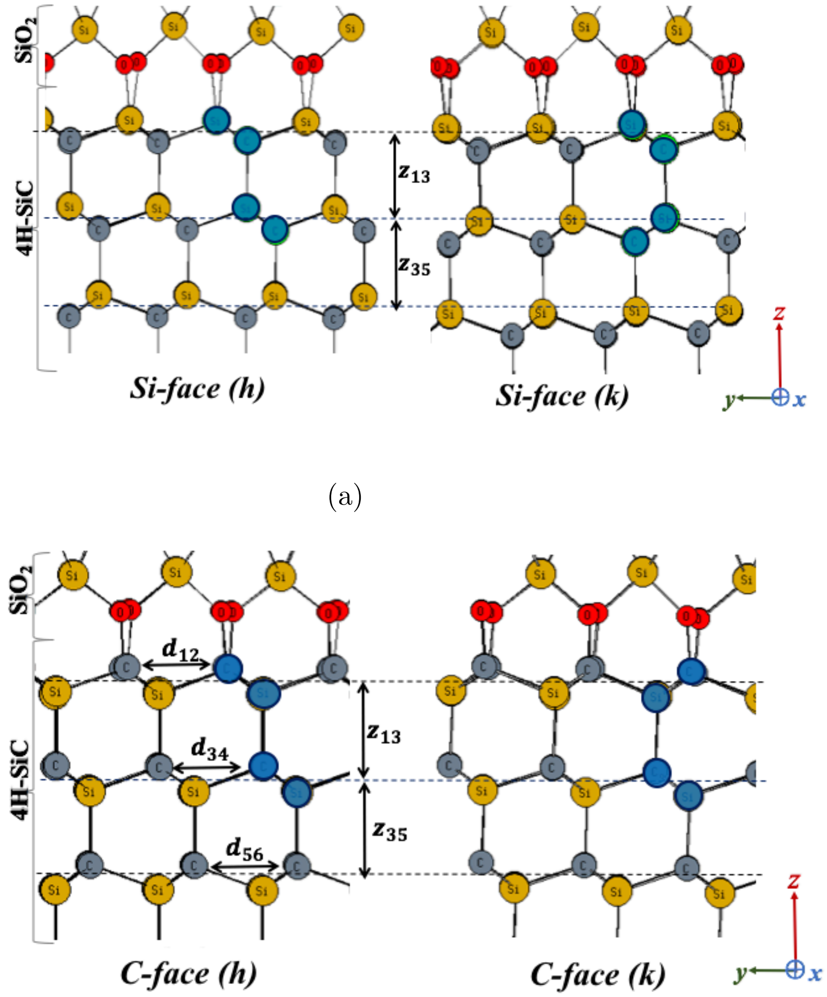
SiO$_2$
4H-SiC
z_{13}
z_{35}
Si-face (h)
Si-face (k)
z
y
x
d_{12}
d_{34}
d_{56}
C-face (h)
C-face (k)

(a)

(b)

Figure 5.3: Schematic diagram showing a side view of the Si-face at the SiO$_2$/4H-SiC interface. Grey, yellow and red atoms represent C, Si and O respectively. Relaxed atomic geometries for the SiO$_2$/(000$\bar{1}$) 4H-SiC interface, with: *h*-face and *k*-face. Also, the figure shows the differences in the z-position for pairs of atoms given in each layers in the interface. All distances are given in Å.

Face	d_{12}	d_{34}	d_{56}	z_{13}	z_{35}
C-face (k)	-0.09	+0.02	0	-0.02	0
C-face (h)	+0.05	-0.02	0	-0.01	0
Si-face (k)	-0.03	+0.01	0	-0.02	0
Si-face (h)	+0.02	-0.02	0	-0.01	0

Table 5.2: The atomic geometry of the 4H-SiC interface for the structure, compared to the ideal 4H-SiC bulk structure, where d_{ij} refers to the distance between interface layers numbers, while z_{13} refers to the distance between the positions of two atoms in different layers, as shown in figure 5.3. The negative sign refers to a contraction and the positive sign indicates an expansion of the interlayer spacing. All distances are given in Å.

32 Si–C atoms in each extended layer in the z-direction. The number of atoms per slab (including both SiC and SiO_2) were systematically varied by including additional layers in the SiC. The resulting systems contain 204 (*basic*), 268 and 332 atoms. The energy difference between the non-equivalent forms where the Si-layer of the SiC connected to the SiO_2 is either a set of h-sites or k-sites was found to be within 1 meV of 27 meV per atom at the interface for all cell sizes. The difference in energy arises from the detailed differences in bond-polarity in at the interface and at the lower surface, so should not be interpreted as having a direct meaning for a SiC/SiO_2 interface. However, the fact that the energy difference is very weakly dependent upon the number of SiC layers provides some confidence that even the basic structure is not significantly affected by the cell size. To summarise the results of this section: the Si-face is most commonly used for the growth process [98, 26, 4, 2]. After building the structure of the interface varied with all the possible configurations, the next step was to introduce where the V_C at a range of non-equivalent sites. In this study, calculations for the geometrical differences of the bond length deviation in each of these faces (h and k) were examined.

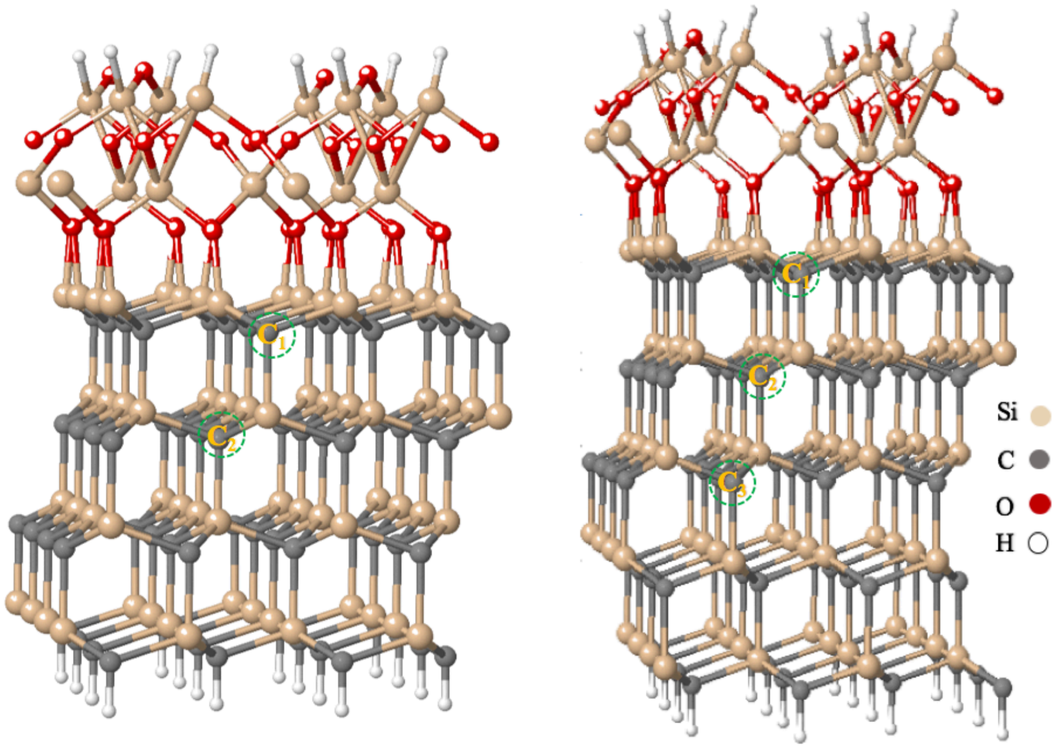

(a)

(b)

Figure 5.4: Schematic diagrams showing: a side view of the Si-face (0001) at the SiO$_2$/4H-SiC interface; grey, yellow and red atoms represent C, Si and O respectively. The 4H-SiC slab is linked with the oxide layers on the top of the slab. The (a) 204 and (b) 268-slab thickness.

5.3.3 Investigation of defects at the SiO_2/(0001) 4H-SiC

5.3.3.1 Model of the V_{C} at both non-equivalent sites

In order to include the model of V_{C} at interfaces, DFT calculations were performed. Firstly, atomic geometries were optimised following the introduction of the vacancy, and compared with the defect-free interface structures. Table 5.3 provides the results of a statistical analysis of the the silicon atoms' positions, which were located adjacent to the first interface. The displacement in the [0001]-direction, relative to the location of the comparable atom in the defect-free slab, was calculated. For the V_{C}^{hf} deformation was represented by the tabulated data, which was consistent with the immediate proximity of the vacancy, and the three silicon atoms involved in the reconstruction.

It was therefore expected that there would be displacements in both the [0001] and $[000\bar{1}]$ directions, ranging over only slightly less than 1 Å in both the faces. Table 5.3 presents the results of a statistical analysis of the silicon atom locations adjacent to the first oxygen layer. For each face, the displacement in the [0001]-direction was calculated, relative to the location of the comparable atom in the defect-free slab. The z coordinate for Si atoms had a wider range of 0.06 Å, respectively, for the h and k faces.

Defect	Range	SD(z)
V_{C}^{kf}	0.840	0.07
V_{C}^{hf}	0.880	0.04

Table 5.3: Range and standard deviation (SD) for the Si-face displacements of the Si atoms in the SiC bonded to the first layer of the SiO_2 as a function of the vacancy location. All values in the table are in Å.

5.3.3.2 Migration barrier non-equivalent at both sites

The diffusion process for the carbon vacancy at the interface between 4H-SiC and SiO_2 was simulated, based on the NEB simulations, [60, 61] (see section 3.2.5). The migration of the carbon vacancy through the SiC lattice was simulated as a direct movement of the same atom type (either h or k) from a neighbouring site. Vacancies in the first C-layers for both the faces h-face and k-face are denoted as V_{C}^{hf} and V_{C}^{kf} respectively. The blue curve in the figure 5.5 shows profiles for the diffusion of the V_{C}^{kf} in the k-face. The diffusion pathway of the V_{C} in both the faces was observed as being independent to the faces.

The migration energy barrier for the current simulations was found to be 3.82 eV for the h-face and 3.84 eV for the k-face. In contrast, as presented in the chapter 4 the energy barriers of V_{C} in the 4H-SiC bulk were calculated to be 3.33 eV and 3.34 eV for the h- and k-sites, respectively, which was found to be higher by 15% for both the faces. It can be further concluded that the energy barrier increase resulting from the relaxation effect at the interface can serve as a source of the additional energy required for the diffusion process [99]. More details on the diffusion process are presented in chapter 6. Based on the diffusion and geometric studies, it was further concluded that the (0001)-interface between 4H-SiC and SiO$_2$ can be constituted of as a layer of Si-face at the k-face.

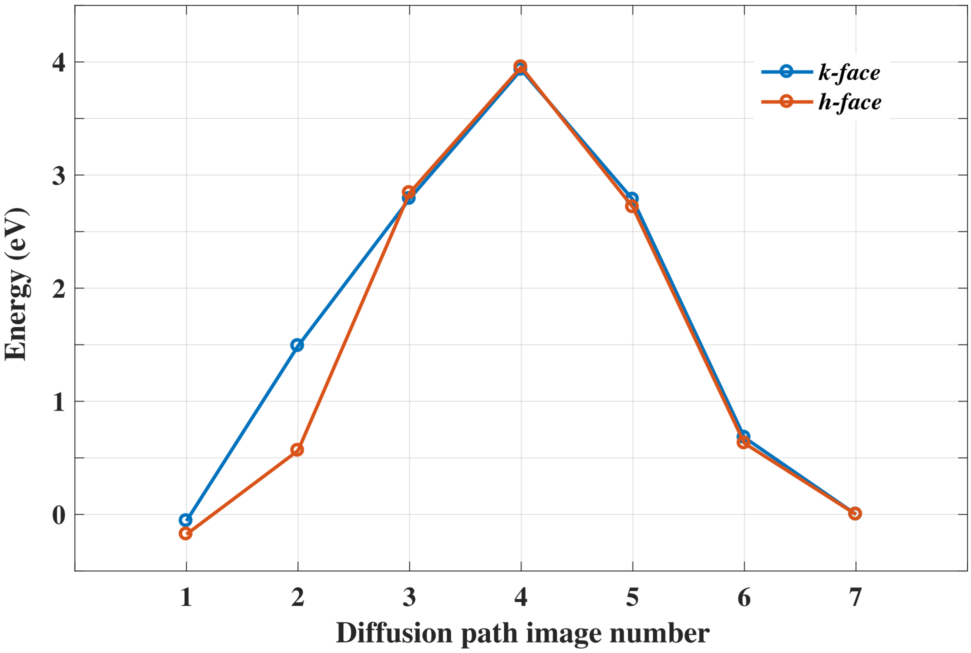

Figure 5.5: Calculated diffusion barrier using the cNEB method for the carbon vacancy defect in both the k-face and h-face at the SiO$_2$/(0001)4H-SiC. V_{C} position in the first layer at the interface.

5.3.3.3 Activation energy of the V_{C} with the slab thickness

Activation energy convergence is an important criterion to fix the model's structure. Based on the conclusions derived in the previous sections, the SiO_2/(0001)4H-SiC at the *k*-site was considered a good model structure, and could be tested for the activation energy convergence. The energy of the reaction energy was investigated and is presented in the table 5.4, which shows the total energy difference of the V_{C} in each layer according to slab thickness variation. Vacancies at the C-layers alongside increasing distance from the interface are denoted as V_{C}^1, V_{C}^2, V_{C}^3 and V_{C}^4. For this study, layers one and three were positioned at the *h*-site, while the layers two and four were located at the *k*-site. Calculations were carried out for three different slab thickness: 204, 232 and 332 respectively.

The 204-slab had previously been tested provided an accurate description of V_{C} at the interface (including the 128 Si and C-layer), and could be selected with only two first layers to introduce the V_{C} defect. Calculations show that for the V_{C_1} defect, the difference in the total energy between two carbon atoms (V_{C_1} with the next carbon-neighbour in the *z*-direction) in the first to second layer was only 0.27 eV higher than the corresponding energy between the *h*- and *k*-sites in the bulk 4H-SiC (as previously obtained in chapter 4). However, the same investigation, when conducted on the second to third layers, for V_{C_2} a difference of 0.06 eV lower than that in the top layer was found, and therefore was higher in comparison with the bulk. The energy values remained almost constant when the number of 4H-SiC slabs were increased, and thus, it was concluded that the energy was independent of the slab thickness. It is further noted that for the 268-slab in the, a smaller value of carbon vacancy difference was obtained in two non-equivalent sites on the 4H-SiC bulk.

Figure 5.6 shows the diffusion energy profiles between the neighbouring sites in a basal plane for the first layer as a function of slab thickness for each of the interface slab.These profiles were compared, together with the bulk 4H-SiC slab (dotted purple line). The diffusion profiles for the 204, 268 and 332 atoms slabs are seen to be converge with the slab thickness. Based on these investigations, it can be concluded that the slab thickness have an insignificant impact upon both the shape and the magnitude of the energy barrier.

No. layers	Vacancy positions	ΔE
	203	
1	$V_{\mathrm{C_{hh}}}$	0.279
2	$V_{\mathrm{C_{kk}}}$	0.061
	267	
1	$V_{\mathrm{C_{hh}}}$	0.285
2	$V_{\mathrm{C_{kk}}}$	0.055
3	$V_{\mathrm{C_{hh}}}$	0.027
	331	
1	$V_{\mathrm{C_{hh}}}$	0.284
2	$V_{\mathrm{C_{kk}}}$	0.055
3	$V_{\mathrm{C_{hh}}}$	0.025
4	$V_{\mathrm{C_{kk}}}$	0.013

Table 5.4: The effect of slab thickness (number of Si-C layers) on the total energy difference of V_{C} between two neighbouring sites of carbon layers in the vicinity of a SiO$_2$/(0001)4H-SiC interface interface, as indicated in the figure 5.4, ($V_{\mathrm{C_{ii}}}$ indicate the vacancies in the ii layer (odd layers are *h*-site and even *k*- site).

5.4 Chapter Summary

Understanding the nature of carbon defects represents is key to the devising of strategies to improve the functionality of semiconductor SiC devices functionality. This chapter aimed to simulate (using AIMpro software) and determine a model structure system for the SiO$_2$/(0001)4H-SiC interface, for use in future studies on carbon vacancy research (chapter 6) and carbon interstitial defect studies (chapter 7).

The model system is defined as a system that can be simulated consistently, with invariant results, and with the least computational requirements. Slab thickness is one of the main parameters that may vary. Furthermore, a comparative study of the diffusion of carbon vacancies at the *h*- and *k*-(0001) faces of the SiO$_2$/(0001)4H-SiC interface was conducted. Calculations showed no significant difference between these interfaces, but a diffusion energy was found to be greater by 15%, compared to that in the bulk 4H-SiC

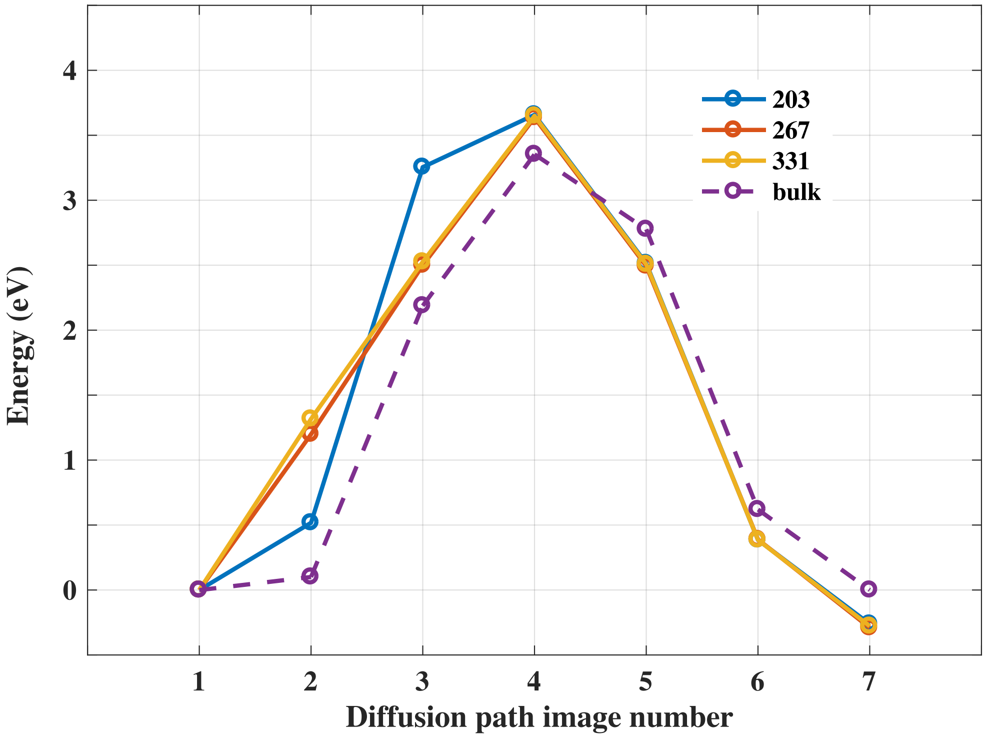

Figure 5.6: Minimum energy paths for the V_C are in the interface, while the blue, orange and yellow lines show the diffusion pathway profiles for slabs containing 203, 267 and 331 atoms, respectively. The dotted purple line represents the high barrier of bulk 4H-SiC.

structures. It is , however, not clear whether a carbon vacancy, as it moves into the deeper interfacial layers, will stabilise or not. In the next chapter, details of the geometry and electronic structure of the vacancy (as it moves in the interfacial layer) will be provided.

Chapter 6

Analysis of V_C at the SiO$_2$/(0001)4H-SiC interface

6.1 Introduction

As discussed in chapter 1, the surplus C-atom, produced at the SiO$_2$/SiC interface during the formation of SiO$_2$, can be diffused into the 4H-SiC, annihilating the pre-existing V_C. This will lead to the observed reduction of DLTS centres [2]. Furthermore, these defects are believed to be the origin of the high interface trap density in the bandgap, which subsequently resulted in charge trapping and Coulomb scattering at the interface [17].

It is understood from existing literature studies that the origins of the interface defects at the transition layer between SiO$_2$ and 4H-SiC remains a matter of debate, particularly regarding the existence of an Si-O-C interlayer [100]. The real point of contention is whether there exists a thin interlayer with increased carbon concentration between the interface layer, and on the either side of the 4H-SiC bulk slab or SiO$_2$ slab. Previously conducted HRTEM and EELS analyses have lead researchers to conclude that on either side (a) the existence of the interlayer or (b) refuted it and establish an abrupt transition from the interface and bulk slabs. Layer thickness is shown to be proportional to the SiC/SiO$_2$ consumed during the oxidation process. A contrary conclusion is provided by Pippel *et al.*, that is, the HRTEM and EELS analysis conducted by the group revealed no such layer, and found a rather abrupt SiC/SiO$_2$ transition, with no excess carbon clusters or layer formations [101]. The claim of an abrupt interface is further supported by Hatakeyama *et al.* [102], regardless of oxidation conditions and/or crystal orientation. It was further concluded that the defects exist intrinsically in the SiC/SiO$_2$ interface layer, rather than being situated in the transition layer. A similar conclusion was reached by X-ray photoelectron spectroscopy studies conducted by Ekoué *et al.*, where no transition layer or carbon clustering was observed following a reduction in Si bond angle by 30% [103], after re-oxidation. This chapter is based on this leading hypothesis.

Previous atomistic simulations [76] of the SiO$_2$/4H-SiC interface have explored the energy levels of different configurations of carbon-related defects. In one of the carbon related defects, the carbon vacancy at SiO$_2$/4H-SiC interface accommodated 2(O)-atoms to form a V_C O$_2$ defect. However, one of the O-atoms replaced carbon and linked with the four Si neighbours, while the remaining oxygen buckled out toward the oxide phase. PAS (positron annihilation spectroscopy) studies by [76] previously experimentally reported this defect, and concluded this was similar to the A centre V_O defect in Si, but electrically inactive. However, Pippel *et al.* contradicted this, and explaining that the regions near the SiO$_2$/4H-SiC were expected to be electrically active, and could have given rise to the interface states observed [38]. Furthermore, [76] lacks an important discussion regarding the properties of the structure for individual V_C defect.

A model system and the parameters for studying the V_C in bulk 4H-SiC were established and reviewed in the previous chapter of this study (section 4.3.1.1). The model structure provided a basis for the information in chapter 5 on the diffusion at the SiO$_2$/4H-SiC interface. It was concluded that the SiO$_2$/4H-SiC interface is hindered, with the overall activation energy being roughly 0.5 eV (15%) higher than the corresponding migration barrier of this native defect in bulk 4H-SiC. In this chapter, the carbon vacancy defects will be studied and will be computationally created at the SiO$_2$/4H-SiC interface (refer to chapter 5). This modelling approach enables capturing the specific interface related effects, including the structural relaxation, the bonding rearrangement and the electronic structure of the vacancy as it moves in the interfacial layer.

Based on this modelling work, the origins of the dependence of the activation energy upon proximity to the SiO$_2$/4H-SiC interface will be explained in terms of stabilisation of the vacancy in the immediate interface and an increase in the transition state energy. Furthermore, the carbon vacancy at the C-layers become increasingly distant from the interface of V_C from the SiO_2/(0001)-4H-SiC interface, parallel to the interfacial plane (as shown in figure 6.1) would be simulated and studied in detail in this chapter. Finally, three types of structural relaxation upon the non-equivalent site at the interface will be investigated, and the first, second, and third position are referred to V_C^1, V_C^2 and V_C^3. This chapter's results and discussion are associated are the work published here [99].

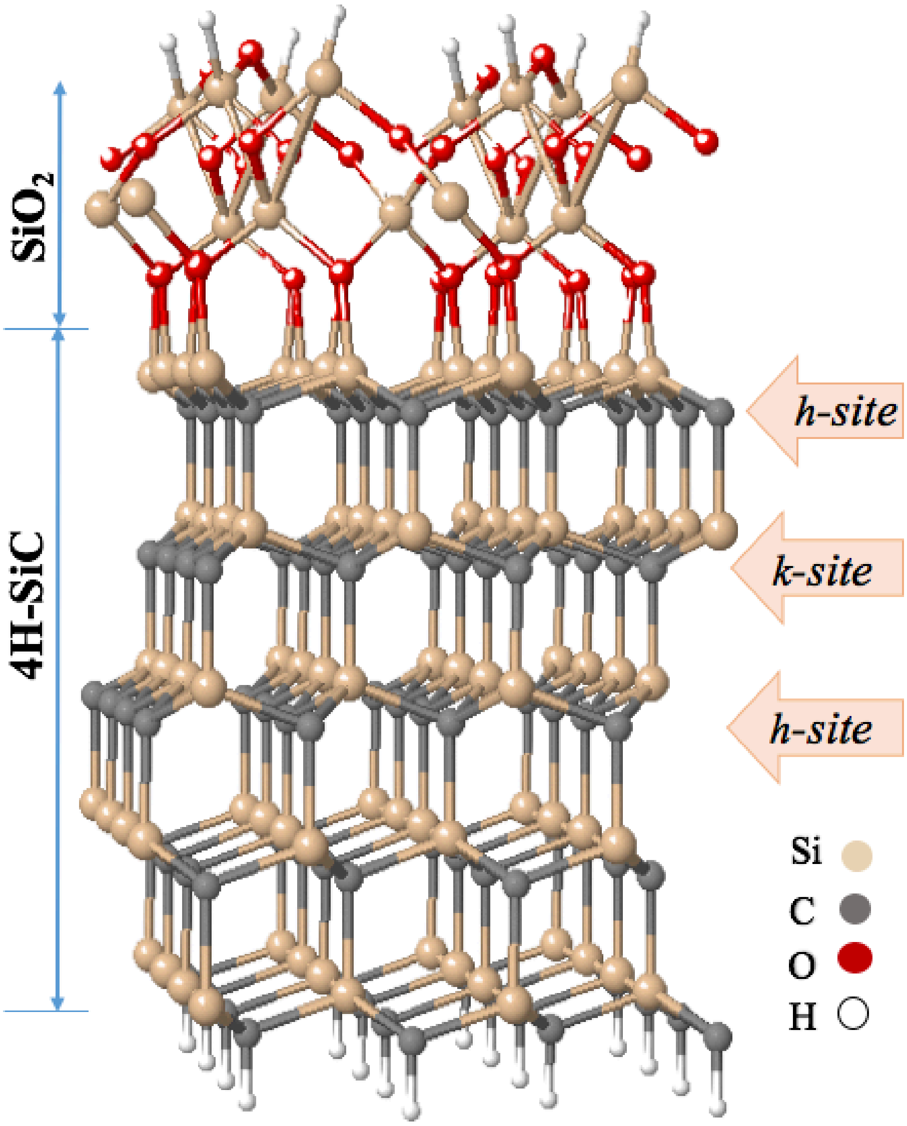

Figure 6.1: schematic of the SiO_2/(0001)-4H-SiC interface structure used for this study: white, red, grey, and yellow, and white spheres are H, O, C and Si respectively. The numbers within the arrows indicate the layer number.

6.2 Computational Method

This chapter studies carbon vacancy defects in the deeper region of the interfaces. To this end, the SiO$_2$/(0001) 4H-SiC system was simulated using the slab-geometry approach (details in section 5.3.2). Carbon vacancy can be simulated by computationally removing any of the C-atoms in the structure.

In order to study the effect of layers at which carbon defects occur, removal can be simulated using any of the three C-layers, according to an increasing distance from the interface. The nature of the vacancy is also explored based on whether the vacancy is initially located at an *h*-site (odd-numbered layers) or a *k*-site (even-numbered layers), as shown in figure 6.1.

All calculations were carried out using the density functional technique, as implemented in AIMpro (described in chapter 2 and chapter 3) including the basis set (see section 3.1.3, band structure, and electrical levels, which were estimated by calculating formation energy (see section 3.2.3) and the diffusion processes of V_{C} (section 3.2.5). The same computational approach was deployed to model the SiO2/4H-SiC(0001) system.

6.3 Results and discussion

6.3.1 Modelling structures of V_{C} at the SiO$_2$/4H-SiC interface

Table 6.1 presents a comparison of the carbon vacancy at the interfaces against the V_{C} in the bulk 4H-SiC at the cubic and hexagonal lattice sites in the neutral charge states. The corresponding values of the V_{C}^{h} and V_{C}^{k} were based on the computational study of 4H-SiC bulk presented in the chapter 4.

In order to study the geometrical structures of V_{C} as in section 4.3.1.1, the following sections provide more details of the defects in each layer.

6.3.1.1 V_{C} in the first layer

The carbon vacancy in the first layer was simulated by removing one carbon atom from the topmost layer (*h*-site of the 4H-SiC slab). Many possible sites have been tested to investigate the V_{C} structure at the interface shown in figure 6.3, with values presented in

Position of V_C	$d1$	$d2$	$d3$	$d4$	$d5$	$d6$
V_C^1	-13	+2	-1	+2	+8	-11
V_C^3	-8	-1	0	+3	+2	-10
V_C^h	-9	+1	0	+2	+2	-10
V_C^2	-12	-1	0	+2	+3	-8
V_C^k	-12	-1	+1	+1	+2	-9

Table 6.1: Relaxation around the V_C in 4H-SiC given in (%), compared to the ideal tetrahedral distance between NN silicon atoms V_C. Distances $d1$–$d6$ are labelled according to figure 6.2. These values indicate how much each of the the other sites were higher (positive) or lower (negative), relative to the Si–C distance in pure 4H-SiC (3.06 Å) in our computational approach).

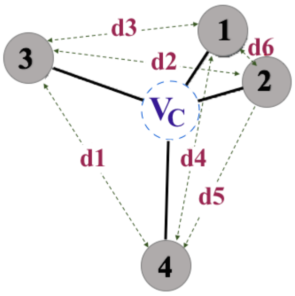

Figure 6.2: Schematic atomic tetrahedron structure of SiC indicating the distances of NN atoms around d1–d6 are used in tables 6.1.

table 6.2. Labels (1–9) indicate non-equivalent sites examined within the interface. On the carbon vacancy at the first layer, it was found that the different energies associated with the carbon vacancy defect, as per the labels 1 and 2 ($V_{\mathrm{C}_{12}}$), and between 2 and 3 ($V_{\mathrm{C}_{23}}$), were situated at 0.27 eV and 0.14 eV, respectively, which is higher in energy than the other sites. These findings can be employed to indicate that the geometric properties of the V_C at this layer was also investigated. Calculations from the simulations showed that the displacement of the parallel Si atoms around the defect was lower, due to the presence of the nearby $\mathrm{SiO_2}$ layer. The results also show that a pronounced movement of two Si atoms towards each other was observed and led to the formation of Si-Si covalent bonds (discussed in section 4.3.1.1). It is further noted that the Si-Si bonds formed (2.77 Å and 2.76 Å) were shorter than the inter-nuclear separation of nearest silicon neighbours in SiC (3.07 Å)and 2.76 Å. Furthermore, the Si reconstruction of the dangling bond formed a defect level state in the band-gap (see figure 6.5).

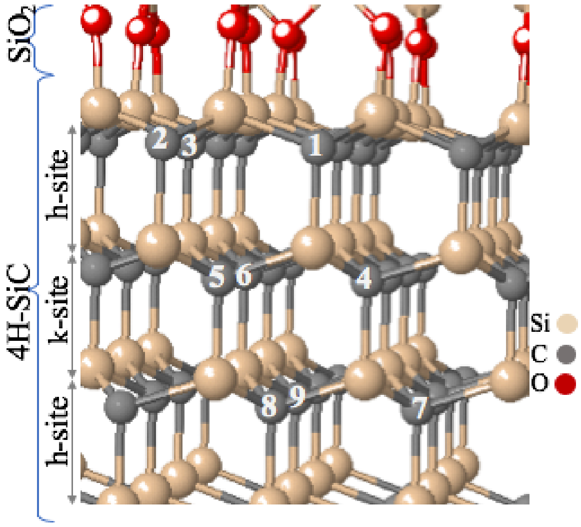

Figure 6.3: Projection of optimised structures of the at the SiO_2/4H-SiC interface. Labels 1-7 indicate the V_C sites investigated.

	Position of V_C	$\triangle E$
layer(1)	$V_{C_{12}}$	0.27
	$V_{C_{23}}$	0.14
layer(2)	$V_{C_{45}}$	0.04
	$V_{C_{56}}$	0.05
layer(3)	$V_{C_{78}}$	0.02
	$V_{C_{89}}$	0.01

Table 6.2: The energy differences $\triangle E$ in (eV) associated with the different sites of V_C.The position of V_C as examined for the sites are illustrated in figure 6.3

The evidence for the impact of relaxation of the equilibrium carbon vacancy structure at the first layer at the interface was observed in the electronic structure (figure 6.5-a). A single occupied state, which was related to Si-Si bonds reconstructions, derived derived from a splitting of the three-fold-degenerate state of the unreconstructed structure V_{C}^{h*} (figure 6.5a). This occupied state was showed an anti-bonding combination of orbitals from the two Si-Si covalent reconstructed bonds [99], as illustrated in figure 6.5. The band structures of V_{C}^{1} (vacancy at the interface) and V_{C}^{h} (at bulk 4H-SiC) show that the highest occupied band was located at to the valence band for the V_{C}^{h}.

On the other hand, the structure around a defect in the amorphous $\mathrm{SiO_2}$ oxide relaxed much more easily and an anti-bond stabilising the system was accommodated [104]. This is probably a consequence of the weak interaction between Si-Si bonds that can result in a small difference by roughly 0.2 eV (see figure 6.5) compared to the unrelaxed structure.

The second observation indicates that, the chemical nature of the atoms also, has an impact on the splitting between occupied and unoccupied levels. This means that, for an unrelaxed structure, the carbon vacancy in the first layer forming a Si-Si bonding level is located at the top of the valence band (see figure 6.5-b). This level moves into the band gap for stronger reconstracaion Si–Si bonds, and as a result, the anti-bonding level remains in CB near the edge (see figure 6.5-c), causing a large separation between the occupied and unoccupied levels, as indicated in [99].

As discussed in the previous sections, this occupied gap-state is dominated by an anti-bonding combination of orbitals from the two Si–Si covalent reconstructed bonds (figure 6.6). Comparing the band structures of V_{C}^{h} and V_{C}^{1} shows that the highest occupied band is closer to the valence band for the vacancy at the $\mathrm{SiO_2}$/4H-SiC interface which is consistent with the strengthening of the reconstructed bonds.

6.3.1.2 V_{C} in the second layer

Based on the figure 6.3 and the values presented in the table 6.2, it was found that with the carbon vacancy in the second layer, the difference in associated energy as per labels 4 and 5 ($V_{\mathrm{C}_{45}}$), was 0.04 eV, whereas the difference in energy between 5 and 6 ($V_{\mathrm{C}_{45}}$) was 0.05 eV. This confirms the environment of V_{C}^{1} then site V_{C}^{2}, which can be considered as being relatively a uneffected by the oxide layer.

The schematic of V_{C} in the second layer is shown schematically in figure 6.7, in which

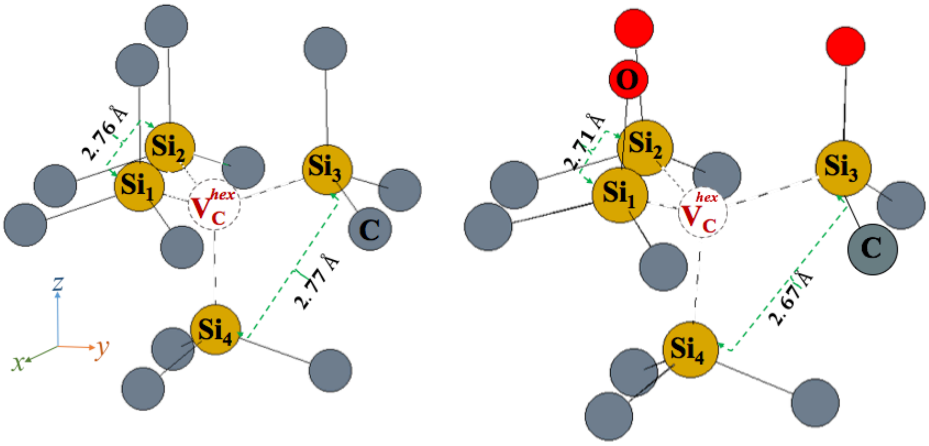

Figure 6.4: Atomic structure indicating the local arrangement of the V_{C} labelling reconstructed Si–Si bond-lengths (Å) for V_{C} in bulk 4H-SiC and in the first carbon layers in the vicinity of a SiO$_2$/(0001)-4H-SiC interface, C, O and Si atoms are shown in grey, red and yellow respectively.

is compered with the schematic in bulk SiC. It can be seen that the bond length for the Si atom pair in the second layer at the k-sites (2.81 Å) was greater than the Si-Si bond length, due to the carbon vacancy at the bulk. This is related to the nearest silicon neighbours in the basal plane which is linked directly with the Si interface (2.77 Å). A decrease in the bond length related to the Si–Si pair in the c-axis (2.67 Å),which is slightly higher compared with V_{C}^{k} (2.68 Å and 2.77 Å), was also reported (in line with the finding in chapter 4). The main structural parameters of the relaxed defect models are summarised in table 6.1.

It can be further observed from the electronic structure of V_{C}^{2} (figure 6.8) that the locations of the occupied band for V_{C}^{2} and V_{C}^{k} were very similar. Therefore, this result shows that, a qualitative investigation of band structures between two vacancy defects was similar, while quantitatively. The data for V_{C} in the second layer are smaller than for V_{C} in the first layer, so that despite the relatively less favourably reconstruction. The relaxation at the interface provides a stabilising effect resulting in a lower energy thanV_{C} in bulk, reinforcing the role of the interfacial relaxation in the stabilisation of V_{C} in the second layer [99].

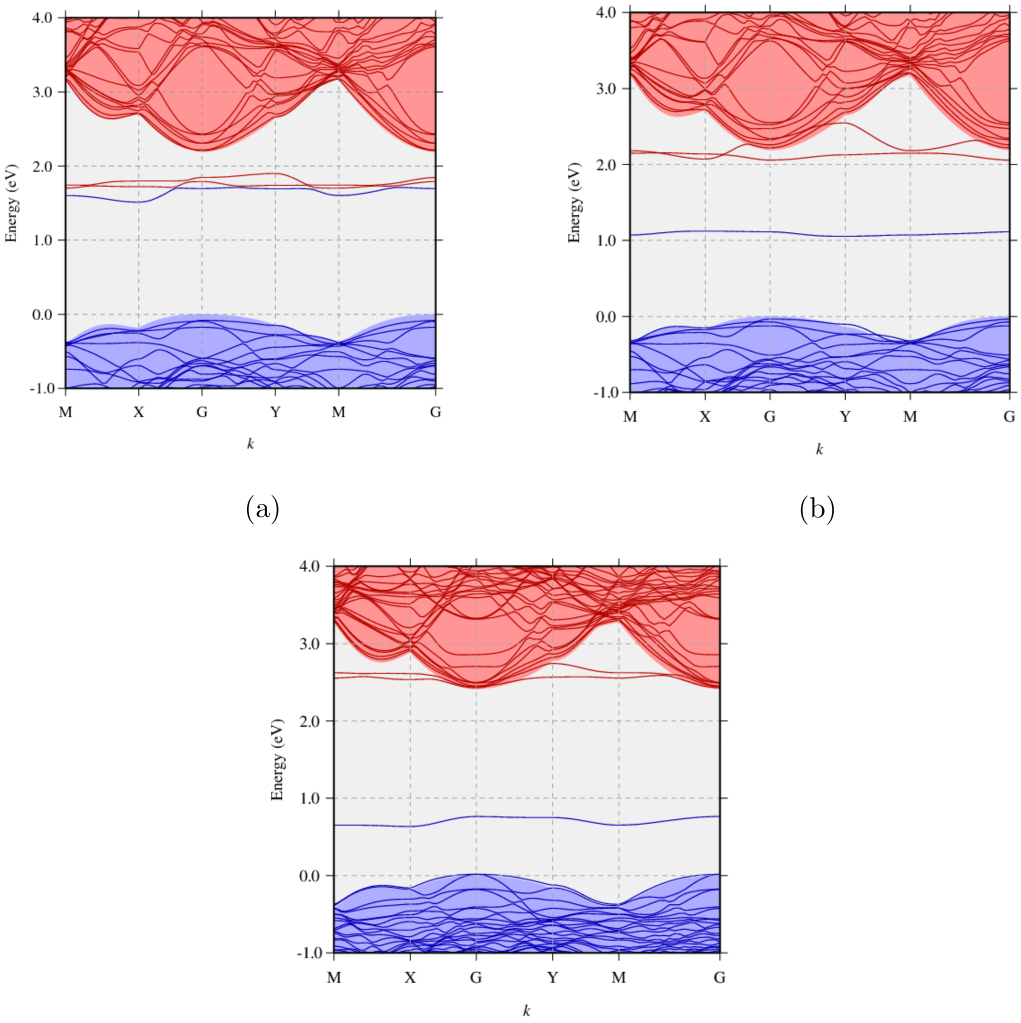

(a)

(b)

(c)

Figure 6.5: Electronic band structures of V_{C} bulk 4H-SiC and at the $\mathrm{SiO_2}$/4H-SiC interface slab: (a) V_{C}^{h*} , (b)V_{C}^{h}, and (C) V_{C}^{1}. Occupied and unoccupied states are depicted as solid blue and red lines respectively, with the envelope of the band-structure for the corresponding defect-free case shown by the underlying shading.The underlying shaded regions show the electronic band structure for the corresponding bulk 4H-SiC (128-atoms) and interface (268-atoms) The energy scale is defined such that the valence band maxima are at zero. Only states in the region of the band-gap are plotted.

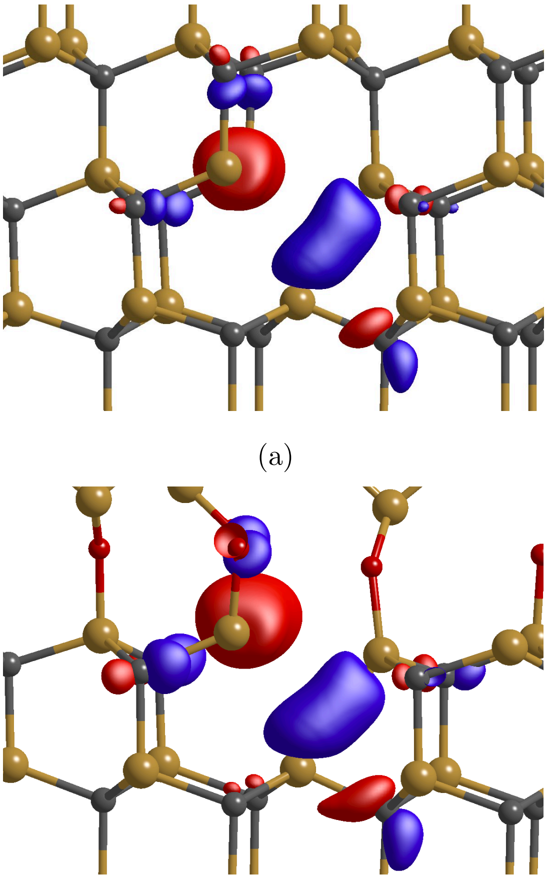

(a)

(b)

Figure 6.6: Schematics showing wave function isosurfaces for the highest occupied bands of V_{C}^{h} and V_{C}^{1} (figure 6.5). Red and blue isosurfaces represent positive and negative wave function components, respectively. Yellow, grey and red atoms, are Si, C and O, respectively. The horizontal direction is approximately along $[1\bar{1}00]$, and the vertically upward direction is [0001].

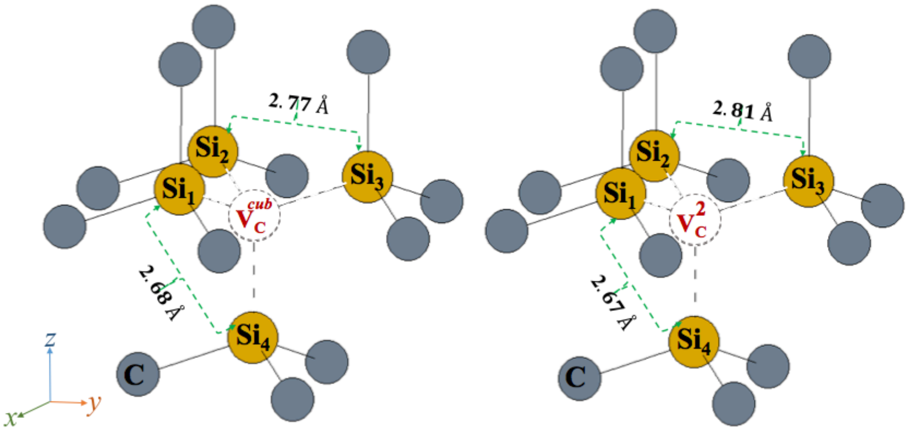

Figure 6.7: Reconstructed Si–Si bond-lengths (Å) for V_{C} in bulk 4H-SiC and in the first carbon layers in the vicinity of a SiO_2/(0001)-4H-SiC interface

6.3.1.3 V_{C} in the third layer

Based on figure 6.3 and the values presented in table 6.2, it was found in the V_{C}^3 at the third layer, that the difference in total energies between 7 and 8 ($V_{\mathrm{C}_{78}}$), ($V_{\mathrm{C}_{89}}$) lie at 0.02 eV and 0.01 eV, respectively. The defect in this layer was reasonably matched to the results obtained from the 4H-SiC bulk. Confirming this result by investigating geometrical structures, the result of the differences between the V_{C}^3 (at the interface) and V_{C}^h (in bulk), showed that the neighbouring pairs interacted had weaker interaction than those in the first layer. In particular, calculations show that the change in the distances of the next neighbours of Si atoms was unchanged from their distances in the 4H-SiC bulk, as shown in table 6.1. It is concluded that V_{C}^3 bonds behave like those in the bulk system and relaxation around defects at this site tends to be similar corresponding to pure 4H-SiC. It can be further observed from the electronic structure of the V_{C}^3 defect (figure 6.10) that a weak interaction between Si-Si bound results in a similar energy level state corresponding with the bulk 4H-SiC (see section 4.3.1.1). This presents a reference for the diffusion calculations that will be presented later in this chapter.

Table 6.3 lists a statistical analysis of the locations of the Si-atoms adjacent to the first O-atoms layer. For V_{C}^1 the deformation represented by the tabulated data is consistent with the immediate proximity of the vacancy and three of the Si atoms analysed are involved in the reconstruction. Therefore there are displacements in both the [0001] and

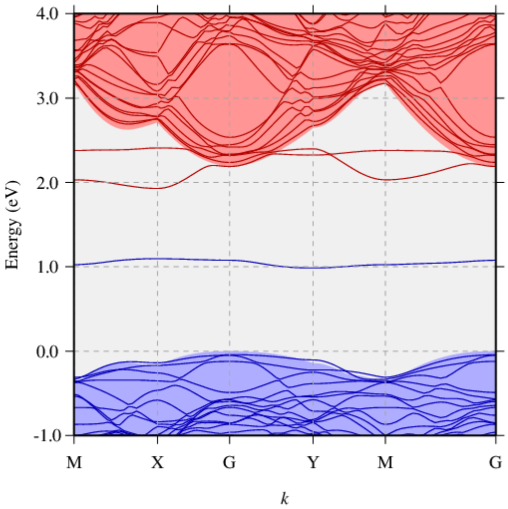

(a)

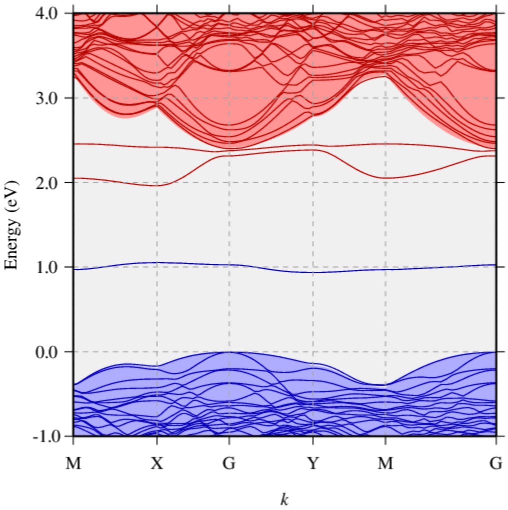

(b)

Figure 6.8: Electronic band structures of V_{C} bulk 4H-SiC and at three sites in the SiO$_2$/4H-SiC interface slab: (a) V_{C}^{k}, (b) V_{C}^{2}. Occupied and unoccupied states are depicted as solid blue and red lines respectively, with the envelope of the band-structure for the corresponding defect-free case shown by the underlying shading. The energy scale is defined such that the valence band maxima are at zero. Only states in the region of the band-gap are plotted.

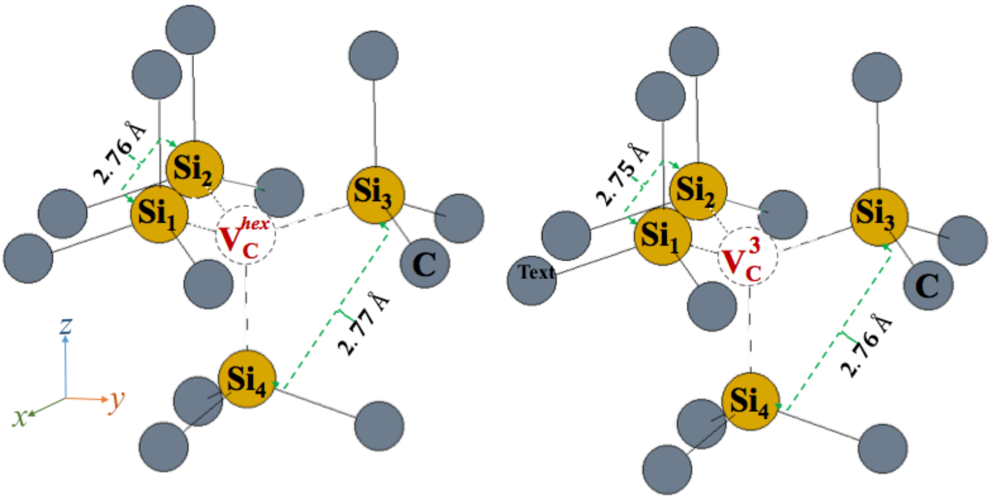

Figure 6.9: Reconstructed Si–Si bond-lengths (Å) for V_C in bulk 4H-SiC and in the third carbon layers in the vicinity of a SiO_2/(0001)-4H-SiC interface

V_C Position	Range	SD(z)
layer (1)	0.840	0.161
layer (2)	0.213	0.053
layer (3)	0.084	0.026

Table 6.3: Range and standard deviation (SD) of the Si- atoms in the [0001] displacements in the SiC bonded to oxygen in the SiO_2 as a function of the position of the V_C, all values in Å

.

[0001?] directions, ranging over slightly less than 1 Å. This result confirms that the carbon vacancy defect at the second layer was smaller than for the first layer but greater than for V_C^3 [99].

The defect observed was more stable than in the bulk, but the question as to how V_C behaved during the process, such as an annealing process, remains largely unanswered. However, the initial results of the migration process were obtained (according to the total energy of defect in each layer at the interface) and the next section will provide more detail in the diffusion process of those defects at the interface.

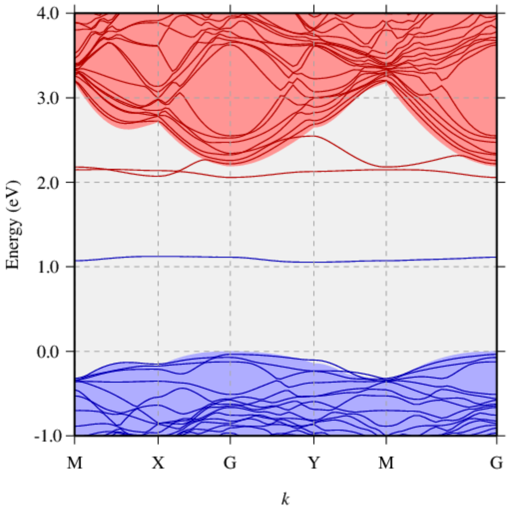

(a)

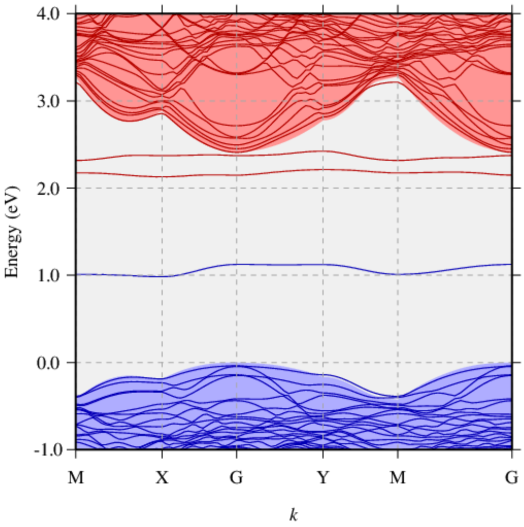

(b)

Figure 6.10: Electronic band structures of V_C bulk 4H-SiC and at three sites in the SiO$_2$/4H-SiC interface slab: (a)V_C^h, (b)V_C^3. Occupied and unoccupied states are depicted as solid blue and red lines respectively, with the envelope of the band-structure for the corresponding defect-free case shown by the underlying shading. The energy scale is defined such that the valence band maxima are at zero. Only states in the region of the band-gap are plotted.

6.3.2 Diffusion of V_C through the SiO_2/4H-SiC interface layers

6.3.2.1 Single hop for V_C at parallel direction

In 4H-SiC, migration could be within the same layer (*hh* or *kk*) or in a perpendicular direction (*hk* or *kh*). In this section, we study the diffusion of carbon vacancies by calculating the activation energies required for carbon vacancies to migrate between two sites (*h* to *h* at the first and third layers, or *k* to *k* at the second layer and the third path diffusion from the first to second layer, as *k* to *h*).

Parallel migration of V_C within the same C-layer, V_{C1} and V_{C2} can be followed as: the C1 atom is removed and moves to the next nearest neighbour C2. Similarly, migration for 2NN happens as $V_{C2} \rightarrow V_{C3}$ (figure 6.3). Perpendicular migration of V_C along the *c*-axis (from the first to the second layer in SiC slab) is described as: $V_{C1} \rightarrow V_{C4}$. Several possible reaction pathways have been tested to investigate the migration barrier of V_C at the SiO_2/4H-SiC interface.

The magnitude of the diffusion barrier in the interface was found to be higher in comparison to the bulk process (figure 6.11). A higher barrier can arise from changes in the energy of (i) the equilibrium structures, (ii) the saddle-point or (iii) a combination of (i) and (ii). The diffusion energy profiles was calculated to resolve the origin of the increased barrier in the SiO_2/SiC interface.

These results have been compared with those for the bulk 4H-SiC, as shown in figure 6.3. Two cases were investigated in each layer: firstly, when a carbon vacancy moved to its next neighbour (2NN) in the direction $(V_{C1})\rightarrow(V_{C2})$, second, when V_C diffused into the next carbon in the next row $(V_{C2})\rightarrow(V_{C3})$. The calculated data for the activation energy SiO_2 for each of these two possible migration routes is listed in table 6.4. It should be noted that the barriers calculated using the interfacial slab were slightly dependent on the pairs of sites between which the diffusion took place, due to the symmetry lowering the effect of the SiO_2 layer [80].

The diffusion parallel to the modelled interfaces was between *k*-site (*kk*) in the second layer at the interface. This means the creation of V_C occurred by removing the C-atom in the second layer at the interface. The energy barrier of diffusion was examined, yielding 3.8 eV, which was higher than the corresponding barrier in the bulk 4H-SiC, by 0.40 eV (figure 6.11). This is probably a consequence of the the strengthening of the reconstructed f

Position of V_{C}	Migration pathway	E_B (eV)	$\triangle E$
Diffusion pathway in basel plane			
1	$(V_{\mathrm{C1}}) \rightarrow (V_{\mathrm{C2}})$	3.82	0.49
	$(V_{\mathrm{C2}}) \rightarrow (V_{\mathrm{C3}})$	3.83	0.51
2	$(V_{\mathrm{C4}}) \rightarrow (V_{\mathrm{C5}})$	3.75	0.40
	$(V_{\mathrm{C5}}) \rightarrow (V_{\mathrm{C6}})$	3.76	0.42
3	$(V_{\mathrm{C7}}) \rightarrow (V_{\mathrm{C8}})$	3.43	0.1
	$(V_{\mathrm{C8}}) \rightarrow (V_{\mathrm{C9}})$	3.37	0.04
Diffusion pathway along c-axis			
$1 \rightarrow 2$	$(V_{\mathrm{C1}}) \rightarrow (V_{\mathrm{C4}})$	4.08	0.20
$2 \rightarrow 3$	$(V_{\mathrm{C4}}) \rightarrow (V_{\mathrm{C7}})$	3.95	0.05

Table 6.4: Possible migration pathways for single V_{C}. The activation energy differences $\triangle E$ in (eV) associated with the different sites of V_{C} in the bulk. These values indicate how much each of the other sites is higher than the reference (in both both h-site and k-site in bulk 4H-SiC). The position of V_{C} as examined for the sites is illustrated in figure 6.3

bonds of V_{C}^2 bonds in this layer. Then, the distance required for the C-atom to move in the diffusion process is greater. Although the paths are symmetrically distinct, the saddle points are not.

Another point is that the barriers are higher in the first layer than in the third, with the former showing a general reduction of 0.1–0.2 eV. This arises from delocalised structural distortion stabilised by the presence of the vacancy. For a clear picture of the variation, the energy of V_{C} is larger than that of the initial structure by 0.22 eV, suggesting that the reaction is endothermic. However, it is noted that this activation energy is somewhat higher than the activation energy for the equivalent path in bulk 4H-SiC, which was calculated to be around 3.3 eV. Moreover, the activation energy in the third layer resembles the energy from bulk 4H-SiC, which can be considered as a reference for V_{C} in a bulk-like interface environment.

Figure 6.12 illustrates the transition state of the defect structure can be illustrated.

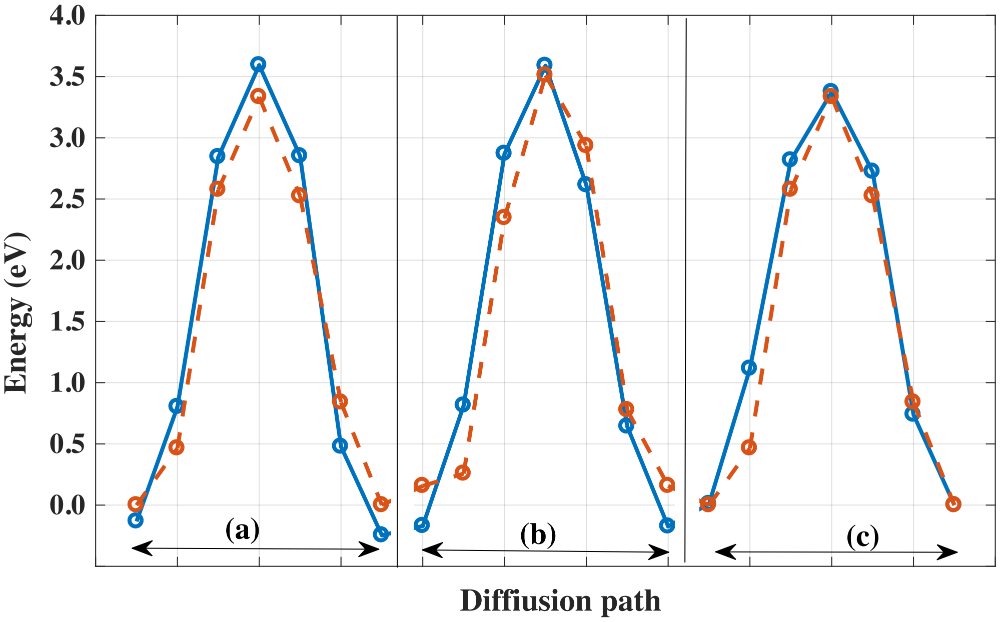

Figure 6.11: Minimum energy path energy profiles for three layers adjacent to the SiO_2/SiC interface (solid blue lines): (a) and (c) show *hh*-process (V_C^1 and V_C^3), and (b) shows the *kk*-process (V_C^2). In each case the underlying red dashes show the energy profile for bulk 4H-SiC (dotted red lines). The energy scale is set to zero for V_C^h. Symbols show the energies obtained using the NEB method, with the lines joining them a guide to the eye.

During the diffusion process, a carbon atom is lying midway between two carbon sites during movement. This atom is bonded to three Si- atoms. One of the Si- neighbours is 3-fold-coordinated, while the other two Si-atoms are fully-coordinated. However, during the diffusion process, the Si-sites adjacent to the two different C-sites can be involved in this process. It can also three C-Si bonds (solid at the centre in figure 6.12), are shorter for V_C^1 than for V_C^h in bulk 4H-SiC. This is probably a consequence of the relatively easier relaxation of the SiO_2.

6.3.2.2 Single hop for V_C in the c-axis

We need to further examine whether the increase in energy was a consequence of the simulation system, rather than a physical effect arising from the proximity to the interface. Diffusion of V_C from the first layer to second layer along c-axis, $(V_{C1})\rightarrow(V_{C4})$, as shown

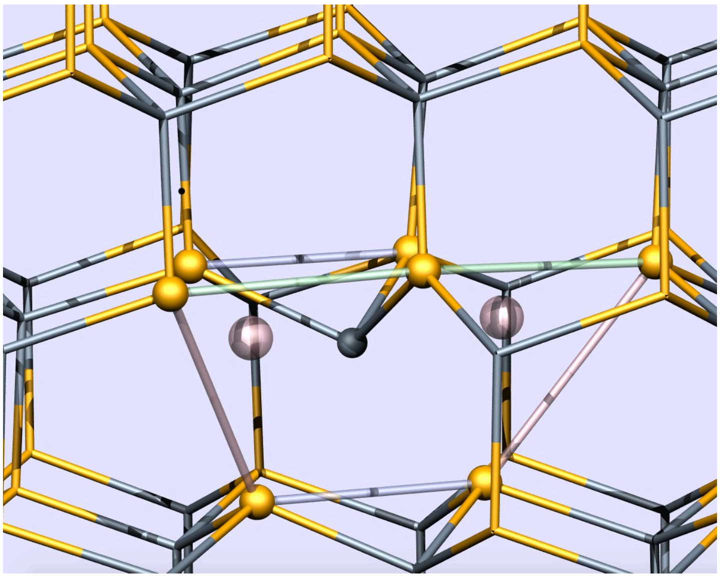

Figure 6.12: Schematic of V_{C} in 4H-SiC in the neutral charge state, the saddle point structure of of V_{C}^{h}. The yellow and grey sites are Si and C, respectively, with the translucent spheres indicating the carbon sites between which the C atom is moving. Si sites indicated with spheres are those adjacent to the vacancy at either end of the process.

in figure 6.3). The energy barrier was found 4.08 eV, while the vertical distances of the bond length Si$_4$ (the upmost Si-C bilayer) decreased (see table 6.4 diffusion pathway along c-axis). This effect is marginally sensitive when V_{C} moves from the second to the third layer at the interface because the effect of the SiO$_2$ layer is diminished. Thus, this position at the interface can be considered as a reference for V_{C} in a the 4H-SiC bulk as being relatively unperturbed by the oxide layer. It can therefore be concluded that from figure 6.3 the increased barriers between the first two carbon layers arise as a direct consequence of the interaction with the oxide.

The result indicates that the carbon vacancies position in layer 1 and 2 of the 4H-SiC slab (figure 6.11) can move from their next nearest neighbour by 0.6 eV, which is a higher-energy barrier than the diffusion barrier when the V_{C} lies at sites 3 and 4. Calculations of the migration barriers formed by V_{C} in the first and second layers show that they were higher in energy than the bulk reference, by roughly 0.5 eV. The data, therefore supported the idea that the V_{C} can move more freely within a basal- plane via the h-site or k-site than in the c-axis direction in the immediate interfacial layers, but that is hindered relative to the diffusion in the bulk. Further, although there is a significant impact on the parallel migration, the energy barrier of the carbon vacancy at each site ($V_{C4} \rightarrow V_{C7}$) in orthogonal directions are a good match for the energys barrier. The resulting of those barriers are plotted in figure 6.13.

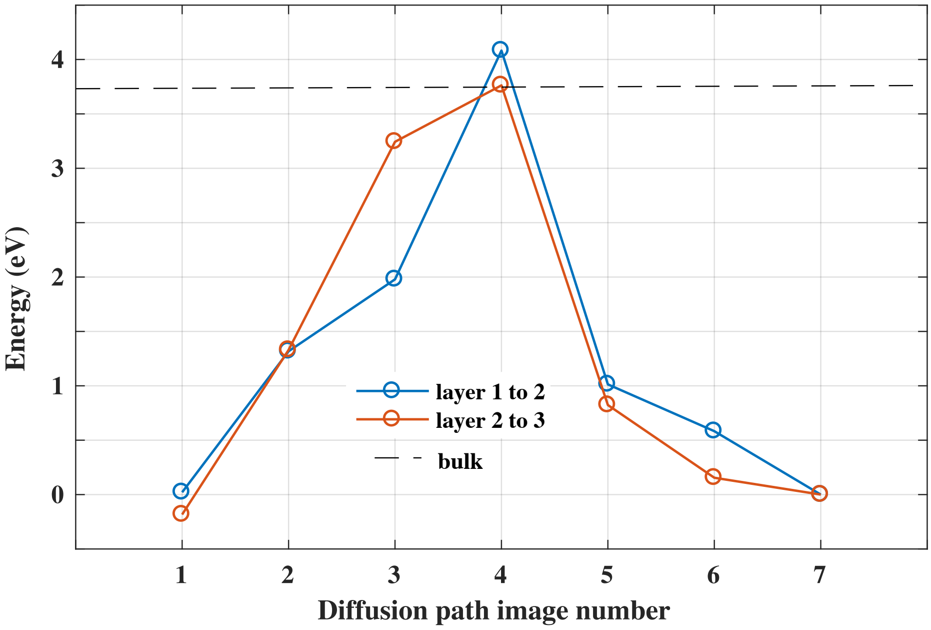

Figure 6.13: Calculated migration barrier of V_C moving between C-layers at the SiO_2/4H-SiC interface via *c*-axis direction. The first process present as the (V_{C1}) → (V_{C4}) in 4H-SiC slab, as illustrated in figure 6.3, while the seconed process; (V_{C4}) → (V_{C7}).The circles refers to the images used in the NEB calculations and The horizontal solid line indicates the diffusion of V_C in bulk 4H-SiC in same process.

This observation is supports the view that the environment beyond the first Si-C bilayer from the SiO_2/4H-SiC interface is very similar to the bulk SiC, and experimental evidence for this is reported in [101].. Additionally, the conclusion supports the notion that the mobility of V_C is lower in the vicinity of an interface with SiO_2 than in bulk, which is consistent with a high density of trap in this region, as supported by experimental findings [101].

6.4 Chapter Summary

In this chapter, an investigation was conducted into the stabilisation and diffusion processes of V_C within the SiC adjacent to the SiO$_2$/(0001)-4H-SiC interface, by means of DFT calculations, and implemented using the AIMpro software package. It was found that V_C can form stronger Si-Si reconstruction bonds in the interface layer, while the lowering of energy of band-gap states correlates with a lowering in the formation energy of the defect in this site. C-layer studies were reviewed to better understand the stabilisation of the vacancy. The more distant vacancy from the interface (third layer), that is similar to the activation energy profile was obtained for the *hh* process in bulk 4H-SiC. The findings of this chapter also found that if the vacancy lay more than two SiC bi-layers from the interface, its behaviour differed insignificantly from the equivalent bulk. In the case of diffusion mechanisms, the interfacial layer had a higher activation energy, due to the stabilisation of the vacancy and increased energy of the transition state. This is linked to the destabilisation of the reconstructions, and reduced the rate at which the vacancy was expected to migrate in the interface neighbourhood. Finally, it is noted that the findings of higher barriers and the stabilisation of vacancies at the SiO$_2$/4H-SiC interface were consistent with a high density of trap in this region, as noted in experimental observations [101].

Chapter 7

Carbon interstitials in the SiO_2/4H-SiC interface

7.1 Introduction

It has been established that the performance of semiconductor devices is negatively influenced by the presence of carbon interstitials [17]. Such regions near the SiO_2/SiC interface were expected to be electrically active and able to give rise to the interface states observed [40](as mentioned in chapter 1). The origins of carbon interstitials can be tracked by following the semiconductor manufacturing process, in which SiO_2 layers are formed by the oxidation process of SiC layers. The free carbon generated during the oxidation is incorporated into the growing SiO_2 layer as interstitials. Experimental evidence suggests that carbon interstitials have been reported to reduce DLTS centres [74], as well as resulting in additional deep-level defects (see section 4.3.2).

Supporting this idea, X-ray photoelectron spectroscopy (XPS) experiments have detected graphitic regions in the SiC layer prior to oxidation [101, 103]; however, during oxidation, these were dissolved, and it was further concluded that no graphite could be found at the SiC/SiO_2 interface [105]. Pippel *et al.* [38] reported to have found no large carbon clusters at the interface following a dry thermal oxidation process; however, the carbon interstitials can be expected to appear as carbon dimers, or native oxide traps [74].

The DFT calculations implemented via the AIMpro software were previously established in this thesis (chapter 5) as a validated numerical approach for studying the

SiO_2/4H-SiC(0001) interface. A model of the interface was previously described in chapter 5. In this chapter, DFT calculations are further employed to provide insights into the geometrical structure and the diffusion mechanisms of the interfacial defects at the SiO_2/SiC interface. In order to gain a deeper understanding of the carbon split-interstitials in the interface, the carbon interstitial defects in the bulk are used as a reference (see secation 4.3.2).

In the existing literature [76], an ab initio study of the SiO_2/4H-SiC interface explored the energy levels of different configurations of carbon-related defects. The experimental findings suggest that D_{it} was mostly present in the lower part of the interface SiC band gap. In particular, the authors identified the split-interstitials configuration as a possible defect in the oxide, based on the energy levels in the SiC band gap, which is an electrically active defect [82]. In subsequent work, Knaup*et al.* considered both intrinsic and C-related defects on the oxide side of the interface [76].

A similar conclusion was reached by Deák *et al.*, whose computational study was focused on several oxidation paths related to C-defects, confirmed that carbon pairs were detrimental to SiC-based device operations. Their calculations indicate that carbon interstitials are expected to appear as carbon dimers or as carbon small clusters, not large carbon structures [42]. They explain that the split interstitial defect also gives rise to a deep-level state in the band gap. Subsequent work by Devynck *et al.* presented a comprehensive study for a wide range of the C-C pair configurations in the interface regions (in SiC and SiO_2). The data at the interface showed that the electronic structures followed a similar pattern as in the bulk SiC. The defects, comprising sp^2 hybridised carbon atoms in the bulk SiC, were identified as the origin of occupied energy levels in the mid-part and upper-part of the SiC band gap [104].

However, these results did not address or discuss how inter-sites (k- or h-site) differences might provide different results. Furthermore, geometrical and electronic structure differences were explored, but no studies related to the diffusion pathways were conducted. It was further concluded that, despite a large number of defects related to the carbon interstitial models could being identified, the main source of D_{it} remains unknown [104, 106].

From the existing literature [104, 106, 76, 42, 10, 18], it can be seen that there is a knowledge gap regarding the carbon interstitial effects in the interface region. Using the

AIMpro software, the main objectives of this chapter were formulated as follows:

1. Establish the geometric and electronic structure of the carbon split-interstitials at the interface (three layers and their differences), and comparisons with the bulk.
2. Show the impact of the interstitial geometric properties on the energetics of the split-interstitials at each site (k and h), as found in the bulk 4H-SiC.
3. Study the diffusion mechanisms of the split-interstitial defect in the vicinity of a model interface between SiO_2 and the 4H-SiC-(0001), highlighting the effect of the interface on $(C\text{-}C)_i$ diffusion.

This chapter results and discussion are associated with the work published in [80]

7.2 Computational Method

All the calculations were carried out using the density functional technique (DFT), and implemented using the AIMpro software package. The details of the software are described in chapter 2 and chapter 3 and this includes the basis set (see section 3.1.3). The diffusion processes of $(C\text{-}C)_i$ (section 3.2.5). The same computational approach used throughout this thesis to model SiC bulk was used to model the SiO_2/(0001)4H-SiC system, using a slab geometry approach. This was discussed in detail in the preceding chapter 5, in the section 5.3.2.

7.3 Results and discussion

7.3.1 Modelling of $(C\text{-}C)_C$ the at the interface

The main objective of this section is to better understand the differences in the nature of the carbon spit interstitials at the interfaces, with respect to the $(C\text{-}C)_C$ in the bulk 4H-SiC. In order to simulate these structures in the interface, the $(C\text{-}C)_C$ defect was computationally introduced, and as the system was optimised or relaxed, these were subjected to a large net relaxation, as be shown in the following section. The corresponding value of the $(C\text{-}C)_C$ in the h-site and $(C\text{-}C)_C$ in the k-site were based on the computational study of the 4H-SiC bulk, as presented in chapter 4. Based on the geometrical structures of $(\text{C-C})_{\text{C}}$ presented in section 4.3.2, the simulation results indicated that the relaxation around $(\text{C-C})_{\text{C}}$ at the *h*-site tended to be slightly lower than at the *k*-site 4.3.2 in case of bulk 4H-SiC.

The atomic geometrical structure around the defect in the interface was observed. In order to show the effect of the presence of the $(\text{C-C})_{\text{C}}$ on the surrounding Si-atom, the present calculations of the geometric parameters for the carbon pairs as a function of different distances (layers one, two, and three) on the neighbouring Si-C atoms are presented. Those results were also compared with the corresponding defects in the 4H-SiC bulk structures in both sites (*h* and *k*). The following sections provide more details of the defects in each layer.

7.3.1.1 $(\text{C-C})_{\text{C}}$ in the first layers

The geometric structure investigated for the bulk 4H-SiC was examined in the SiO_2/4H-SiC system, as shown in figure 7.1. The comparison of the geometric structure began with $(\text{C-C})_{\text{C}}$ at the first layer (figure 7.1–a). The process of the defect formation began with the carbon split-interstitials involvement, with the first Si-atom plane of the 4H-SiC-slab, located in the first C-layer, at the *h*-site of the 4H-SiC-slab (figure 7.1-a). As a result of relaxation, the $(\text{C-C})_{\text{C}}$ found its location at its equilibrium site in the first layer, at the SiO_2/4H-SiC interface; the split-interstitial had a similar co-ordination, as found in the bulk 4H-SiC. The angles and distances parameters of the defective structures are also indicated in figure 7.1. It is shown that the distance between the C-C pair was decreased by 1% compared to the bulk 4H-SiC, and the distances between the carbon atoms of the $(\text{C-C})_{\text{C}}$ and Si/C neighbours were very similar within the structures. In contrast, the angle parameters between the planes of the two C-atoms increased at a variation of 1% to 7%, in contrast to the defect structure in 4H-SiC. Despite the different chemical nature of the neighbours of the paired carbon atoms in the $(\text{C-C})_{\text{C}}$ defect model,Therfore, the overall structure parameters remained very similar to the defect configurations in the 4H-SiC bulk, as shown in figure 7.1, This result agree with [107, 76].

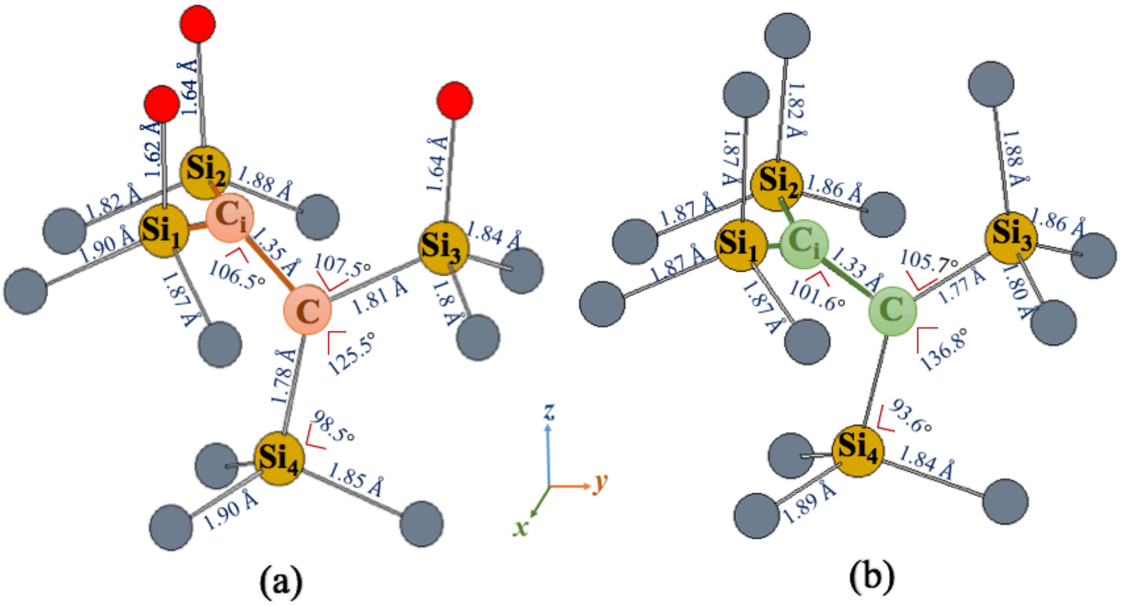
1.64 Å
1.62 Å
1.82 Å
Si2
1.88 Å
Si1
Ci
1.90 Å
1.35 Å
106.5°
107.5°
1.64 Å
Si3
1.84 Å
1.87 Å
C
1.81 Å
1.8 Å
125.5°
1.78 Å
98.5°
Si4
1.85 Å
1.90 Å
z
y
x
(a)
1.82 Å
1.87 Å
Si2
1.86 Å
1.87 Å
Si1
Ci
1.33 Å
105.7°
1.88 Å
Si3
1.86 Å
1.87 Å
101.6°
1.77 Å
1.80 Å
1.87 Å
C
136.8°
93.6°
Si4
1.84 Å
1.89 Å
(b)

Figure 7.1: Schematic of the simulated atomic structures, indicating the angles and bond lengths and angles of the (C-C)$_C$ at: (a) first layer at the interface and (b) the 4H-SiC bulk. Grey, red and yellow atoms represent C, O and Si atoms, respectively.

7.3.1.2 (C-C)$_C$ in the second layer

There examination of structural information of the (C-C)$_C$ in second layer is considered. The split-interstitial defect was introduced into in the second C-layer in the 4H-SiC slab, as shown in figure 7.2(a).The difference of this configuration (2Si –C–C–3Si) comparing with previous one in first layer comes from the positions of the Si atoms (*k*-site) bonding to the C pairs. This was a key difference between the first and the second layer. The coordination number (5) for the second layer was higher than the C–C pair surrounded by five neighbouring Si-atoms, compared to the split pairs in the first layer, surrounded by four Si-atom.

That means in this configuration, one carbon atom is involving with 3–silicon atoms of the SiC slab in a plane (Si$_{1,2.3}$, as illustrated in figure 7.2), and the other carbon pair links with a two silicon atoms (Si$_{4,5}$) that position within the *c*-axis. This coordination resembled in the equilibrium of the split pairs at the *k*-site in 4H-SiC (see section 4.3.2.2). It was found that the bond lengths of the defect at the interface in the second layer were longer than that of the bulk by 1% to 2%, and the angles were very different from those of a tetrahedron. Figure 7.2(b) summarises the distance and angle parameters of layer two, in comparison to the bulk. It can be seen that the angle of the Si$_1$–C–Si$_2$ increased by 7% in comparison with the bulk, while the angle difference in the (C-C)–Si$_3$ was less than 1%; this is in line with previous theoretical findings [104].

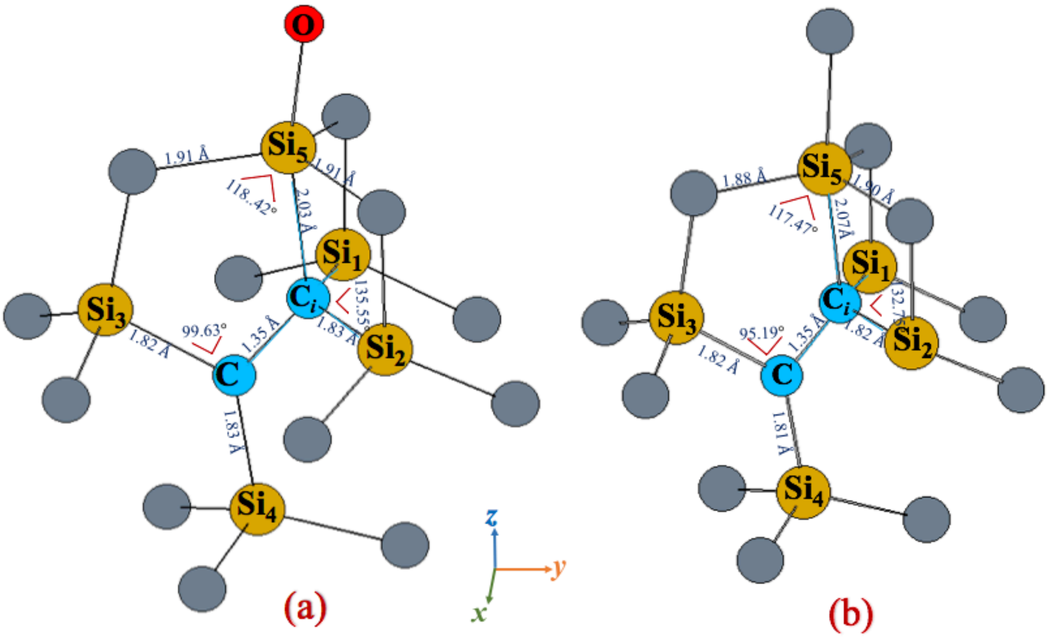
O
Si5
1.91 Å
1.91 Å
118..42°
2.03 Å
Si1
Ci
135.55°
1.83 Å
Si2
Si3
1.82 Å
99.63°
1.35 Å
C
1.83 Å
Si4
z
y
x
(a)
Si5
1.88 Å
1.90 Å
117.47°
2.07Å
Si1
Ci
132.75
1.82 Å
Si2
Si3
95.19°
1.35 Å
1.82 Å
C
1.81 Å
Si4
(b)

Figure 7.2: Schematic of the simulated atomic structures indicating the angles and bond lengths and angles of the (C-C)$_\text{C}$ at: (a) the second layer at the interface and (b) the 4H-SiC bulk. Grey, red and yellow atoms represent C, O and Si atoms, respectively.

7.3.1.3 (C-C)$_\text{C}$ in the third layer

In the third layer, the structure of the defectremained very similar to the defect configurations at the *h*-site in the 4H-SiC, as shown in figure 7.3. For the defect model in the third layer, the only slightly noticeable difference from the bulk was for the angle between the two carbon spilt-interstitial defect, while the other structural parameters remained almost unchanged. In particular, calculations showed that changes in the distances of the next neighbours of Si atoms were unchanged, corresponding to the bulk 4H-SiC. This presents a reference for the diffusion calculations, which will be presented later in this chapter.

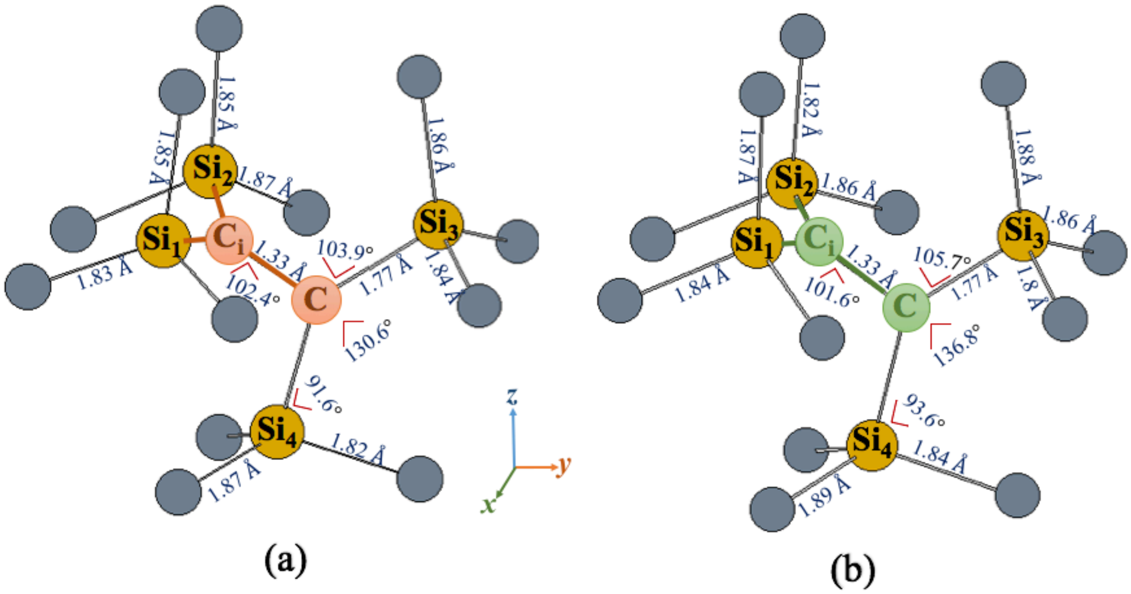
1.85 Å
1.85 Å
Si$_2$
1.87 Å
Si$_1$
C$_i$
1.33 Å
103.9°
1.77 Å
1.86 Å
Si$_3$
1.84 Å
1.83 Å
102.4°
C
130.6°
91.6°
Si$_4$
1.82 Å
1.87 Å
z
y
x
(a)
1.82 Å
1.87 Å
Si$_2$
1.86 Å
Si$_1$
C$_i$
1.33 Å
105.7°
1.77 Å
1.88 Å
Si$_3$
1.86 Å
1.8 Å
1.84 Å
101.6°
C
136.8°
93.6°
Si$_4$
1.84 Å
1.89 Å
(b)

Figure 7.3: Schematic of the simulated atomic structures indicating the angles and bond lengths and angles of the (C-C)$_C$ at: (a) the third layer at the interface and (b) the 4H-SiC bulk. Grey, red and yellow atoms represent C, O and Si atoms, respectively.

7.3.2 Diffusion of the (C-C)$_\mathrm{C}$ interfacial layer at the interface

As illustrated in Chapter 4, the motion of (C-C)$_\mathrm{C}$ as a split-interstitial configuration (C-C)$_\mathrm{C}$ process involves the motion of one of the carbon atoms in the initial split-interstitial configuration moving to the adjacent basal-plane, yielding a barrier of 0.86 eV; this shows good agreement with an existing study [108]. For comparison, an approach in which (C-C)$_\mathrm{C}$ might diffuse in the bulk was also examined in the vicinity of the SiO$_2$/(0001)4H-SiC interface. In order to study the motion of (C-C)$_\mathrm{C}$ in the vicinity of the interface, two cases were investigated. We assumed that the defect initially lay in the topmost carbon layer, which in our model system placed it at an k-site; there are two possible steps: For comparison, the approach in which in bulk might diffuse has also examined in the vicinity of the SiO$_2$/(0001)4H-SiC interface. In order to study the motion of at the vicinity of the interface, two cases have been investigated. Assuming that the defect initially lies in the topmost carbon layer, which in our model system places it at an h-site, in this study, there are two possible steps: kh and hk, which means the (C-C)$_\mathrm{C}$ moves from the first layer (from k-site) at an interface to the second layer (h-site). While the second path is from the second to the third layer, as shown in figure 7.4.

7.3.2.1 Single hop for $(C\text{-}C)_C$ at the c-axis

Processes involving the motion of $(C\text{-}C)_C$ in the vicinity of the interface were modelled. The initial step involved the topmost carbon layer in the interfacial layer, which in this model system placed it at an k-site. The final configuration placed the $(C\text{-}C)_C$ at a h-site in the second layer from the interface. The processes corresponding to those investigated for bulk 4H-SiC were examined in the SiO_2/4H-SiC system. The processes for the activation energy of these migration process hops are shown in figure 7.5. The results showed that the barrier relative form of the $(C\text{-}C)_C$ moving in the interfacial layer was lower than 1 eV, which is less than that of the motion from the corresponding bulk structure. This configuration was used to define zero on the energy scale, as shown in figure 7.5.

Based on the atomic coordination network shown in figure 7.4, the C-atom in the first layer was surrounded by three silicon atoms, and changed to four-fold coordination of the carbon atoms in the split-interstitial configuration in the second layer. A significant impact was observed on the energies, and the underlying geometry of the split-interstitials at each site (k and h) was the same as found in the bulk 4H-SiC.

The mechanisms of the possible migration pathways from the second to third layer have been further studied. For the overall energy barrier of the process of the carbon split-interstitials, which is labelled 3-4 (figure 7.4), the maximum energy is approximately the same for both the interfacial and the bulk processes. A comparison of the bulk and interfacial energy profiles is shown in figures 7.5. For the second stage (3-4 in figure 7.5), both the overall barrier shape and the absolute energies matched well, supporting the view that the environment beyond the first Si-C bi-layer from the SiO_2/4H-SiC interface was very similar to the bulk 4H-SiC structure.

Experimental evidence [109, 76] reports that interstitial carbon produces trap states, and it has been found that the region immediately adjacent to the SiO_2 layer is an energetically favourable environment for $(C\text{-}C)_C$. This being the case, the build-up of carbon in this region is expected to give rise to a potentially high concentration of interfacial traps.

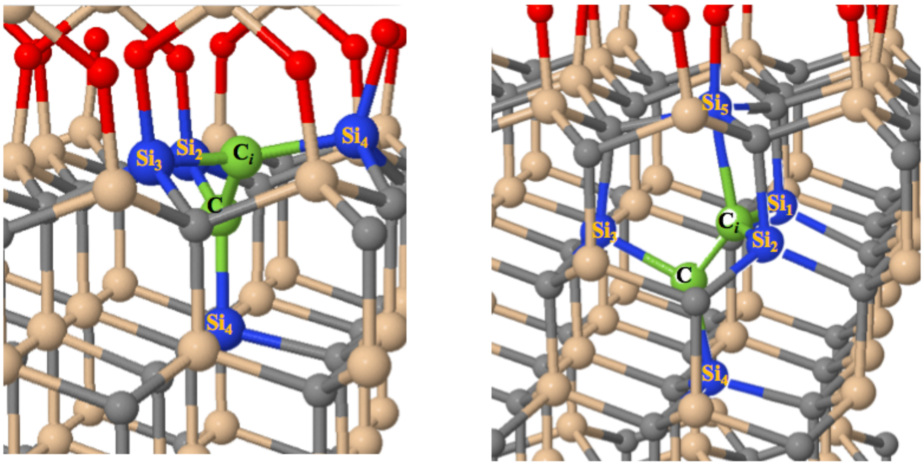

First diffusion process $\xrightarrow{step(1)} (C-C)_C^k \xrightarrow{step(2)} (C-C)_C^h$

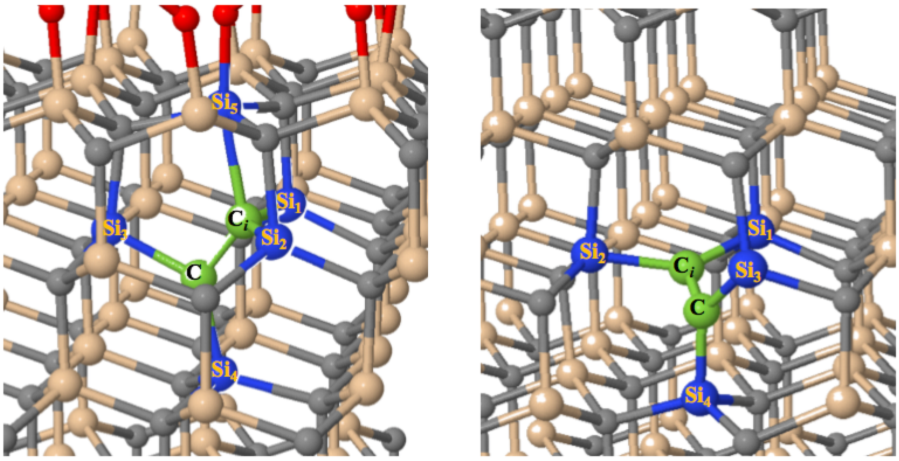

Second diffusion process $\xrightarrow{step(2)} (C-C)_C^h \xrightarrow{step(3)} (C-C)_C^k$

Figure 7.4: illustration of (C-C)$_C$ diffusion at the SiO$_2$/4H-SiC interface: (1) the initial step (in k site); and (2) the final step (in h site) between first and second layers in 4H-SiC slab. while (3)(in h site) and (4) (in k site) step. This shows the diffusion process of (C-C)$_C$ between the initial (3) and final (4) structures.

7.4 Chapter Summary

Using the DFT approach, the diffusion processes of (C-C)$_C$ in the vicinity of the SiO$_2$/4H-SiC interface were simulated, and the results are presented in this chapter. It has been demonstrated that the carbon spilt-interstitial structure effect, and the energy associated with this, was extremely low. The (C-C)$_C$ from the interface. In contrast, the diffusion

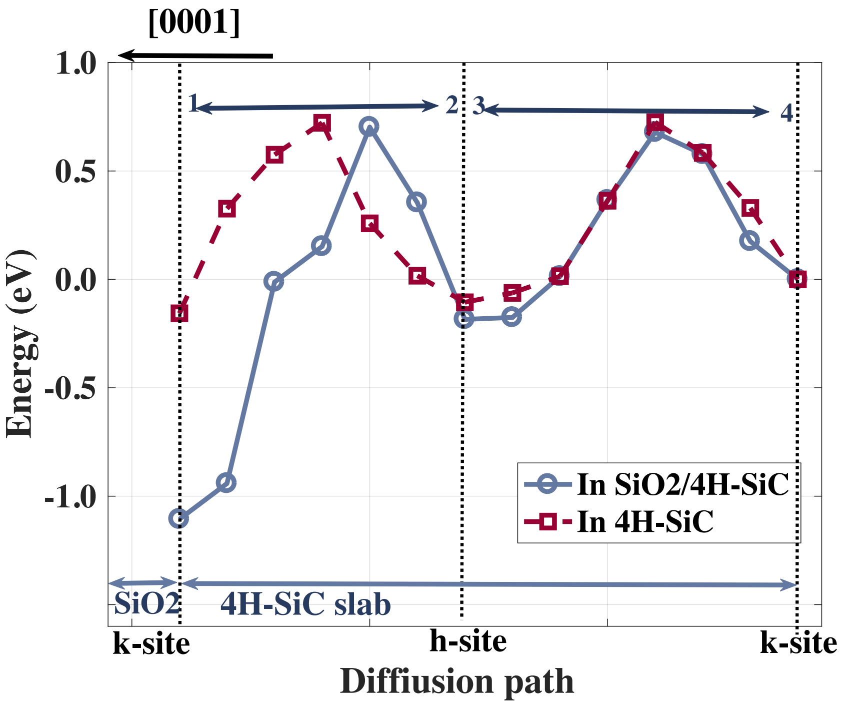

Figure 7.5: Minimum energy paths for in bulk 4H-SiC (dashed red) and interfaces (solid blue). To facilitate comparison, the zero on the energy scale is defined as the k-site energy at the end of the process.1-4 are as indicated in the labelling of figure 7.4.

(C-C)$_C$ at the first layer in the interface was strongly affected, with the interstitial being energetically stabilised at roughly 1 eV, compared to the 4H-SiC bulk behaviour. This stabilisation was expected to inhibit the injection of single self-interstitials into the bulk 4H-SiC. The processes by which oxidation resulted in the modification of deep traps within the SiC remains to be fully understood, and thus this area may serve as a potential future research direction.

Part III

Conclusions

Chapter 8

Summary and Future Work

8.1 Conclusion

As mentioned in chapter 1, semiconductor devices have had a great impact on society by enabling us to power any gadget that we use. However, it is surprising how much we are limited by the choice of materials to help manufacture these devices. The ideal material would function properly at high temperature and yet provide high power throughput. Over the years, 4H-SiC has been a great candidate for these purposes due to its wide band gap, and is easy to extract from its much abundant native oxide SiO_2. A key challenge undermining 4H-SiC as the material that underpins this technology is its purity. Electrically-active defects (carbon-related defects) are common in these materials and give used states located deep within the band gap arising from native defects in the SiC, close to the SiO_2 interfaces. Most common of these carbon vacancy defects in the 4H-SiC bulk structure and the SiO_2/4H-SiC interface are key challenges to overcome in order to manufacture high efficiency semiconductor devices. Previously, understanding of these carbon-related defects has been explored via DLTS experimental studies, but these have been limited to observable and measurable aspects in [30, 65, 66, 33, 19, 3, 67, 68, 69]. Previous computational researchers have shown that experiments can reproduce the underlying physics through first principle DFT models [19, 5, 34, 29].

In this thesis, a computational DFT study is presented specifically to understand the geometric features of carbon vacancy defects and interstitial defects and their migration in the vicinity of the SiO_2/4H-SiC interface. The DFT theory was previously implemented in software developed by an emerging material technology research group at Newcastle University. The code effectively determines the structure of an assembly of atoms by solving Schrodinger equations for electrons by making a certain set of approximations. In this thesis, the AIMpro simulations have been deployed to investigate the carbon vacancy have been studies and the interstitial defects: structures, electrical properties, and diffusion energetics. The modelling work in this thesis takes advantage of the periodic boundary conditions for computationally feasible bulk and interface studies. Chapters 4–7 lay out computational studies with increasing modelling complexity, building on the work from the conclusions of previous chapters.

These studies from chapter 4 validated the computational approach to model the 4H-SiC structure with the emphasis on the geometrical features of the different lattice site configurations of the carbon related defects. The chapter also explored the diffusion pathways of these defects and compared the results with computational studies from the existing literature. It was found out via the bulk calculations that there is a slight difference in the inequivalent lattice sites in the h and k bilayers in the unit cell, although the difference between the energies of V_C is quite small. The difference was shown to increase with the increase in the charged states due to the relaxation after the removal of the carbon atom and the chemistry results in a covalent bond between the Si atoms around the defect in the different charged states. The simulations studied the electrical activity of V_C for the h and k sites at different charged states, supporting the assignment of the double acceptor level to $Z_{1/2}$ and $EH_{6/7}$ to the single donor level. Further simulations were conducted to understand all the possible migration pathways: parallel and perpendicular directions of V_C in 4H/SiC as well as variously charged states. V_C calculations in the two different migration directions suggested that the V_C can move more freely along the basal plane via the h and k sites, as opposed to the perpendicular direction. The energy barrier for the positively charge states across all migration pathways is higher than that for the negatively charged states. Furthermore, single and di-interstitial carbon defects were successfully computationally reproduced. The electronic and the band calculations were found to be in excellent agreement with the experimental and theoretical results. These studies from chapter 4 provided a validation of the computational approach to model 4H-SiC.

Using AIMpro software and the same computational approach as in chapter 4, a model structure system for SiO_2 and the SiO_2/4H-SiC interface was simulated, for use in the subsequent chapters on carbon vacancy (chapter 6) and carbon interstitial defect studies (chapter 7). Furthermore, a comparative study of the diffusion of carbon vacancies at the h- and k-(0001) faces of the SiO_2/(0001) 4H-SiC interface showed no significant difference between these interfaces, but a diffusion energy was found to be greater by 15%, compared to that in the bulk 4H-SiC structures. The chapter 6 built on this work in term of the details of the geometry and electronic structure of the vacancy (as it moves in the interfacial layer).

Chapter 6 and 7 further determined that the carbon-vacancies, which are known to be key carrier traps, have their diffusion hindered in the vicinity of a SiO_2/(0001)-4H-SiC interface, with the overall activation energy ∼15% higher in the immediate interface than two-to-three bi-layers into the SiC where they behave as in bulk SiC. It is also thought that oxidation of SiC introduces carbon interstitials to device channels, and the diffusion C_i in the vicinity of the interface with SiO_2 was also been simulated. It is found that the interface stabilises $(C\text{-}C)_i$ even more than V_C, lower its energy by ∼1 eV relative to bulk. In addition, it was found that if the vacancy lies in more than two SiC bi-layers from the interface, its behaviour differs insignificantly from the equivalent bulk.

For the diffusion mechanisms, the interfacial layer was found to have a higher activation energy due to the stabilisation of the vacancy. It was further noted that the findings of higher barriers and the stabilisation of vacancies at the SiO_2/4H-SiC interface are consistent with the high density of trap in this region which was observed experimentally [101]. The first layer of the interface was shown to be very strongly affected by the carbon vacancy and the interstitial defects. The layer was energetically stabilised by about ∼1 eV as compared to the bulk. The energetic stabilisation was expected to inhibit the injection of single self-interstitials into the bulk 4H-SiC. It is thus concluded that in devices such as MOSFETs control over the injection of self-interstitials to modify the profile of trap states within the channel, and therefore the carrier lifetime, is rate-limited by this initial step.

8.2 Future Outlook

This study contributes to a better understanding of the mechanism of carbon vacancy defect and carbon interstitial defects at the interface and can be useful for the interpretation of experimental observations. The improvement of processing techniques reduces the trap density of defects at the interface. Based on the understanding in this thesis, the following three themes can be explored by future researchers for high impact work to lead to potential improvements in the performances of high performance electronic devices.

Understanding of the carbon spilt-interstitial defect was significantly extended in this thesis (chapter 7). However, certain aspects of these defect structures such as the ON1 and ON2 centres remain to be determined in detail due to the time limitations; this remains an interesting endeavour for future researchers. These centres are primarily generated during the thermal oxidation process and were previously reported to be responsible for reduction of of $Z_{1/2}$ and $EH_{6/7}$ centres [98] and acts as the generation process for the carbon interstitials [10, 80]. Deeper understanding of physical structure of this defect is essential

Potential utilisation of nitrogen as doping agents for reducing the interface defect densities has been previous explored [110] based on the fact that the N is thermodynamically favourable [104]. However, there is a general lack of in-depth knowledge on the kinetics of this configuration and an opportunity lies to explore this via first principle modelling. A computational study building on the work of the current thesis can further establish the benefits of N atom and other element such as Al, B and O as doping agents.

In this thesis, interface models (chapter 5) have been implemented extensive to simulate and study defects such as V_{C} and C_i in Si-face. Therefore, a natural reapplication of this work would be to apply the methodology to other interesting orientations such as $(11\bar{2}0)$. This configuration remains unexplored in this work, the experimental observations that this orientation can lead to a higher carrier mobility [111]. Future researchers are encouraged to explore these themes to further improve the electronic device performance

Bibliography

[1] F. B. Arith, *4H-SiC metal oxide semiconductor devices.* PhD thesis, Newcastle University, 2018.

[2] K. Kawahara, “Identification of deep levels in SiC and their elimination for carrier lifetime enhancement,” 2013.

[3] K. Kawahara, J. Suda, and T. Kimoto, “Analytical model for reduction of deep levels in SiC by thermal oxidation,” *Journal of Applied Physics*, vol. 111, no. 5, p. 053710, 2012.

[4] Z. Zolnai, “Irradiation-induced crystal defects in silicon carbide,” 2005.

[5] L. Gordon, A. Alkauskas, W. F. Koehl, A. Janotti, D. D. Awschalom, and C. G. Van de Walle, “Defects as qubits in 3C and 4H polymorphs of SiC,” in *APS Meeting Abstracts*, 2015.

[6] O. Madelung, *Semiconductors: group IV elements and III-V compounds.* Springer Science & Business Media, 2012.

[7] A. Mattausch, *Ab initio-Theory of Point Defects and Defect Complexes in SiC.* PhD thesis, University of Erlangen-Nuremberg, 2005.

[8] M. Y. Zaman and C. F. Pirri, *Modeling and Characterization of Metal/SiC Interface for Power Device Application.* PhD thesis, 2012.

[9] E. Acheson, “Production of artificial crystalline carbonaceous materials,” U.S. Patent 492 767, Feb 1893.

[10] T. Kimoto, K. Danno, and J. Suda, "Lifetime-killing defects in 4H-SiC epilayers and lifetime control by low-energy electron irradiation," *Physica Status Solidi (b)*, vol. 245, no. 7, pp. 1327–1336, 2008.

[11] J. A. Lely, "Darstellung von einkristallen von siliciumcarbid und beherrschung von art und menge der im gitter eingebauten verunreinigungen," *Angewandte Chemie*, vol. 66, no. 22, pp. 713–713, 1954.

[12] M. I. B. Idris, *Surface engineering for silicon carbide interface.* PhD thesis, Newcastle University, 2018.

[13] V. Heydemann, N. Schulze, D. Barrett, and G. Pensl, "Growth of 6H and 4H silicon carbide single crystals by the modified Lely process utilizing a dual-seed crystal method," *Applied Physics Letters*, vol. 69, no. 24, pp. 3728–3730, 1996.

[14] Y. Ding, *Quantum well state of cubic inclusions in hexagonal silicon carbide studied with ballistic electron emission microscopy.* PhD thesis, The Ohio State University, 2004.

[15] S. Mendis, *Thermal Diffusion of Dopants in Silicon Carbide.* PhD thesis, Auburn University-US, 2012.

[16] L. S. Ramsdell, "Studies on silicon carbide," *American Mineralogist: Journal of Earth and Planetary Materials*, vol. 32, no. 1-2, pp. 64–82, 1947.

[17] K. Kawahara, X. Thang Trinh, N. Tien Son, E. Janzén, J. Suda, and T. Kimoto, "Quantitative comparison between $\mathrm{z}_{1/2}$ center and carbon vacancy in 4H–SiC," *Journal of Applied Physics*, vol. 115, no. 14, p. 143705, 2014.

[18] S. Ichikawa, K. Kawahara, J. Suda, and T. Kimoto, "Carrier recombination in n-type 4H-SiC epilayers with long carrier lifetimes," *Applied Physics Express*, vol. 5, no. 10, p. 101301, 2012.

[19] T. Hornos, A. Gali, and B. G. Svensson, "Large-scale electronic structure calculations of vacancies in 4H-SiC using the heyd-scuseria-ernzerhof screened hybrid density functional," in *Materials Science Forum*, vol. 679, pp. 261–264, Trans Tech Publ, 2011.

[20] T. Umeda, J. Isoya, N. Morishita, T. Ohshima, and T. Kamiya, "EPR identification of two types of carbon vacancies in 4H-SiC," *Physical Review B*, vol. 69, no. 12, p. 121201, 2004.

[21] F. Devynck, F. Giustino, P. Broqvist, and A. Pasquarello, "Structural and electronic properties of an abrupt 4H-SiC(0001)/SiO_2 interface model: Classical molecular dynamics simulations and density functional calculations," *Physical Review B*, vol. 76, no. 7, p. 075351, 2007.

[22] K. Kawahara, J. Suda, and T. Kimoto, "Analytical model for reduction of deep levels in sic by thermal oxidation," *Journal of Applied Physicsournal of Applied Physics*, vol. 111, no. 5, p. 053710, 2012.

[23] Z. Fang, D. C. Look, A. Saxler, and W. C. Mitchel, "Characterization of deep centers in bulk n-type 4H-SiC," *Physica B: Condensed Matter*, vol. 308, pp. 706–709, 2001.

[24] T. Petrenko, T. Petrenko, V. Y. Bratus, and J. Monge, "Calculation of hyperfine parameters of positively charged carbon vacancy in sic," *Physica B: Condensed Matter*, vol. 308, pp. 637–640, 2001.

[25] L. Torpo, T. Staab, and R. M. Nieminen, "Divacancy in 3C- and 4H-SiC: An extremely stable defect," *Physical Review B*, vol. 65, no. 8, p. 085202, 2002.

[26] L. C. Martin, *Characterisation of silicon carbide CMOS devices for high temperature applications*. PhD thesis, Newcastle University, 2015.

[27] T. Hiyoshi and T. Kimoto, "Reduction of deep levels and improvement of carrier lifetime in n-type 4H-SiC by thermal oxidation," *Applied Physics Express*, vol. 2, no. 4, p. 041101, 2009.

[28] J. Schneider and K. Maier, "Point defects in silicon carbide," *Physica B: Condensed Matter*, vol. 185, no. 1-4, pp. 199–206, 1993.

[29] A. Mattausch, M. Bockstedte, and O. Pankratov, "Structure and vibrational spectra of carbon clusters in SiC," *Physical Review B*, vol. 70, no. 23, p. 235211, 2004.

[30] M. Bockstedte, A. Gali, A. Mattausch, O. Pankratov, and J. W. Steeds, "Identification of intrinsic defects in SiC: Towards an understanding of defect aggregates by combining theoretical and experimental approaches," *physica status solidi (b)*, vol. 245, no. 7, pp. 1281–1297, 2008.

[31] E. Rauls, T. Lingner, Z. Hajnal, S. Greulich-Weber, T. Frauenheim, and J.-M. Spaeth, "Metastability of the neutral silicon vacancy in 4H-SiC," *Physica Status Solidi B*, vol. 217, no. 2, pp. r1–r3, 2000.

[32] T. Liao, G. Roma, and J. Wang, "Neutral silicon interstitials in silicon carbide: a first principles study," *Philosophical Magazine*, vol. 89, no. 26, pp. 2271–2284, 2009.

[33] F. Gao, M. Posselt, V. Belko, Y. Zhang, and W. J. Weber, "Structures and energetics of defects: a comparative study of 3C-and 4H-SiC," *Nuclear Instruments and Methods in Physics Research Section B: Beam Interactions with Materials and Atoms*, vol. 218, pp. 74–79, 2004.

[34] M. Bockstedte, A. Mattausch, and O. Pankratov, "Ab initio study of the migration of intrinsic defects in 3C-SiC," *Physical Review B*, vol. 68, no. 20, p. 205201, 2003.

[35] O. A. S. Al-Ani, *Nanoscale modelling of point and extended defects in mc-Si solar cell*. PhD thesis, Newcastle University, 2018.

[36] V. Afanasev, M. Bassler, G. Pensl, and M. Schulz, "Intrinsic SiC/SiO$_2$ interface states," *physica status solidi (a)*, vol. 162, no. 1, pp. 321–337, 1997.

[37] J. Rozen, *Electronic properties and reliability of the silicon dioxide/silicon carbide interface*. PhD thesis, Vanderbilt University, 2008.

[38] E. Pippel, J. Woltersdorf, H. Ö. Ólafsson, and E. Ö. Sveinbjörnsson, "Interfaces between 4H-SiC and SiO$_2$: Microstructure, nanochemistry, and near-interface traps," *Journal of Applied Physics*, vol. 97, no. 3, p. 034302, 2005.

[39] N. Tajima, T. Kaneko, T. Yamasaki, J. Nara, T. Schimizu, K. Kato, and T. Ohno, "First-principles study on C=C defects near SiC/SiO$_2$ interface: Defect passivation by double-bond saturation," *Japanese Journal of Applied Physics*, vol. 57, no. 4S, p. 04FR09, 2018.

[40] V. Afanas ev, A. Stesmans, M. Bassler, G. Pensl, M. Schulz, and C. Harris, "SiC/SiO$_2$ interface-state generation by electron injection," *Journal of Applied Physics*, vol. 85, no. 12, pp. 8292–8298, 1999.

[41] J. P. Cottom, *The characterisation of performance limiting defects in 4H-SiC devices using density functional theory.* PhD thesis, University College London, 2017.

[42] P. Deák, J. M. Knaup, T. Hornos, C. Thill, A. Gali, and T. Frauenheim, "The mechanism of defect creation and passivation at the SiC/SiO$_2$ interface," *Journal of Physics D: Applied Physics*, vol. 40, no. 20, p. 6242, 2007.

[43] K. Kawahara, X. Thang Trinh, N. Tien Son, E. Janzén, J. Suda, and T. Kimoto, "Investigation on origin of Z$_1$/2 center in SiC by deep level transient spectroscopy and electron paramagnetic resonance," *Applied Physics Letters*, vol. 102, no. 11, p. 112106, 2013.

[44] N. T. Son, X. T. Trinh, L. S. Løvlie, B. G. Svensson, K. Kawahara, J. Suda, T. Kimoto, T. Umeda, J. Isoya, T. Makino, *et al.*, "Negative-u system of carbon vacancy in 4H-SiC," *Physical review letters*, vol. 109, no. 18, p. 187603, 2012.

[45] A. Kawasuso, F. Redmann, R. Krause-Rehberg, M. Weidner, T. Frank, G. Pensl, P. Sperr, W. Triftshäuser, and H. Itoh, "Annealing behavior of vacancies and Z$_{1/2}$ levels in electron-irradiated 4H-SiC studied by positron annihilation and deep-level transient spectroscopy," *Applied Physics Letters*, vol. 79, no. 24, pp. 3950–3952, 2001.

[46] P. Briddon and R. Jones, "LDA calculations using a basis of gaussian orbitals," *Physica Status Solidi (b)*, vol. 217, no. 1, pp. 131–171, 2000.

[47] M. Born and R. Oppenheimer, "On the quantum theory of molecules," *Ann. Phys*, vol. 84, no. 4, pp. 457–484, 1927.

[48] P. Hohenberg and W. Kohn, "Inhomogeneous electron gas," *Physical Review*, vol. 136, no. 3B, p. B864, 1964.

[49] W. Kohn and L. Sham, "Quantum density oscillations in an inhomogeneous electron gas," *Physical Review*, vol. 137, no. 6A, p. A1697, 1965.

[50] M. Al-Hadidi, *A density functional study of point defects in nanoelectrical materials.* PhD thesis, Newcastle University, 2015.

[51] C. Hartwigsen, S. Gœdecker, and J. Hutter, "Relativistic separable dual-space gaussian pseudopotentials from H to Rn," *Physical Review B*, vol. 58, no. 7, p. 3641, 1998.

[52] C. W. Castleton, A. Höglund, and S. Mirbt, "Density functional theory calculations of defect energies using supercells," *Modelling and Simulation in Materials Science and Engineering*, vol. 17, no. 8, p. 084003, 2009.

[53] Y. Zhang, *First-principles statistical mechanics approach to step decoration at solid surfaces.* PhD thesis, Freie Universität Berlin Berlin, 2008.

[54] H. J. Monkhorst and J. D. Pack, "Special points for brillouin-zone integrations," *Physical review B*, vol. 13, no. 12, pp. 5188–5192, 1976.

[55] F. Murnaghan, "The compressibility of media under extreme pressures," *Proceedings of the national academy of sciences of the United States of America*, vol. 30, no. 9, p. 244, 1944.

[56] F. Birch, "Finite elastic strain of cubic crystals," *Physical review*, vol. 71, no. 11, p. 809, 1947.

[57] G. Zhao and D. Bagayoko, "Electronic structure and charge transfer in 3C-and 4H-SiC," *New Journal of Physics*, vol. 2, no. 1, p. 16, 2000.

[58] A. Zywietz, J. Furthmüller, and F. Bechstedt, "Neutral vacancies in group-iv semiconductors," *Physica Status Solidi (b)*, vol. 210, no. 1, pp. 13–29, 1998.

[59] A. Gali, "Time-dependent density functional study on the excitation spectrum of point defects in semiconductors," *Physica Status Solidi B*, vol. 248, no. 6, pp. 1337–1346, 2011.

[60] G. Henkelman and H. Jónsson, "Improved tangent estimate in the nudged elastic band method for finding minimum energy paths and saddle points," *The Journal of chemical physics*, vol. 113, no. 22, pp. 9978–9985, 2000.

[61] G. Henkelman, B. P. Uberuaga, and H. Jónsson, "A climbing image nudged elastic band method for finding saddle points and minimum energy paths," *Journal of Chemical pPhysics*, vol. 113, no. 22, pp. 9901–9904, 2000.

[62] L. Torpo, M. Marlo, T. Staab, and R. Nieminen, "Comprehensive ab initio study of properties of monovacancies and antisites in 4H-SiC," *Journal of Physics: Condensed Matter*, vol. 13, no. 28, p. 6203, 2001.

[63] J. Furthmüller, A. Zywietz, and F. Bechstedt, "Monovacancies in 3C and 4H-SiC," *Materials Science and Engineering: B*, vol. 61, pp. 244–247, 1999.

[64] I. Capan, T. Brodar, Ž. Pastuović, R. Siegele, T. Ohshima, S.-i. Sato, T. Makino, L. Snoj, V. Radulović, J. Coutinho, *et al.*, "Double negatively charged carbon vacancy at the h-and k-sites in 4H-SiC: Combined laplace-DLTS and DFT study," *Journal of Applied Physics*, vol. 123, no. 16, p. 161597, 2018.

[65] J. Xi, B. Liu, F. Yuan, Y. Zhang, and W. J. Weber, "Diffusion of point defects near stacking faults in 3C-SiC via first-principles calculations," *Scripta Materialia*, vol. 139, pp. 1–4, 2017.

[66] J. Xi, B. Liu, Y. Zhang, and W. J. Weber, "Ab initio study of point defects near stacking faults in 3C-SiC," *Computational Materials Science*, vol. 123, pp. 131–138, 2016.

[67] T. Kimoto and J. A. Cooper, *Fundamentals of silicon carbide technology: growth, characterization, devices and applications.* John Wiley & Sons, 2014.

[68] G. Alfieri and T. Kimoto, "Resolving the $\mathrm{EH}_{6/7}$ level in 4H-SiC by laplace-transform deep level transient spectroscopy," *Applied Physics Letters*, vol. 102, no. 15, p. 152108, 2013.

[69] T. Kimoto, H. Niwa, T. Okuda, E. Saito, Y. Zhao, S. Asada, and J. Suda, "Carrier lifetime and breakdown phenomena in SiC power device material," *Journal of Physics D: Applied Physics*, vol. 51, no. 36, p. 363001, 2018.

[70] K. Danno, D. Nakamura, and T. Kimoto, “Investigation of carrier lifetime in 4H-SiC epilayers and lifetime control by electron irradiation,” *Applied Physics Letters*, vol. 90, no. 20, p. 202109, 2007.

[71] I. D. Booker, H. Abdalla, J. Hassan, R. Karhu, L. Lilja, E. Janzén, and E. Sveinbjörnsson, “Oxidation-induced deep levels in n-and p-type 4H- and 6H-SiC and their influence on carrier lifetime,” *Physical Review Applied*, vol. 6, no. 1, p. 014010, 2016.

[72] X. T. Trinh, K. Szász, T. Hornos, K. Kawahara, J. Suda, T. Kimoto, A. Gali, E. Janzén, and N. T. Son, “Identification of the negative carbon vacancy at quasi-cubic site in 4H-SiC by EPR and theoretical calculations,” in *Materials Science Forum*, vol. 778, pp. 285–288, Trans Tech Publ, 2014.

[73] P. Carlsson, N. Son, F. Beyer, H. Pedersen, J. Isoya, N. Morishita, T. Ohshima, and E. Janzén, “Deep levels in low-energy electron-irradiated 4H-SiC,” *Physica Status Solidi*, vol. 3, no. 4, pp. 121–123, 2009.

[74] L. Storasta and H. Tsuchida, “Reduction of traps and improvement of carrier lifetime in 4H-SiC epilayers by ion implantation,” *Applied Physics Letters*, vol. 90, no. 6, p. 062116, 2007.

[75] T. Petrenko, T. Petrenko, V. Y. Bratus, and J. Monge, “Calculation of hyperfine parameters of positively charged carbon vacancy in SiC,” *Physica B: Condensed Matter*, vol. 308, pp. 637–640, 2002.

[76] J. M. Knaup, P. Deák, T. Frauenheim, A. Gali, Z. Hajnal, and W. Choyke, “Theoretical study of the mechanism of dry oxidation of 4H-SiC,” *Physical Review B*, vol. 71, no. 23, p. 235321, 2005.

[77] A. Gali, “Time-dependent density functional study on the excitation spectrum of point defects in semiconductors,” *Physica Status Solidi B*, vol. 248, no. 6, pp. 1337–1346, 2011.

[78] J. Isoya, T. Umeda, N. Mizuochi, N. Son, E. Janzén, and T. Ohshima, "EPR identification of intrinsic defects in SiC," *Physica Status Solidi (b)*, vol. 245, no. 7, pp. 1298–1314, 2008.

[79] J. Davidsson, V. Ivády, R. Armiento, N. Son, A. Gali, and I. A. Abrikosov, "First principles predictions of magneto-optical data for semiconductor point defect identification: the case of divacancy defects in 4H-SiC," *New Journal of Physics*, vol. 20, no. 2, p. 023035, 2018.

[80] H. Alsnani, J. Goss, O. Al-Ani, S. Olsen, P. Briddon, M. Rayson, and A. Horsfall, "Investigation of carbon interstitials in the vicinity of the $\mathrm{Si0_2}$/4H-SiC(0001) interface," in *2018 International Semiconductor Conference (CAS)*, pp. 231–234, IEEE, 2018.

[81] M.-J. Zheng, N. Swaminathan, D. Morgan, and I. Szlufarska, "Energy barriers for point-defect reactions in 3C-SiC," *Physical Review B*, vol. 88, no. 5, p. 054105, 2013.

[82] A. Gali, P. Deák, P. Ordejón, N. Son, E. Janzén, and W. Choyke, "Aggregation of carbon interstitials in silicon carbide: A theoretical study," *Physical Review B*, vol. 68, no. 12, p. 125201, 2003.

[83] E. Rauls, T. Staab, Z. Hajnal, and T. Frauenheim, "Interstitial-based vacancy annealing in 4H-SiC," *Physica B: Condensed Matter*, vol. 308, pp. 645–648, 2001.

[84] S. Dhar, L. C. Feldman, S. Wang, T. Isaacs-Smith, and J. Williams, "Interface trap passivation for $\mathrm{SiO_2}$/C-terminated 4H-SiC," *Journal of Applied Physics*, vol. 98, no. 1, p. 014902, 2005.

[85] T. Hirose, D. Mori, and Y. Teraot, "Atomic level analysis of SiC devices using numerical simulation," *Fuji Electric Review*, vol. 62, no. 1, pp. 23–27, 2016.

[86] T. Akiyama, S. Hori, K. Nakamura, T. Ito, H. Kageshima, M. Uematsu, and K. Shiraishi, "Reaction mechanisms at 4H-SiC/$\mathrm{SiO_2}$ interface during wet SiC oxidation," *Japanese Journal of Applied Physics*, vol. 57, no. 4S, p. 04FR08, 2018.

[87] J. Sołtys, J. Piechota, M. Łopuszyński, and S. Krukowski, "A comparative dft study of electronic properties of 2H-, 4H- and 6H-SiC (0001) and SiC clean surfaces:

significance of the surface stark effect," *New Journal of Physics*, vol. 12, no. 4, p. 043024, 2010.

[88] A. Miyashita, T. Ohnuma, M. Iwasawa, T. Sakai, T. Kano, M. Yoshikawa, and N. Soneda, "Generation of amorphous SiO_2/SiC interface and dynamical simulation of interface oxidation process of SiC device," *Annual Report of the Earth Simulator Center April*, vol. 2006, 2005.

[89] B. Wenzien, P. Käckell, and F. Bechstedt, "Vacancy-induced 2× 2 reconstruction of the si-terminated 3c sic (111) surface: ab initio calculations of the atomic and electronic structure," *Surface science*, vol. 331, pp. 1105–1109, 1995.

[90] H.-J. Sung, D.-H. Choe, and K.-J. Chang, "The effects of surface polarity and dangling bonds on the electronic properties of monolayer and bilayer mos2 on α-quartz," *New Journal of physics*, vol. 16, no. 11, p. 113055, 2014.

[91] M. Farnesi Camellone, *Theoretical investigation of SiO_2 dielectric breakdown*. PhD thesis, ETH Zurich, 2007.

[92] L. Levien, C. T. Prewitt, and D. J. Weidner, "Structure and elastic properties of quartz at pressure," *American Mineralogist*, vol. 65, no. 9-10, pp. 920–930, 1980.

[93] J. Sarnthein, A. Pasquarello, and R. Car, "Structural and electronic properties of liquid and amorphous SiO_2: An ab initio molecular dynamics study," *Physical Review Letters*, vol. 74, no. 23, p. 4682, 1995.

[94] R. Smoluchowski, "Anisotropy of the electronic work function of metals," *Physical Review*, vol. 60, no. 9, p. 661, 1941.

[95] T. Kaneko, T. Yamasaki, N. Tajima, and T. Ohno, "First-principles study on reconstruction of 4H-SiC(0001) and (0001^{-})," *Surface Science*, vol. 647, pp. 45–50, 2016.

[96] S. Mehandru and A. B. Anderson, "Structures and energetics for polar and nonpolar SiC surface relaxations," *Physical Review B*, vol. 42, no. 14, p. 9040, 1990.

[97] M. C. Gibson, *Implementation and application of advanced density functionals*. PhD thesis, Durham University, 2006.

[98] T. Kimoto and J. A. Cooper, *Fundamentals of silicon carbide technology: growth, characterization, devices and applications.* John Wiley & Sons, 2014.

[99] H. Alsnani, J. P. Goss, P. Briddon, M. Rayson, and A. B. Horsfall, "First principles study of the stability and diffusion mechanism of a carbon vacancy in the vicinity of a SiO_2/4H-SiC interface," *physica status solidi (a)*, p. 1900328, 2019.

[100] D.-K. Kim, K.-S. Jeong, Y.-S. Kang, H.-K. Kang, S. W. Cho, S.-O. Kim, D. Suh, S. Kim, and M.-H. Cho, "Controlling the defects and transition layer in SiO_2 films grown on 4H-SiC via direct plasma-assisted oxidation," *Scientific Reports*, vol. 6, p. 34945, 2016.

[101] T. Zheleva, A. Lelis, G. Duscher, F. Liu, I. Levin, and M. Das, "Transition layers at the SiO_2/SiC interface," *Applied Physics Letters*, vol. 93, no. 2, p. 022108, 2008.

[102] T. Hatakeyama, H. Matsuhata, T. Suzuki, T. Shinohe, and H. Okumura, "Microscopic examination of SiO_2/4H-SiC interfaces," in *Materials Science Forum*, vol. 679, pp. 330–333, Trans Tech Publ, 2011.

[103] A. Ekoué, O. Renault, T. Billon, L. Di Cioccio, and G. Guillot, "Study of the wet re-oxidation annealing of SiO_2/4H-SiC (0001) interface properties by AR-XPS measurements," in *Materials Science Forum*, vol. 433, pp. 555–558, Trans Tech Publ, 2003.

[104] F. Devynck, "First-principles study of defects at the SiC/SiO_2 interface through hybrid functionals," tech. rep., EPFL, 2008.

[105] C. Virojanadara and L. Johansson, "Interfacial investigation of in situ oxidation of 4H-SiC," *Surface science*, vol. 472, no. 1-2, pp. L145–L149, 2001.

[106] F. Devynck, A. Alkauskas, P. Broqvist, and A. Pasquarello, "Charge transition levels of carbon-,oxygen-, and hydrogen-related defects at the SiC/SiO_2 interface through hybrid functionals," *Physical Review B*, vol. 84, no. 23, p. 235320, 2011.

[107] H. Kobayashi, T. Sakurai, M. Takahashi, and Y. Nishioka, "Interface states at SiO_2/6H-SiC (0001) interfaces observed by X-ray photoelectron spectroscopy mea-

surements under bias: Comparison between dry and wet oxidation," *Physical Review B*, vol. 67, no. 11, p. 115305, 2003.

[108] M. Bockstedte, A. Mattausch, and O. Pankratov, "Ab initio study of the annealing of vacancies and interstitials in cubic SiC: Vacancy-interstitial recombination and aggregation of carbon interstitials," *Physical Review B*, vol. 69, no. 23, p. 235202, 2004.

[109] X. Shen, M. P. Oxley, Y. Puzyrev, B. Tuttle, G. Duscher, and S. T. Pantelides, "Excess carbon in silicon carbide," *Journal of Applied Physics*, vol. 108, no. 12, p. 123705, 2010.

[110] S. Wang, S. Dhar, S.-r. Wang, A. Ahyi, A. Franceschetti, J. Williams, L. C. Feldman, and S. T. Pantelides, "Bonding at the SiC-SiO_2 interface and the effects of nitrogen and hydrogen," *Physical Review Letters*, vol. 98, no. 2, p. 026101, 2007.

[111] H. Yano, T. Hirao, T. Kimoto, H. Matsunami, K. Asano, and Y. Sugawara, "High channel mobility in inversion layers of 4H-SiC mosfets by utilizing $(11\bar{2}0)$ face," *IEEE Electron Device Letters*, vol. 20, no. 12, pp. 611–613, 1999.